

**FUNDAMENTAL BUILDING BLOCKS OF
NANOPOROUS NETWORKS FROM
ULTRA-SMALL-ANGLE X-RAY SCATTERING (USAXS)
AND SMALL-ANGLE X-RAY SCATTERING (SAXS)
EXPERIMENTS**

A Dissertation presented to
the Faculty of the Graduate School
at the University of Missouri

In Partial Fulfillment
of the Requirements for the Degree
Doctor of Philosophy

by
MICHAEL KRAUS
Dr. Peter Pfeifer, Thesis Supervisor
JULY 2010

The undersigned, appointed by the Dean of the Graduate School, have examined the dissertation entitled:

FUNDAMENTAL BUILDING BLOCKS OF NANOPOROUS NETWORKS FROM
ULTRA-SMALL-ANGLE X-RAY SCATTERING (USAXS)
AND SMALL-ANGLE X-RAY SCATTERING (SAXS) EXPERIMENTS

presented by Michael Kraus,
a candidate for the degree of Doctor of Philosophy and hereby certify that, in their
opinion, it is worthy of acceptance.

Dr. Peter Pfeifer

Dr. Carlos Wexler

Dr. Haskell Taub

Dr. Galen Suppes

Dr. Jan Ilavsky

ACKNOWLEDGMENTS

The research presented here was funded in part by the following agencies:

U.S. Department of Energy, Basic Energy Sciences, DE-FG02-07ER46411

U.S. Department of Energy, Energy Efficiency & Renewable Energy,
DE-FG36-08GO18142

Argonne National Laboratory, Advanced Photon Source, GUP 10069

I would like to thank my committee members Jan Ilavsky, Haskell Taub, Peter Pfeifer, Galen Suppes, and Carlos Wexler for their overview and support.

I would like to thank the staff of Argonne National Labs, Advanced Photon Source.

I would like to extend a sincere thanks to all of the members of the ALL-CRAFT team whose contributions cannot fit on paper, especially Elmar Dohnke and Dave Stalla for surviving multiple trips to the APS with me, and maintaining their enthusiasm. Several students in the physics department have given suggestions and support over the years, in particular Michael Gramlich, Matt Mower, Raina Olsen, Jacob Buress, Soo Yuchoong, Jeff Pobst, and John Gaddy.

I have had the opportunity to work with two remarkable young men, Jimmy Romanos and Matt Beckner. My gratitude to Matt for his help, support, and participation in this project and many others cannot be overstated.

There are four people whose involvement have resulted in this experience converging to the current state of affairs.

Dr. Wilfried Gille, your enthusiasm and willingness to freely share from your own years of experience served as an unexpected source of guidance.

Dr. Carlos Wexler who offered suggestions and, better yet, explanations for many of the results I encountered.

Dr. Jan Ilavsky, whose responses to my email questions alone fill an entire server somewhere. Thank you for teaching me and spending Easter at the beamline even though you could have been with your family. I hope you are happy with the final product.

Most of all, my thanks to Dr. Peter Pfeifer. Since writing less in these situations means more, I thank you for taking on the biggest of all challenges: teaching me about optimism and confidence, and how to use them. It may have seemed a random walk, but the net distance far exceeded the number of steps taken.

TABLE OF CONTENTS

ACKNOWLEDGMENTS	ii
LIST OF TABLES	xi
LIST OF FIGURES	xiii
LIST OF SYMBOLS	xvi
LIST OF ABBREVIATIONS	xviii
ABSTRACT	xix
CHAPTER	
1 Introduction	1
2 Porous Media	5
2.1 Introduction	5
2.2 Porous media	6
2.3 Geometric structure and characterization	6
2.3.1 Two phase porous media	7
2.3.2 Calculation of pore space characterization quantities	8
2.4 Characterization Techniques	10
2.4.1 Imbibition and drainage	10
2.4.2 Small-angle scattering	11
2.4.3 Nuclear magnetic resonance	12
2.5 Structural characterization of amorphous nanoporous media	13
2.5.1 Viable methods for nanoporous media characterization	14
2.5.2 NMR	14

2.5.3	Gas adsorption-desorption isotherms	15
2.5.4	Small-angle x-ray scattering	15
3	Analysis motivation and development	17
3.1	Introduction	17
3.2	USAXS scattering curve features	18
3.2.1	Region I	19
3.2.2	Transition Region	20
3.3	Synthetic SAXS curves	20
3.3.1	Numerical calculation	21
3.3.2	Results	21
3.4	Nanopore dimensions using form factors	24
3.4.1	Scattering from a two phase porous media	24
3.4.2	Scattering from an individual particle	25
3.4.3	Master Formula	26
3.4.4	Form factors	26
3.4.5	Motivating factor for the cylinder and rectangular box form factors	27
3.5	Correlation function method	28
3.5.1	Introduction	28
3.5.2	Cylinder correlation function	29
3.6	Data analysis: implementation	31
3.6.1	Form factors: Method I	31
3.6.2	Correlation function:Method II	33
3.7	Analysis work-flow	34
3.8	Summary and conclusion	35

4	KOH activated carbon samples	37
4.1	Introduction	39
4.2	Previous SAXS and nitrogen studies	40
4.2.1	Nitrogen studies of KOH activated carbons	40
4.2.2	Previous SAXS investigations	41
4.3	Samples 3K and 4K: cylindrical pores	42
4.3.1	Sample 3K: cylindrical pores	42
4.3.2	Method II and the cylinder core-shell model	47
4.4	Sample 4K: competing models	49
4.5	Sample AX-21/MS-30 : slit-shaped pores	52
4.5.1	Sample AX-21/MS-30: demonstration of the weak dependence of Method II on cylindrical geometry	53
4.6	Samples 5K and 6K	54
4.6.1	Violation of the primary working assumption	54
4.6.2	Transition Region power law slope: a metric of applicability	55
4.6.3	Samples with $n < 1.1$	57
4.6.4	Samples 5K, 6K: $n > 1.1$	58
4.7	Discussion of results	59
4.8	Summary and conclusion	60
5	Polymeric carbons	62
5.1	Introduction	63
5.2	Polyvinylidene chloride	63
5.2.1	Previous SAXS investigations	64
5.3	Results and discussion	64
5.3.1	A new constraint on sample characterization	69

5.3.2	The utility of Method II: a comparison of ϕ_{SAXS} and ϕ_{N_2}	70
5.4	Sample S7:surface area from SAXS	71
5.5	Summary and conclusion	73
6	Boron-doped and irradiated activated carbons	74
6.1	Introduction	74
6.1.1	SAXS for evaluating boron-doped carbons	75
6.2	Samples 3K-H6 (II,A) and 3K-H6 (II,A) Irr. 1 min.	76
6.2.1	Form factor fits	78
6.2.2	Discussion	79
6.2.3	Hydrogen results	79
6.3	Samples 3K*, 3K*-H6 (II,A), and 3K*-H7 (I,A)	80
6.3.1	Non-fractal explanation	83
6.3.2	Fractal interpretation	84
6.4	Summary and conclusion	86
7	SAXS measurements: hydrogen and methane storage performance 88	
7.1	Connection to ALL-CRAFT work	88
7.2	Trends between SAXS measurements and storage performance	89
7.2.1	Methodology	90
7.3	Results	92
7.3.1	$G_{\text{sc,CH}_4}$ and SAXS pore volume	93
7.3.2	$G_{\text{ex,CH}_4}$ and SAXS pore width	94
7.3.3	$G_{\text{ex,H}_2}$ and SAXS pore length	95
7.4	Summary and conclusion	96
8	Effect of activation temperature on pore structure	98
8.1	Introduction	99

8.2	Effect of activation temperature on pore structure	99
8.2.1	Sample 3K 700°C and AX-21/MSC-30	101
8.2.2	Samples 3K 800°C, 3K 900°C, 3K 1000°C: the contribution from mesopores	101
8.3	Model-independent SAXS analysis	103
8.3.1	Guinier approximation	103
8.3.2	Conclusion	104
8.4	Contrast matching as a method to explore pore space	105
8.4.1	Introduction	105
8.4.2	Previous SAXS contrast matching work	105
8.4.3	Contrast matching examination of the effect of activation tem- perature on Sample 3K	107
8.4.4	Explanation: percolation threshold	109
8.5	Summary and conclusion	111
9	Summary and concluding remarks	113
	APPENDIX	115
	A ALL-CRAFT	115
	B Terminology and definitions	117
B.1	Scattering refresher	117
B.2	Differential scattering cross-section	118
B.3	Absolute scattered intensity from monodisperse solid particles	118
B.4	Particle form factor	119
B.4.1	Form factor recipe	120
B.4.2	Terminology note	121
B.5	Form factors of interest	121

B.5.1	Sphere	121
B.5.2	Cylinder	122
B.5.3	Rectangular box	122
B.5.4	Cylindrical core shell model	124
B.6	Structure factor	124
B.6.1	Integral form	124
B.7	Master formula derivation	125
B.7.1	Mathematical statement of Babinet’s principle	127
B.8	Correlation Function	127
B.9	Guinier approximation	128
B.9.1	Derivation	128
C	Experimental setup	131
C.1	Transmission electron microscope	131
C.2	Hydrogen isotherms	131
C.3	Nitrogen isotherms	132
C.4	X-ray scattering	132
C.4.1	Sample outgassing	132
C.4.2	Ultra-small-angle x-ray scattering	133
C.5	Small-angle x-ray scattering	134
C.5.1	Contrast matching	135
C.6	Boron doping procedures	135
C.6.1	Method I,A	135
C.7	Method II, A	136
D	Mathematica and SAXS	137
D.1	Top panel	138

D.2 Bottom panel	139
BIBLIOGRAPHY	141
VITA	151

LIST OF TABLES

Table		Page
2.1	Classification of porous materials based on the pore size and the symmetry of its distribution within the embedding solid.	6
2.2	Demonstration of the calculation of structural quantities of a pore space	9
3.1	Data analysis flow chart.	35
4.1	SAXS porosity, and nominal dimensions of samples 3K and 4K measured from form factor fits and correlation function analysis	44
4.2	Results of power law fits for the Transition Region of carbons activated with different KOH:C ratios	58
5.1	Fabrication conditions of samples S11, S3;5Ba, S8;4Bb, and S7.	65
5.2	SAXS porosity and nominal dimensions of samples S11, S3;5B ^a , and S8;4B ^b measured from form factor fits and correlation function analysis.	68
6.1	Results of the form factor fits and correlation function analysis of Sample 3K-H6 (II,A) and Sample 3K-H6 (II,A) after being irradiated for one minute.	78
6.2	Fabrication conditions and boron wt.% for samples 3K*, 3K*-H6 (II,A), and 3K*-H7 (I,A).	81
6.3	Fractal measurements for samples 3K*, 3K*-H6 (II,A), and 3K*-H7 (I,A).	83

7.1	Hydrogen storage measurements of $G_{\text{ex,H}_2}$, and $G_{\text{sc,H}_2}$ recorded at 80 K and 50 bar, and at 303 K and 50 bar.	89
7.2	Methane storage measurements of $G_{\text{ex,CH}_4}$, $G_{\text{sc,CH}_4}$, and $V_{\text{sd,CH}_4}$ recorded at 293K and 35 bar.	90
7.3	Linear regression analysis for the two observable trends between storage measurements and SAXS parameters	92
8.1	Cumulative pore volume, change in CPV per 100°C, and percentage of pores with widths $W < 20$ Å for samples 3K 700°C, 3K 790°C, 3K 900°C, 3K 1000°C.	101
8.2	Power law slopes, prefactors, and the radius of gyration fits made to the Transition Region of the SAXS curve.	103
B.1	R_G^2 for some common shapes and the relation to their parameters. . .	129

LIST OF FIGURES

Figure		Page
2.1	Sketches of three different renditions of a two-dimensional, two-phase porous media with increasing levels of inhomogeneities.	9
3.1	Schematic illustration of the three distinguishable regions of a typical nanoporous carbon USAXS scattering curve.	19
3.2	Experimental and synthetic scattering curves of samples 3K, 4K and S11.	22
3.3	Experimental and synthetic scattering curves of Sample 3K, assuming cylindrically shaped pores.	23
3.4	A simplified schematic of a correlation function with corresponding illustration of the particle and its ghost translate.	29
3.5	Graphical method for finding the average cylinder width from the correlation function	34
4.1	USAXS curves, PSD and CPV of KOH activated carbons with different KOH:C ratios	43
4.2	Form factor fits and correlation functions analysis of Sample 3K . . .	44
4.3	Chi-square contour plots for sample 3K	45
4.4	TEM images of Sample 3K	46
4.5	Sample 3K compared with a cylindrical core-shell model.	48

4.6	Chi-square contour plots for Sample 4K	51
4.7	Form factor fits and correlation function analysis for Sample AX-21/MSC-30	52
4.8	Chi-square contour plots for Sample AX-21/MSC-30.	53
5.1	USAXS curves, PSD, and CPV of samples S11, S8;4B ^b , and S3;5B ^a . .	66
5.2	Form factor fits and correlation function analysis of Sample S11. . . .	68
5.3	Chi-square contour plots of Sample S11 demonstrating that cylindrical fits give far better agreement than box fits.	69
5.4	USAXS curve, PSD, and CPV of Sample S7. The asymptotic Porod law allows the specific surface area to be measured using SAXS. . . .	71
6.1	USAXS curves of Sample 3K-H6 (II,A) before and after one minute of irradiation.	77
6.2	Plots of the form factor fits and correlation function analysis for Sample 3K-H6 (II,A) and Sample 3K-H6 (II,A) irradiated for one minute. . .	79
6.3	USAXS curves, PSD, and CPV of samples 3K*, 3K*-H6 (II,A), and 3K*-H7 (I,A) showing the effect of boron doping using two different methods.	81
6.4	Sample 3K* fit using the rectangular box fit. Unlike samples 3K*-H6 (II,A) and 3K*-H7 (I,A), Sample 3K* clearly shows a nanoporous knee that is similar to Sample 3K.	82
6.5	Graphical illustration of the proposed boron pore clogging scenario. The USAXS curve, CPV, and PSD of the individual samples are given along with the proposed surface features that could give rise to the fractal behavior of the boron-doped samples.	86

7.1	An example of a scatter matrix plot used to find preliminary trends between SAXS measurements and hydrogen and methane storage measurements.	91
7.2	The relation between pore volumes as measured by SAXS and methane gravimetric storage capacity (g/kg) at 293 K and 35 bar.	93
7.3	Linear dependence of methane gravimetric excess adsorption (g/kg) at 293K and 50 bar on cylinder width.	95
7.4	The apparent inverse linear dependence of the hydrogen gravimetric excess adsorption at 303 K and 50 bar on cylinder length.	96
8.1	SAXS curves, CPV, and PSD for samples 3K 700°C through 3K 1000°C.	100
8.2	The contribution of mesopores to the scattered intensity as illustrated by samples 3K 700°C and AX-21/MSC-30.	102
8.3	SAXS curves of dry and dibromomethane wetted samples of 3K produced at different activation temperatures, and of Sample AX-21/MSC-30.	108
8.4	Conceptual schematic of the DBM wetting of nanopores in carbon. . .	111
B.1	Scattering geometry and wave vectors.	117
B.2	The volume of the scatterer is fixed at 565 \AA^3 for each plot. Left: Plot of the form factor of a cylinder for varying widths and lengths. Right: Rectangular box for varying side lengths A and $B = C$	123
D.1	This figure shows the top panel of the interface.	138
D.2	This figure shows the ability of the user to customize the appearance of all plots.	139
D.3	This figure shows the bottom panel of the interface. This contains the portion of the interface that allows the user to make chi-square plots and perform a correlation function analysis.	140

LIST OF SYMBOLS

Symbol	Description (Units)
V_{sample}	Total sample volume (cm^3).
V_{solid}	Solid phase volume in a two phase porous material (cm^3).
V_{pore}	Pore phase volume in a two phase porous material (cm^3).
ϕ	Volume fraction of pores ($V_{\text{pore}}/V_{\text{sample}}$).
$1 - \phi$	Volume fraction of solid material ($V_{\text{solid}}/V_{\text{sample}}$).
S	Sample interface surface area (cm^2).
S/m	Specific surface area per sample mass (cm^2/g).
S/V_{sample}	Specific surface area per sample volume (cm^{-1}).
V_{solid}/m	Specific solid volume per sample mass (cm^3/g).
V_{pore}/m	Specific pore volume per sample mass or cumulative pore (cm^3/g).
$N_{\text{solid particles}}$	Number of solid particles in a two phase porous media.
$V_{\text{single solid particle}}$	Volume of a single solid particle in a monodisperse two phase porous media consisting of a single size and shape of particle (cm^3).
$V_{\text{single pore}}$	Volume of a single pore in a monodisperse two phase porous media consisting of a single size and shape of pore (cm^3).
N_{pores}	Number of pores in a two phase porous media.
$(d\sigma/d\Omega)_e$	Differential scattering cross-section of the electron (cm^2).
ρ_e	Electron density (# electrons/ cm^3).
D_m	Mass fractal dimension.
D_p	Pore fractal dimension.
D_s	Surface fractal dimension.
D	Fractal dimension.
$N(p/p_0)$	Number of moles adsorbed at relative pressure p/p_0 .
ρ_{skeleton}	Skeletal density (cm^3/g).
$S(q)$	Particle structure factor.
$P(q)$	Single particle form factor.
$m_{\text{carbon atom}}$	Mass of a carbon atom (g).
$(d\Sigma/d\Omega)_{\text{sample}}$	Differential scattering cross-section per unit sample volume illuminated by the beam (cm^{-1}).
$(d\sigma/d\Omega)$	Differential scattering cross-section (cm^2).
$g(\vec{r})$	Correlation function.
$g_0(\vec{r})$	Correlation function of a single particle.
n	The slope of the power law- generally in the Transition Region.
L	Cylinder length measured using Method I (\AA).
W	Cylinder width measured using Method I (\AA).

A	Short length of the rectangular box measured using Method I (\AA).
B	Long length of the rectangular box measured using Method I (\AA).
W_1	The average width of a cylinder measured using Method II (\AA).
C_1	The average width of the particulate carbon phase in which a pore is embedded measured using Method II (\AA).
Σ	The specific surface area (m^2/g).
Q	The Porod invariant (cm^{-4}).
$\Delta\rho$	The difference in the mean electron density of the phases in a two phase porous media ($\# \text{ electron}/\text{cm}^3$).
$(\Delta\rho)^2$	The square of the difference in the mean electron density of the phases in a two phase porous media [$(\# \text{ of electrons})^2/\text{cm}^{-6}$].
ϕ_{SAXS}	Porosity from SAXS.
ϕ_{N_2}	Porosity from N_2 .
$G_{\text{ex,CH}_4}$	Gravimetric excess adsorption of methane (g/kg).
$V_{\text{sd,CH}_4}$	Volumetric storage density of methane (g/l).
$G_{\text{sc,CH}_4}$	Gravimetric storage capacity of methane (g/kg).
$G_{\text{ex,H}_2}$	Gravimetric excess adsorption of hydrogen (g/kg).
$G_{\text{sc,H}_2}$	Gravimetric storage capacity of hydrogen (g/kg).
μ	Mass absorption coefficient (cm^2/g).
R_G	Radius of gyration (\AA).
$I(0)$	Forward scattered intensity.
\vec{q}_{in}	The wave vector of an incident monochromatic x-ray beam.
\vec{q}_{out}	The wave vector of a scattered beam.
q	the length of the scattered wave vector (\AA^{-1}).
λ	Wavelength (\AA).
θ	The scattering angle.
$(d\sigma/d\Omega)_e (\Delta\rho)^2$	Difference in the mean scattering length density between phases in a two phase porous media (cm^{-4}).
$F(\vec{q})$	Amplitude of the single particle form factor.
$A(\vec{q})$	Amplitude of the scattered intensity.
$I(q)$	Scattered intensity (cm^{-1}).

LIST OF ABBREVIATIONS

ALL-CRAFT	Alliance for Collaborative Research in Alternative Fuel Technology.
USAXS	Ultra-small-angle x-ray scattering.
SAXS	Small-angle x-ray scattering.
SAS	Small-angle scattering.
CPV	Cumulative pore volume.
PSD	Pore size distribution.
PVDC	Polyvinylidene chloride.
DBM	Dibromomethane.
MIP	Mercury intrusion porosimetry.
NMR	Nuclear magnetic resonance.
PGAA	Prompt-gamma activation analysis spectroscopy.
FTIR	Fourier transform infrared spectroscopy.
XRD	X-ray diffraction.
WAXS	Wide-angle x-ray diffraction.
TEM	Transmission electron microscope.
CF	Correlation function.

ABSTRACT

A new method of structural analysis that measures the nominal dimensions of pores using ultra-small-angle x-ray scattering (USAXS) and small-angle x-ray scattering (SAXS) data is presented. The characterization technique developed is applied to highly porous carbons that are used for reversible methane and hydrogen storage based on physisorption.

Data is analyzed and fit under the primary working assumption that there is only one size and shape of pore and that the number of pores present in the sample is accounted for by the sample porosity, ϕ .

The procedure presented in this study is not restricted to the analysis of carbonaceous materials. It is applicable to any porous material in which the nanopore is the fundamental building block.

The advantage of our technique in comparison to methods currently used to measure the size and shape of nanopores, is that in addition to a width, at least one additional characteristic length is determined.

Chapter 1

Introduction

We propose a new method of structural analysis based on ultra-small-angle x-ray scattering (USAXS) and small-angle x-ray scattering (SAXS) data. Our method assesses the shape and nominal dimensions of the individual nanopores that constitute the fundamental building blocks of an amorphous nanoporous solid.

Our methodology uses a model-dependent particle form factor and a correlation function. These tools provide two different, independent sets of information. The particle form factor gives measurements of two characteristic lengths of an individual nanopore. The correlation function gives one characteristic length of a nanopore and one characteristic length of the carbon matrix in which it is embedded. Additionally, the correlation function provides information about sample porosity.

We will formulate and then repeatedly apply our characterization technique. Different types of nanoporous carbon samples will be used as case studies that demonstrate the consistency and quality of the results. Each case study provides information about how our technique works and more importantly, why it sometimes fails. Guidelines and “rules of thumb” for its use are developed along the way.

Some sections contain what appear to be miscellaneous topics that depart from our exposition. These sections are best thought of as case studies that illustrate the wealth

of structural information available from small-angle scattering (SAS) techniques.

The beginning of each chapter gives some preliminary information about sample composition, as well as why the sample is of interest within the broader scope of research performed by the Alliance for Collaborative Research in Alternative Fuel Technology (ALL-CRAFT), which is outlined in Appendix A. Previous studies that provide relevant results are introduced where necessary.

An outline of this study is as follows:

In chapter 2, we briefly review concepts involved in the study of porous media. The simplest possible model of a two phase porous material is introduced. Quantities commonly used to measure the structure of pore space are defined, and an explicit illustrative demonstration of their calculation is provided. Then, experimental methods used to characterize porous media are discussed. The characterization needs of ALL-CRAFT are listed and used to revisit, further down-select, and explain why SAS is our tool of choice for pore characterization. Finally, the goal of this study is plainly stated.

Chapter 3 discusses the distinguishable features of a typical nanoporous carbon USAXS scattering curve. Synthetic scattering curves are constructed using widths from nitrogen isotherm pore size distributions (PSD). The resulting curves illustrate that there is additional structural information present in the USAXS data that is absent from the nitrogen data. With this in mind, we develop our procedure for measuring the nominal dimensions of nanopores using USAXS data.

In chapter 4, our technique is applied repeatedly to nanoporous carbons activated with different ratios of KOH:C. The samples examined highlight the case of a cylindrically shaped pore, a slit-like pore, and a pore that shows competing cylindrical and slit-shaped characteristics. Samples that violate the primary working assumption formulated in Chapter 3 are used to develop an economical rule of thumb that assesses the potential for success if our technique is applied to an arbitrary nanoporous

material.

Chapter 5 examines carbons made from a polymeric precursor, polyvinylidene chloride (PVDC). These samples have very monodisperse size distributions of nanopores and, therefore, should provide a natural opportunity to benchmark our methodology. We find that PVDC samples can only be fit using cylindrical pores. Additionally, we discover that there is a minimum cumulative pore volume that is necessary for a sample to be properly characterized using the USAXS instrument. A sample demonstrating the asymptotic Porod power law is used as a case study to demonstrate how the specific surface area of a sample can be measured using USAXS.

Boron-doped activated carbons and one boron-doped irradiated activated carbon are examined in Chapter 6. Preliminary SAXS analysis and nitrogen isotherm studies suggest that the sample structure does not change upon irradiation. However, a hydrogen isotherm analysis emphasizes that this material may provide a case study in which neither SAS, nor nitrogen possess a sufficient yardstick to measure the true structure of this sample. Finally, a sample that is boron-doped using two different methods is analyzed using a very light fractal analysis that suggests pore clogging.

In Chapter 7, matrix scatter plots are used to find trends that link the pore dimensions measured in Chapter 4 to hydrogen and methane storage results. We find that the methane gravimetric storage capacity at 273 K and 35 bar depends on nanopore volume, and that methane gravimetric excess adsorption depends on pore width.

In chapter 8, nitrogen pore size distribution data is combined with pinhole SAXS data to qualitatively examine the effect of activation temperature on pore structure. Nitrogen data shows that increasing the activation temperature from 700°C to 1000°C more than doubles the cumulative pore volume. A model-independent SAXS analysis is presented that independently corroborates the finding that the pore size does, in fact, increase with activation temperature. Contrast matching studies are introduced

as a new method for probing pore space. Preliminary results from pilot studies, using dibromomethane as a contrast matching agent, help explain how the pore structure and its connectivity change with activation temperature.

Chapter 2

Porous Media

2.1 Introduction

This chapter is divided into two parts. The first part provides some necessary background information about porous media. This includes:

1. A brief description of the simplest possible model of a porous material, a sample that consists of only two phases.
2. A discussion of a two phase porous media model and the quantities commonly used to measure the structure of its pore space.
3. Discussion of the experimental methods used to characterize porous media.

The second part of this chapter discusses the specific porous media characterization needs of ALL-CRAFT, and reports the inadequacies of several of the techniques discussed in the first part of the chapter. The mission, recent accomplishments, and current goals of ALL-CRAFT are presented in Appendix A. This appendix gives the larger context and scope underlining this study. It is a reference that explains why the samples discussed in Chapters 4-8 are of interest.

2.2 Porous media

A porous material is a solid material with holes in it [1, 2]. If the size of the holes (pores) and the symmetry of their spatial distribution within the solid are known, this rough definition can be further refined along the lines of classification listed in Table 2.1. Regardless of how it is labeled or named, the defining property of any porous media is its topology. The topology describes how, and if, the pores are connected. From this, a model of the geometry of the pore space can be built.

It is the structure of the pore space that determines the vast majority of physical and chemical properties of a porous material - its diffusivity, conductivity, permeability, etc. According to Pfeifer [3], pores mediate all communication when a disordered solid interacts with its surroundings.

Table 2.1: Common classifications of porous media based on the pore size (in nanometers) and the symmetry of its distribution within the embedding solid.

Pore width (W) (nm)	Classification	Symmetry	Classification
$W < 2$ nm	Nanoporous	Translational	Locally homogeneous and isotropic
$2 \text{ nm} < W < 50$ nm	Mesoporous	Dilational	Fractal
$W > 50$ nm	Macroporous	Random	Stochastic

2.3 Geometric structure and characterization

The porosity is the most fundamental and important geometric structural measurement of a porous material. Unfortunately, porous media and pore surfaces are geometrically and chemically heterogeneous [2]. The connectivity, and breadth of the pore network is determined by how the porosity is distributed within the sample.

For large systems with large features, there are not too many measurement difficulties. However, intricate networks formed by the criss-crossing of small size scale

features of meso and nanopores can create highly tortuous features that are difficult to access experimentally in all but the simplest of materials. As a consequence, the properties measured often indirectly reflect the measurement technique.

We now present the most basic model of a porous solid in brief detail. It is used as a framework to introduce the most fundamental measurable structural parameters of pore space. Additionally, we qualitatively illustrate how difficult it can be to measure just these few parameters. This naturally leads to a dialog in which current characterization techniques are compared.

2.3.1 Two phase porous media

The simplest model of a porous solid is a material that consists exclusively of two phases, a pore phase and a solid phase. The volume of any sample can be written in terms of the contribution from the individual phases as, $V_{\text{sample}} = V_{\text{solid}} + V_{\text{pore}}$, where V_{solid} is the solid volume, V_{pore} is the pore volume, and V_{sample} is the total sample volume. By writing the sample volume in terms of its binary constituent phase volumes, we immediately find that volume fractions provide a natural language for describing the characteristic properties of our system.

There are two measurements of pore space geometry that can now be measured using our model and its assumptions. These are :

1. the sample porosity, and
2. the interfacial surface area and the specific surface area.

Porosity

The porosity, ϕ , is the most fundamental and important structural measurement of a porous material. It is defined as the fractional pore volume of the sample,

$$\phi = V_{\text{pore}}/V_{\text{sample}}.$$

By construction, as all material in the sample is either pore or solid, the sum of the volume fractions of the two phases must give unity. That is, $V_{\text{solid}}/V_{\text{sample}} + V_{\text{pore}}/V_{\text{sample}} = 1$. The fractional volume of solid in the sample, $V_{\text{solid}}/V_{\text{sample}}$, can therefore be written in terms of the porosity as $1 - \phi$.

Surface area

Dividing a porous material into two phases provides the opportunity to define a surface separating the pore phase and the solid phase. This surface has a surface area, S (cm^2). S is the total amount of interface in V_{sample} [1]. A second measurable quantity of a porous material is the specific surface area. This is the total amount of interface per unit volume or mass of material.

2.3.2 Calculation of pore space characterization quantities

Three very different sketches of two-dimensional two phase porous media are given in Figure 2.1. The sketch on the far left can be used to conceptually illustrate our procedure for characterizing pore space.¹

The white circles are considered to be pores and the black square is considered to be solid. There are nine spherical pores each with a width of 1 cm. They are embedded within a solid cube that is 5 centimeters on each side. Assuming the solid and pores have a combined mass of one hundred grams, $m=100$ g, we can give a zeroth order approximation of the pore structure using elementary geometry and the quantities just discussed. The quantities are tabulated and listed in Table 2.2 along with alternative definitions that will be used throughout this study. The numbers are not particularly realistic.

¹Please imagine it is in 3-D.

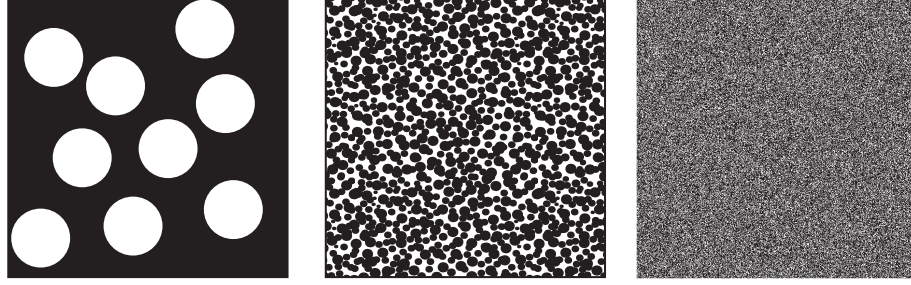


Figure 2.1: All three of these sketches qualify as two-dimensional two phase porous media. The solid phase is black and the pore phase is white. The structural measurements discussed in the text can be conceptually grasped and even explicitly measured for the simple sketch on the left. The sketch in the middle is more complex. However, the individual phases can still be distinguished by eye. The sketch on the right is far too complex to be visually processed. No details, let alone patterns, are distinguishable. This illustration is still macroscopic. The samples measured in this study are about five orders of magnitude smaller.

Table 2.2: Structural quantities of the pore space in Figure 2.1 (far left) calculated for demonstrative purposes.

Quantity	Description/name	Value
$V_{\text{sample}} \text{ (cm}^3\text{)}$	Total sample volume	125
$V_{\text{pore}} \text{ (cm}^3\text{)}$	Total pore volume	5
$V_{\text{solid}} \text{ (cm}^3\text{)}$	Total solid volume	120
$V_{\text{solid}}/m \text{ (cm}^3\text{/g)}$		1.20
$V_{\text{pore}}/m \text{ (cm}^3\text{/g)}$	Cumulative pore volume	0.04
$m/V_{\text{solid}} \text{ (g/cm}^3\text{)}$	Skeletal density (ρ_{skeleton})	0.83
ϕ	porosity	0.04
$(1 - \phi)$	Solid volume fraction	0.96
$S \text{ (cm}^2\text{)}$	Interfacial surface area	29
$S/m \text{ (cm}^2\text{/g)}$	Specific surface area (Σ)	0.29
$S/V_{\text{sample}} \text{ (cm}^{-1}\text{)}$		0.2

The only unfamiliar quantity is S/V_{sample} , which is an inverse length. Its reciprocal is sometimes considered a length that characterizes the length scale of pores [2].

It is now possible to see how further measurements characterizing the structure of pore space can be made. For example, a measurement of the distribution of pore widths within the material.² Unfortunately, the other two sketches in Figure 2.1 give a more realistic representation of the structures that one is most likely to encounter

²In our example this would yield no information since we considered only one width of pore.

in practice. Measuring the porosity, surface area, and other quantities in these cases becomes non-trivial.

2.4 Characterization Techniques

Numerous material characterization techniques have been used to investigate the geometric structure of pore space. These include stereological analysis of digital images, mono and multilayer adsorption isotherms, mercury intrusion porosimetry (MIP), dynamic light scattering, small-angle x-ray scattering (SAXS), small-angle neutron scattering (SANS), x-ray imaging, nuclear magnetic resonance (NMR) relaxation measurements, permeability and electrokinetics, and microtomography [4].

The four most commonly used techniques to determine the structure of pore space are MIP, adsorption-desorption isotherms, SAXS, and NMR [5]. Many researchers use these techniques in tandem.

Using only one characterization method is usually insufficient for a complete analysis. It is actually the cross-referencing and validation of data collected using different methods that provides the most valuable information about sample structure. That being said, not all techniques are created equal, and the information provided by one method of evaluation may give more detail than another.

2.4.1 Imbibition and drainage

MIP and adsorption-desorption isotherms consist of measuring cycles of imbibition and drainage. Imbibition is the displacement of a nonwetting phase by a wetting phase. Drainage is the displacement of a wetting phase by a nonwetting phase [2].

The technique of MIP consists of measuring injection and retraction curves of liquid mercury into and out of an initially dry porous material that has been immersed in mercury at constant temperature. The volume of mercury occupying the pore space

is plotted as a function of the applied pressure and the results presented in a capillary pressure-saturation curve [6].

Adsorption-desorption isotherms involve the same technique as MIP. A porous material is exposed to a single component gas at constant temperature and incrementally varying pressures until equilibrium is reached. The amount adsorbed per unit volume of adsorbent is measured as a function of the relative pressure $P/P_0(T)$, where $P_0(T)$ is the bulk vapor pressure.

Imbibition therefore corresponds to the adsorption branch of the isotherm and the extrusion curve of MIP. Drainage corresponds to the desorption branch of the isotherm and the intrusion curve of MIP. Both MIP curves and adsorption-desorption isotherms exhibit characteristic hysteresis loops. That is, the desorption/intrusion branch does not retrace the adsorption/extrusion branch. This is due to the fact that pore filling is independent of connectivity, geometry, and spatial correlation for imbibition. It only depends on the effective particle size. The process of drainage, on the other hand, depends on all of these variables [6].

The process of reconstructing the geometry of the pore network that gives rise to a particular set of experimental imbibition and drainage curves is very complicated. The curves are inverted and a suitable pore structure is found that produces synthetic curves consistent with the experimental data (c.f. Section 3.3.1). This is a substantially difficult problem that lacks a unique solution. The difficulty is compounded by the need to take into account the thermodynamics of film formation at the pore interface. Information about the pore shape and connectivity must be provided by the user in order to numerically find a distribution of pore widths that fit the data.

2.4.2 Small-angle scattering

All small-angle scattering (SAS) techniques (USAXS, SAXS, SANS) involve the same fundamental principle. A monochromatic plane wave is elastically scattered from a

sample through an angle θ . The intensity is measured as a function of the scattering vector that has a magnitude $|q| = 4\pi/\lambda \sin(\theta/2)$, where λ is the wavelength.

SAS can be thought of as the line shape analysis of the (000) Bragg peak. It is of greatest benefit in determining the structure of samples that have no crystalline or long range order. When dealing with disordered materials, this method replaces the traditional technique of x-ray diffraction (XRD). XRD is no longer useful, as there is no atomic length scale periodicity to be measured in amorphous materials.

Characterization of porous media using SAS experiments suffers from many of the same limitations as imbibition and drainage techniques. Primarily, that a pore shape needs to be assumed. One distinct advantage of SAS experiments is that no assumptions about pore connectivity needs to be made.

2.4.3 Nuclear magnetic resonance

NMR is one of the more subtle techniques used to probe porous media. Porous media is usually filled with fluid and then a pulse (radio frequency) is applied. Magnetization relaxation is caused by the interaction of the solid surface of pores with fluid near the surface and in the bulk [5]. Measurements of the relaxation rate in the different relaxation regimes over time provides information about the surface-to-volume ratio of the pore space.

However, the connection between the surface-volume distribution and the pore size distribution is poorly known [7]. The resolution of the experiment (i.e. the smallest detectable pore size) is determined by the instruments' minimum detection time. Having a proper signal to noise ratio is crucial for a successful NMR measurement.

Although all four techniques discussed here have a technological cost, the quality of NMR data seems to be the most directly tied to the sophistication of the measurement equipment.³ This is due, in part, to the fact that NMR offers the greatest variety of

³Obviously, we momentarily exclude SANS from the SAS technique. Large neutron sources

measurement modalities.

Now that the four main techniques used to study the structure of pore space have been discussed, we turn our attention to the particular needs of ALL-CRAFT.

2.5 Structural characterization of amorphous nanoporous media

ALL-CRAFT is dedicated to researching the use of engineered nanoporous media for alternative fuel storage, specifically, monolithic and granular nanoporous carbon.

The product of any controlled engineering process needs to be monitored in order to reproduce success and evaluate failure. Our monitoring procedure consists of meticulous sample characterization. In order to determine what makes one sample superior to another requires enumerating its characteristic properties in as much detail as possible.

In order to systematically determine the structure function relationships between different fabrication procedures and storage performance, ALL-CRAFT requires a robust pore characterization method. Mapping of the pore-space architecture gives vital feedback about the efficacy of different pore engineering mechanisms.

What makes ALL-CRAFT’s porous media characterization needs different from the needs of, say a geological or petrochemical research team, is that the most valuable and vital structural information is the information found at the smallest size scale (see Appendix A). This unique need causes the number of viable characterization methods available to shrink to only a handful of methods, for reasons that are now outlined.

cannot be purchased by individual laboratories.

2.5.1 Viable methods for nanoporous media characterization

Mercury intrusion porosimetry

This method is immediately ruled out for several reasons. The primary reason is that MIP is a technique aimed at characterizing meso and macroscopic systems. The effective size range of pores that can be measured using MIP is 3 nm to 100 μm [5]. There are other valid objections to using MIP.

The large pressures required to fill increasingly smaller pores can damage the internal structure of the material. Additionally, a certain level of mercury becomes lodged irretrievably in the material during the measurement process. Finally, pores that are close to the external surface are preferentially filled inhibiting access to the smaller pores located in the bulk of the material. As a result, these small pores may never be detected.

2.5.2 NMR

NMR is capable of measuring regions of pore space that are separated by more than one diffusion length [7]. However, pore spaces that extend beyond a few diffusion lengths are inaccessible to NMR. Therefore, exceedingly complicated and convoluted pore structures may not be measured by NMR in a sensible manner.

Additionally, conventional NMR measurements of porous media require the sample to be immersed in a fluid, typically water. The magnetization relaxation signal measured is due to the interaction of the solid surface of the pores with the fluid. Immersing activated carbon in water would simply destroy its structure, not measure it. Any soluble oxygen within the water would be immediately adsorbed.

2.5.3 Gas adsorption-desorption isotherms

Since the primary use of nanoporous carbon is as an adsorbent, characterization of these materials has focused on the use of adsorption-desorption isotherms. The adsorption-desorption isotherm provides a size distribution of pore widths. As mentioned in Section 2.4.1, in order to extract these pore widths from the data, a user is required to make assumptions about pore size and connectivity.

There are some other limitations of using adsorption-desorption isotherms for mapping out the structure of pore space. For example, in nanoporous networks the adsorption process may be very slow and present diffusion resistance for N_2 at 77 K [8]. Additionally, the choice of gas determines the range of pore sizes explored. Furthermore, closed pores are not accessible.

2.5.4 Small-angle x-ray scattering

Small-angle x-ray scattering (SAXS) does not suffer from any accessibility effects. The wavelength of the incident radiation is typically on the order of 1 Å, allowing it to probe the entire pore space.

Furthermore, although an assumption must be made about pore shape in order to interpret the data, no assumption needs to be made about pore connectivity. As stated by Pfeifer [3], this is the very property that explains how and why a porous material interacts with its surroundings. We therefore choose not to assume its properties *a priori*.

Having chosen scattering as our characterization method of choice, we are now in a position to outline the goal of this study: The goal of this study is to demonstrate that ultra-small angle x-ray scattering (USAXS) and small-angle x-ray scattering (SAXS), offer a wealth of unique information about nanopore structure. The purpose of this study is to develop a procedure that describes the nominal size and shape of individual

nanopores, the fundamental building blocks of any nanoporous material. We seek to formulate the simplest possible characterization method, the one requiring the least number of assumptions and redundancies, that still provides valuable structural information.

Chapter 3

Analysis motivation and development

3.1 Introduction

The aim of this chapter is to develop a characterization technique that provides more detailed information about nanopore structure than the set of width distributions provided by nitrogen isotherm PSDs.

First, the general features of a nanoporous carbon USAXS scattering curve are outlined and discussed. Synthetic scattering curves are then generated using nitrogen PSD data to demonstrate that there is additional structural information that can be extracted from the scattering data, but that is not present in the isotherm data. The results additionally highlight that scattering from nanoporous carbon is best modeled by correlated networks of pores and not as independent, individually scattering objects.

The rest of the chapter is devoted to developing a characterization technique for investigating nanopore morphology. The work-flow of a complete analysis cycle is presented, detailing the assumptions made in each step of the procedure, along with

the required user input and the resulting output.

3.2 USAXS scattering curve features

A representative sketch of a nanoporous carbon USAXS scattering curve is drawn in Figure 3.1. It shows two distinct regions. The first region, Region I, is the small q scattering regime. It corresponds to large length scale features of the sample. Region I contains information about the hierarchical structure of pore networks. This may also be viewed as the stacking or agglomeration of the primary scattering objects into nested structures. There is clear fractal behavior at length scales of $q \lesssim 10^{-2} \text{\AA}^{-1}$. This is discussed in Section 3.2.1.

The second region, Region II, is the large q scattering regime. It corresponds to small length scale features of the sample. The translation from reciprocal space units (\AA^{-1}) to direct space units (\AA) is given by the relation $q = 2\pi/L$, where L is the direct space length scale (\AA). Measurements made between $0.1 < q < 1 \text{\AA}^{-1}$ therefore correspond to features that range from $6 < L < 65 \text{\AA}$. It is in this region that the structural features of individual nanopores can be resolved. Region II is therefore the main focus of this study.

A third region, that is far less distinguishable than Region I or II, exists where Region I crosses over into Region II. This is the Transition Region. As the remainder of this study will be devoted to a detailed examination of Region II, Region I and the Transition Region are now discussed.

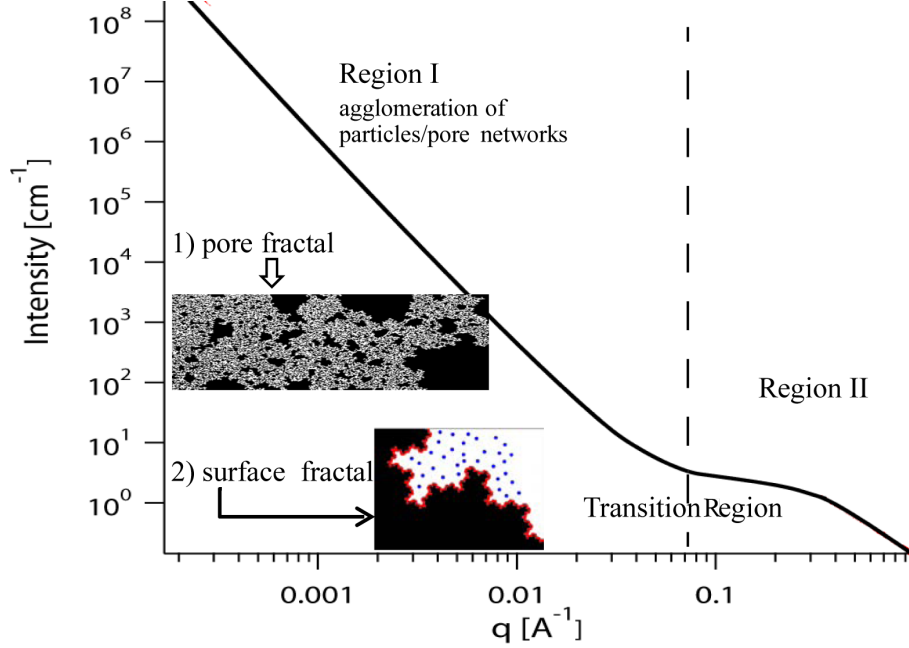


Figure 3.1: Schematic illustration of the three distinguishable regions of a typical nanoporous carbon USAXS scattering curve. Region I corresponds to the large length scale structure of the sample and demonstrates scattering proportional to a non-integer power law. Region II corresponds to the small length scale sample structure. The broad knee in the curve is due to scattering from the fundamental building block of the sample, the nanopore. The Transition Region is located between Regions I and II.

3.2.1 Region I

The scattered intensity in Region I is fractal. It can be modeled using a non-integral power law. Pfeifer [9, 10] has shown that the most general expression for the scattering from a surface/mass/pore fractal obeys the power law $I(q) \propto q^{D_s - 2D_m + D_p + 6}$, where D_s , D_m , and D_p are the fractal dimension for the surface, mass, and pore fractal respectively. The main possibility in Region I is finding a pore fractal ($I(q) \propto q^{-D_p}$, $0 < D_p \leq 3$) or surface fractal ($I(q) \propto q^{-D_s - 6}$).

The surface fractal case is the one most commonly found in activated and non-activated carbons. The surface fractal dimension D_s may loosely be interpreted as a measure of the surface sample roughness, with $D_s = 2$ representing a perfectly smooth

surface and $D_s = 3$ representing a completely space filling surface [11]. Characteristic values for the surface fractal dimension range from $D_s \approx 2.2 - 2.5$. This suggests that the global surface bounding the sample is mildly corrugated.

3.2.2 Transition Region

The cross-over region between Regions I and II is the Transition Region. It delineates where the surface fractal behavior terminates (its inner cutoff), and the knee that is characteristic of nanopore scattering begins. The Transition Region is typically observed at $q \approx 0.08-0.2 \text{ \AA}^{-1}$. Although this region is not essential in the formulation of our analysis, it is demonstrated in Section 4.6.4 that the slope of its power law provides valuable information about the relative number of mesopores in a sample.

3.3 Synthetic SAXS curves

As mentioned in Chapter 2, one of the most used tools in porous media characterization is the pore size distribution (PSD). In practice, the pore size distribution represents a simplified model of the internal structure of porous material that assumes the complex void spaces within the real solid can be modeled as an equivalent set of non-interacting, regularly shaped pore models [12]. PSD are calculated as function of width, W from the integral equation

$$N\left(\frac{p}{p_0}\right) = \int_{W_{min}}^{W_{max}} N\left(\frac{p}{p_0}, W\right) f(W) dW,$$

where $N(p/p_0)$ is the number of moles adsorbed at relative pressure p/p_0 , W_{min} and W_{max} are the effective minimum and maximum pore width of the pores present in the pore space, and $f(W)$ is the differential pore size distribution as a function of width.

3.3.1 Numerical calculation

Synthetic scattering curves are constructed under the least biased assumption that pores can be modeled as independently scattering, spherical (isotropic), particles of width W . The volume of pores with $W \in [W, W + dW] = N(W)dW \times (\pi W^3/6) = (dV/dW) dW$. The scattered intensity is therefore given by

$$I(q) = \int_0^\infty \left[\left(\frac{d\sigma}{d\Omega} \right)_e \rho_e^2 \frac{\pi W^3}{6} \frac{3(\sin qR - qR \cos qR)^2}{(qR)^3} \frac{dV}{dW} \right] dW, \quad (3.1)$$

where $(d\sigma/d\Omega)_e$ is the differential scattering cross-section of the electron (cm^2), ρ_e is the electron density of amorphous carbon ($\rho_e = 6 \times \rho_{\text{skeleton}}/m_{\text{carbon atom}}$), ρ_{skeleton} is the skeletal density of amorphous carbon (cm^3/g), and $m_{\text{carbon atom}}$ is the mass of a carbon atom (g). For numerical calculations $(d\sigma/d\Omega)_e = 7.9 \times 10^{-26} \text{ cm}^2$, $\rho_{\text{skeleton}} = 2.0 \text{ g/cm}^3$, $\rho_e = 6.0 \times 10^{23} \text{ electrons/cm}^3$. All widths used in Equation (3.1) are taken from the PSD of the corresponding experimental nitrogen isotherms.

3.3.2 Results

The experimental USAXS curves of samples 3K (red), 4K (blue), and S11 (green) are plotted as open circles, while the synthetic scattering curves (constructed from nitrogen PSD data using Equation (3.1)) are plotted as closed triangles in Figure 3.2. The PSD of each sample is plotted in the inset found in the top right corner of the graph. Samples 3K, 4K, and S11 all have a distinct nanopore knee at large q values.

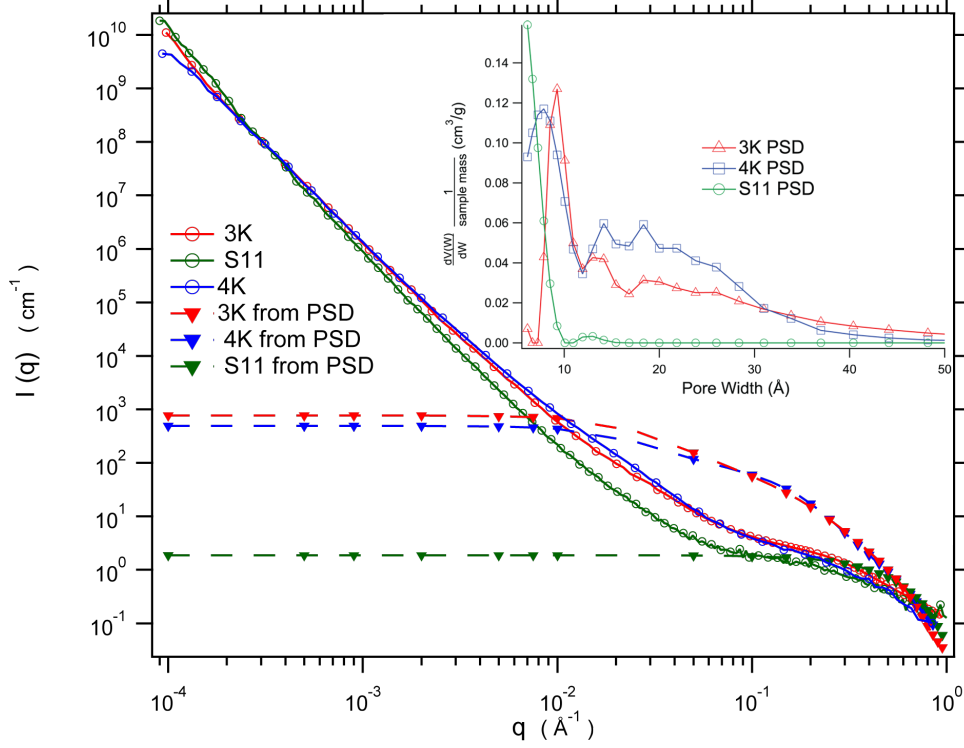


Figure 3.2: Experimental USAXS curves (open circles) and synthetic scattering curves constructed from nitrogen PSD data (closed triangles) for samples 3K (red), 4K (blue), and S11 (green). The synthetic curves have greater intensities than the experimental curves. This suggests inter-particle interference in the experimentally measured samples. Top right: PSD of samples 3K, 4K, and S11 from N_2 isotherms.

The most noteworthy result of this exercise is the observation that all synthetic scattering curves have intensities that are greater than the corresponding experimental intensities. The only physical explanation for the diminished intensities observed in the experimental data is some form of destructive interference. The most likely mechanism for this is inter-particle interference. This suggests that pores do not scatter as N independently scattering particles, but as correlated networks.

An immediate objection to this hypothesis is that the wrong shape has been used to model the pores. That is, a more appropriate choice of particle shape will result in an acceptable duplication of the experimental USAXS curve, while staying within an independently scattering particle framework. We qualitatively demonstrate that this is not the case by replacing spheres with cylinders and proceeding as follows.

Sample 3K has peaks in its PSD corresponding roughly to the following distribution of widths: $W=9\text{ \AA}$:71%, $W=18\text{ \AA}$:14%, and $W=24\text{ \AA}$:15%. We assume a cylinder of fixed length $L=18\text{ \AA}$,¹ and generate a synthetic scattering curve following the same procedure used in Section 3.3.1. As shown in Figure 3.3, the resulting synthetic curve does not give any better agreement with the experimental data.

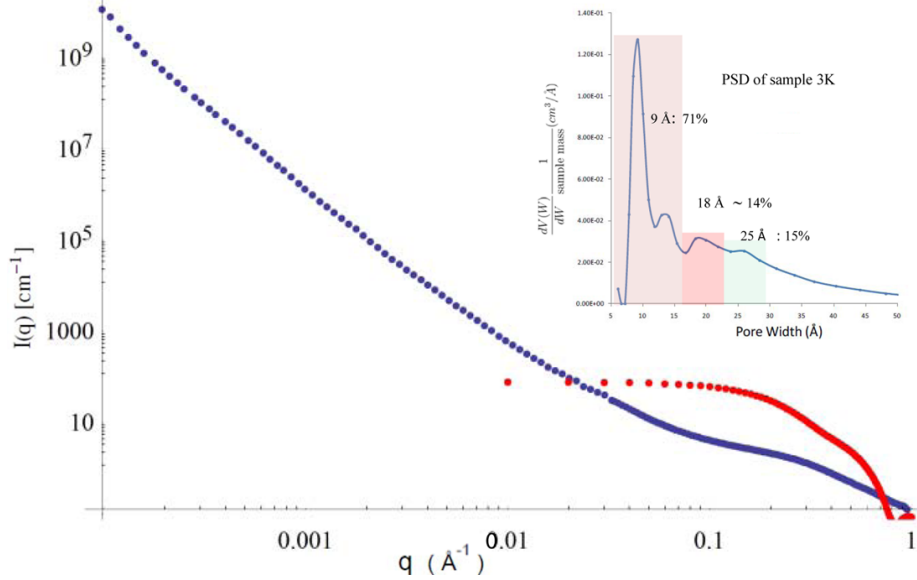


Figure 3.3: Experimental (blue) and synthetic (red) scattering curves of Sample 3K. The synthetic scattering curve is generated using the three highlighted regions of the PSD plotted in the top-right corner of the graph, and assuming a cylindrically shaped pore with fixed length, $L=18\text{ \AA}$.

In summary, none of the high surface area nanoporous carbons discussed here can be adequately modeled using an independent single scatterer approximation that is consistent with the N_2 pore size distribution data. In other words, the experimental absolute scattered intensity of the USAXS curves cannot be replicated using N_2 PSD data alone. The immediate conclusion is that USAXS data gives additional information about the sample structure that is missing from the nitrogen data.

¹This choice of length is not arbitrary and will coincide with results presented in Chapter 4.

3.4 Nanopore dimensions using form factors

The simplest way to get information beyond the PSD, is to find a pore length in addition to finding a pore width.² In order to incorporate explicit geometric structural parameters into an expression for the scattered intensity the use of a particle form factor is required. Particle form factors describe the influence of a particles' shape on the scattered intensity (Section 3.4.4).

Primary working assumption

We are interested in modeling pores using simple shapes. We adopt the viewpoint that the solid (granular activated carbon) consists of one size and shape only, the sample is monodisperse. Explicitly, no distribution of sizes is considered. We assume that the number of pores present in the solid is accounted for by the sample porosity ϕ , which is the volume fraction occupied by pores. Furthermore, the shapes considered are simple geometric forms (e.g. a cylinder or rectangular box).

3.4.1 Scattering from a two phase porous media

We continue with the model of the two phase porous media introduced in Chapter 2, and use it to write an expression for the intensity elastically scattered from a monochromatic x-ray beam (Appendix B.1). First, we generalize our definition of volume fractions so that we can find the scattered intensity corresponding to a single pore.

²The explicit definitions of all terminology and formulas used in this section are given in Appendix B and are indexed here for brevity.

Volume fractions

A sample consisting of only a single pore size and a single solid particle size has a sample volume

$$V_{\text{sample}} = N_{\text{solid particles}} V_{\text{single solid particle}} + N_{\text{pores}} V_{\text{single pore}} \quad (3.1.a),$$

where $N_{\text{solid particles}}$ is the number of solid particles (all of which have a corresponding volume $V_{\text{single solid particle}}$), and N_{pore} is the number of pores (all of which have a corresponding volume $V_{\text{single pore}}$).

Using the nomenclature of Section 2.3.1, the volume fraction of each phase can be expressed in terms of the number densities of pore and solid. For the case of a single particle size, the volume fraction of pores (the porosity) is

$$\phi = \frac{N_{\text{pores}} V_{\text{single pore}}}{V_{\text{sample}}} \quad (3.1.b).$$

The solid volume fraction can be written in terms of the porosity as

$$\frac{N_{\text{solid particles}} V_{\text{single solid particle}}}{V_{\text{sample}}} = 1 - \frac{N_{\text{pores}} V_{\text{single pore}}}{V_{\text{sample}}}.$$

3.4.2 Scattering from an individual particle

The expression for the absolute scattered intensity due to N single, monodisperse, isotropic, independently scattering solid particles within a sample volume, V_{sample} , is given by the differential cross-section per unit sample volume ($(d\Sigma/d\Omega)_{\text{sample}}$ ³)

$$\left(\frac{d\Sigma}{d\Omega} \right)_{\text{sample}} = \left(\frac{d\sigma}{d\Omega} \right)_e \rho_e^2 \frac{N_{\text{solid particles}}}{V_{\text{sample}}} (V_{\text{single solid particle}})^2 P(q) S(q). \quad (3.2)$$

³see Equation (B.2) in Appendix B.6.1 for the derivation.

For a single particle, $N_{\text{solid particles}} = 1$ and Equation(3.2) becomes

$$\left(\frac{d\Sigma}{d\Omega}\right)_{\text{sample}} = \left(\frac{d\sigma}{d\Omega}\right)_e \rho_e^2 (1 - \phi) V_{\text{single solid particle}} P(q) S(q) \quad (3.3)$$

3.4.3 Master Formula

The quantity $(N_{\text{pores}} V_{\text{single pore}} / V_{\text{sample}})$ is the volume fraction of pores, ϕ . The quantity $(N_{\text{solid particles}} V_{\text{single solid particle}} / V_{\text{sample}})$ is the volume fraction of carbon, $1 - \phi$. Using the result derived in Appendix (B.6.1) leads to our master formula

$$\left(\frac{d\Sigma}{d\Omega}\right)_{\text{sample}} = \left(\frac{d\sigma}{d\Omega}\right)_e \left(\frac{\text{no. of electrons} \times \rho_{\text{skeleton}}}{m_{\text{carbon atom}}}\right)^2 \phi (1 - \phi) V_{\text{single pore}} P(q). \quad (3.4)$$

Intuition suggests that we call the carbon grains the solid phase, and call the pores the pore phase. The idea of effectively assigning an electron density ρ_e to a pore consisting of vacuum is subtle. However, the Babinet principle of complementarity (a consequence of Fourier inversion) allows the role of pore and matter to be interchanged without any loss of generality.

3.4.4 Form factors

The term $P(q)$ in Equation (3.4) is the particle form factor. Detailed expressions for the form factors of interest, as well as an outline of how to derive form factors for particles of any arbitrary shape, are given in Appendices B.5 and B.4 respectively. The form factors that will be used consistently throughout this study are the cylinder:

$$P(q)_{\text{cylinder}} = \int_0^{\frac{\pi}{2}} \left[\frac{2J_1(q \frac{W}{2} \sin \theta) \sin(q \frac{L}{2} \cos \theta)}{q \frac{L}{2} \cos \theta q \frac{W}{2} \sin \theta} \right]^2 \sin \theta d\theta, \quad (3.5)$$

where L is the pore length and W the pore width; and the rectangular box:

$$P(q) = \frac{2}{\pi} \int_0^{\frac{\pi}{2}} \int_0^{\frac{\pi}{2}} \left[\frac{\sin(q\frac{A}{2} \sin \phi) \sin(q\frac{B}{2} \cos \phi)}{q\frac{A}{2} \sin \phi q\frac{B}{2} \cos \phi} \right]^2 \cdot \left[\frac{\sin(q\frac{C}{2} \cos \theta)}{q\frac{C}{2}} \right]^2 \sin \theta d\theta d\phi, \quad (3.6)$$

where A , B , and C are the side lengths of the box [13]. Side length A (subsequently abbreviated as A) corresponds to the short dimension of the box, while side length B (subsequently denoted B) corresponds to the the long dimension of the box. Side length C is set equal to B in order to approximate the geometry of a pair of slits.

We note that the pore volume V_{pore} in the master formula depends on the choice of form factor. If the cylinder form factor is used, pores will have a volume $V_{\text{pore}} = \pi L(W/2)^2$. If the rectangular box is used, pores will have a volume $V_{\text{pore}} = AB^2$. This dependence needs to be kept in mind when calculating the values of the scattered intensity in Equation (3.4).

3.4.5 Motivating factor for the cylinder and rectangular box form factors

Section 3.4 stated that the main goal of this study is the development of a procedure that will give structural information about nanopores that extends beyond a pore size distribution.

The choice of the cylinder and rectangular box shapes are motivated by currently debated models of activated carbons. Activated carbons are often approximated as having slit-shaped pores or a structure resembling ex-foliated graphite [14] [15]. The slit-shaped pore is a common model chosen for the kernel in density functional theory calculations used to construct pore size distributions from experimental isotherms [16, 17]. Many computational simulations of adsorption on activated carbons use a slit-shaped pore model as well [18–21].

A less widely held view is that activated and glassy carbons have elliptically

or cylindrically shaped pores [22–24]. In addition to developing a methodology to characterize pore morphology in this study, we therefore also seek information that might provide evidence for the existence of one or both of these shapes.

3.5 Correlation function method

3.5.1 Introduction

The small-angle scattering (SAS) correlation function (CF), $g(\vec{r})$, is a monotonically decreasing function that measures the common, or overlapping, volume of a particle and its ghost⁴ averaged over all orientations. The initial slope of the CF is a function of the external surface of the particle [25]. At small values of r , the derivative of the correlation function can be used to find the specific surface area of a well defined system.

The SAS CF is an extremely complicated function and only the simplest shapes (e.g. a sphere) have correlation functions that can be evaluated analytically.⁵ This is due to the fact that increasingly complicated shapes will have integration limits that depend explicitly on the parameter r .

The SAS CF must satisfy certain boundary conditions:

1. $g(0) = 1$, and
2. $g(L_{\max}) = 0$

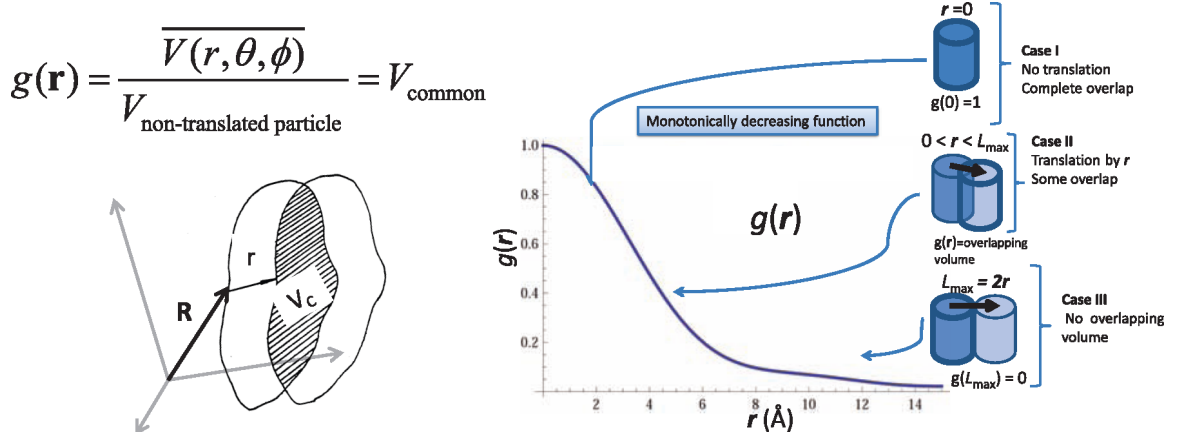
L_{\max} is a characteristic length scale that specifies the maximum distance a particle can be translated before condition 2 is met.

These boundary conditions communicate a lot of conceptual information about how the CF works. Condition 1 corresponds to the case in which the translation vector is equal to zero, $r = 0$. For this particular configuration, the particle and its

⁴Defined as the image of the particle at the origin translated by a vector, \vec{r} .

⁵For the case of the cuboid see [26]. For a complete treatise see [27].

ghost occupy the same position in space. As a consequence, their respective volumes completely overlap, as illustrated in the top-right corner of Figure 3.4. Condition 2 corresponds to the case where the ghost has been translated a sufficient distance such that no common volume is shared between the two, as illustrated in the bottom-right corner of Figure 3.4.



3.5.2 Cylinder correlation function

The correlation function for a single long cylinder or an elongated rod is given by the expression

$$g_0(r, W_1) = 1 - {}_2F_1\left(-\frac{1}{2}, \frac{1}{2}; 2; \frac{r^2}{W_1^2}\right) \simeq 1 - \frac{r}{W_1} + \frac{r^3}{W_1^3} + O[r]^5, \quad 0 \leq r < W_1^6 \quad (3.7)$$

and

$$g_0(r, W_1) = 1 - {}_2F_1\left(-\frac{1}{2}, \frac{1}{2}; 2; \frac{W_1^2}{r^2}\right), \quad r > W_1, \quad (3.8)$$

⁶The subscript 0 attached to the symbol g indicates that this is the correlation function of a single particle. For the isotropic case $|\vec{r}| = r$.

where W_1 is the average width of the rod, r is a parameterized length scale (measured in Å in this case), and ${}_2F_1$ is the Gauss hypergeometric function. All of the even coefficients of Equation (3.7) are zero. Since we are interested in pores of finite size, $r < W_1$, Equation (3.7) is the expression we use.

Evaluating the Gauss hypergeometric function at $r = W_1$ gives

$${}_2F_1\left(-\frac{1}{2}, \frac{1}{2}; 2; \frac{w^2}{r^2}\right)\Big|_{r=W_1} = 8/3\pi.^7$$

Substituting this result into Equation (3.7) we find that the average cylinder width W_1 is given by $g_0(W_1, W_1) = 1 - 8/3\pi$. Assuming the pore is cylindrically shaped, Gille [29] found that W_1 can be found graphically by locating the intersection of $g_0(r)$ and $r \cdot g_0(r)$ with the lines $(1 - 8/3\pi)$ and $r \cdot (1 - 8/3\pi)$ respectively. The only data needed for the construction of this plot is the normalized Fourier sine transform of the experimental scattered intensity, Equation (B.15).

More information about the sample structure can be gained by examining the position of the inflection points in the plot of $r \cdot g_0(r)$. The first point beyond the intercept of $(1 - 8/3\pi)$ and $r \cdot g_0(r)$ indicates a change in length scale [31, 32] that corresponds to a spatial sequence of pore plus carbon matrix, $W_1 + C_1$. Finding W_1 and $W_1 + C_1$ automatically yields C_1 . Assuming that W_1 and C_1 are fundamental lateral length scales of our nanoporous material, the porosity can be calculated from SAXS using the relations

$$\frac{V_{\text{pore}}}{V_{\text{sample}}} = \phi_{\text{SAXS}} = \frac{W_1}{W_1 + C_1}, \quad (3.9)$$

and

$$\frac{V_{\text{solid}}}{V_{\text{sample}}} = 1 - \phi_{\text{SAXS}} = \frac{C_1}{W_1 + C_1}. \quad (3.10)$$

⁷The rigorous parameterization and relations connecting the correlation function of an oval domain to a three dimensional infinitely long cylinder is given in [28]. Further justification and application of these results to elongated cylinders of finite length, as well as the result of easing the condition of constant oval cross-section are discussed in [29, 30].

The procedure for implementing the form factor and correlation function analysis is now outlined.

3.6 Data analysis: implementation

In this section the assumptions and required input needed to characterize nanopores using Methods I and II are discussed. Each method is presented independently, followed by a table that outlines the work-flow of a complete analysis cycle.

The use of a particle form factor in Method I requires the *a priori* assumption of a nanopore shape. That is, it requires the user to choose a model dependent form factor representing the pores' shape.

Method II is based on the assumption that pores can be modeled as elongated rods with an oval cross-section. This is a far more general assumption, and is therefore less restrictive than that of Method I.

Both methods independently give a sample width and length as desired (c.f. Section 3.4). We expect the results of the two techniques to give the highest level of agreement for the case of cylindrically shaped pores. This is due to the fact that Method II assumes that a pore can be modeled as an elongated rod with an oval cross-section. This is confirmed in Sections 4.3.1 and 4.4.

3.6.1 Form factors: Method I

Method I requires porosity measurements from nitrogen isotherm experiments as user input. Form factor fits involve finding the structural parameters in Equations (3.5) and (3.6) that provide the best overall fit to the experimental data. These parameters are W and L if the cylinder form factor is used, and side lengths A and B if the rectangular box form factor is used.

Best fit criteria

The phrase “best overall fit” is not limited to the strict statistical sense of minimizing the chi-square error. The form factors are highly oscillatory functions expressed on a log log scale. The chi-square statistic alone cannot be the only measure of the goodness of fit. A typical USAXS curve spans nine decades in intensity and five decades in reciprocal space. As a result, small errors between the observed and expected intensity values at small q give much larger contributions to the error than large errors at large q .

Our expanded working definition of a good fit consists of three criteria. It must

1. have a reasonable chi-square value,
2. have line plots that pass a visual inspection, and
3. give values suggestive of physically reasonable pore dimensions.

Form factors are fit by combining two plotting methods: a line plot and a chi-square contour plot. When performing an analysis, the chi-square contour plot is examined first and the results are then checked for consistency using the line plots.

Chi-square contour plots

Two dimensional contour plots of the chi-square statistic are constructed. The difference between the experimentally measured intensity and the intensity calculated using the master formula are tabulated over a large parameter space. The value of $P(q)$ in Equation (3.4) is calculated using Equation (3.5) for the case of the cylinder and Equation (3.6) for the case of the rectangular box.

The values of the form factor parameters that correspond to the minimum chi-square value are determined by simply reading the x and y axes of the plot. If the cylinder form factor is used the contour plot axes are W and L . If the rectangular box form factor is used, the contour plot axes are A and B . For cylinders, the chi-square value is tabulated for all combinations of widths between W :3-10 Å and lengths

between $L:6-35 \text{ \AA}$. For the rectangular box all combinations of lengths between $A:2-8 \text{ \AA}$ and $B:4-20 \text{ \AA}$ are calculated. The plots may be truncated if the data of interest is confined to a small region.

The reason such a large parameter space is considered is so multiple aspect ratios can be evaluated within a single plot. Different aspect ratios correspond to different shapes. For example, if the cylinder chi-square plot has a minimum in which $L \ll W$, then the cylinder can rightfully be considered a flat disk. Similarly, if the rectangular box chi-square plot has a minimum in which $A \ll B$, it can be considered to be a narrow pair of slits rather than a cubic box. In sum, the achievement of sampling such a large parameter space is that many different shapes and sizes of pore can be evaluated and presented simultaneously.

It is not uncommon to have several minima in a contour plot due to the large parameter space considered. This mandates the use of line plots to check the validity of the chi-square results.

Line plots

Line plots of the experimental data and the master formula are made using the pore dimensions obtained from the chi-square plots. If the width and lengths from the chi-square plots give line plots that disagree, they are incrementally adjusted until the best visual fit to the experimental data is achieved (see Appendix D).

3.6.2 Correlation function:Method II

The only input needed for the construction of this plot is the normalized Fourier sine transform of the experimental data (Equation (B.15)).⁸ This gives $g_0(\vec{r})$. Plots of

⁸The significance of the term $r \cdot g_0(r)$ in relation to the distance distribution is found on p. 155 of [33].

the lines $(1 - 8/3\pi)$, $r \cdot (1 - 8/3\pi)$, and $r \cdot g_0(r)$ follow in a self-evident fashion. The graphical construction used to find W_1 and C_1 is given in Figure 3.5.

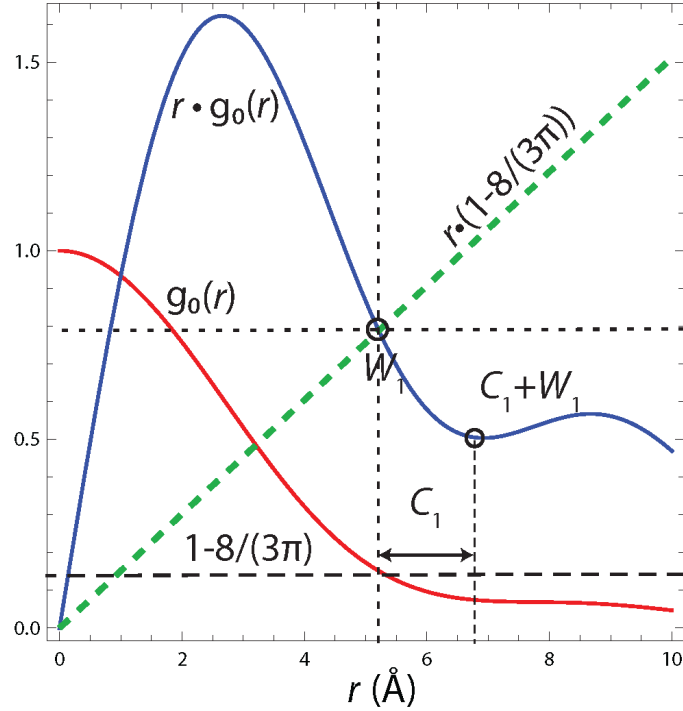


Figure 3.5: Graphical construction used to find the average pore width W_1 of a cylinder and the average width of the carbon matrix C_1 surrounding the pore. The correlation function $g_0(r)$ (solid red line), $r \cdot g_0(r)$ (solid blue line), and the dashed lines $r \cdot (1 - 8/3\pi)$ and $(1 - 8/3\pi)$ are plotted. The average pore width is found graphically by locating the intersection of $g_0(r)$ with the line $(1 - 8/3\pi)$ and $r \cdot g_0(r)$ with the line $r \cdot (1 - 8/3\pi)$.

3.7 Analysis work-flow

A table outlining the assumptions, required input, and expected output using the form factor analysis outlined in Section 3.4.4 (Method I) and the correlation function analysis outlined in Section 3.5 (Method II) is presented in Table 3.1. Method I is clearly a model-dependent technique, whereas Method II is a weakly model-dependent technique.⁹ The fundamental assumption that is common to both techniques is that

⁹The only requirement is that the scatterer has a constant oval right-section [29].

a carbon grain consists of only one size and shape of pore, and that the number of pores present in the solid is accounted for by the sample porosity.

Table 3.1: Flow chart of the required assumptions, input, and output from the two methods of data analysis introduced in Sections 3.4.4 and 3.5.

	Method I	Method II
Input	Porosity measurements from N ₂ data Experimental Data	Experimental Data
Assumption	Shape of pore - based on choice of form factor	Porosity ϕ is unknown Pore can be approximated as a long cylindrical rod or form with similar geometrical cross-section
Output	Average nominal width W and length L using the cylinder form factor Average nominal side lengths A, B if the rectangular box form factor is chosen	Average nanopore width W_1 Average length of carbon matrix between pores C_1 Sample porosity ϕ_{SAXS}

3.8 Summary and conclusion

A method for quantitatively characterizing the nominal dimensions of nanopores in amorphous porous materials has been developed. The primary working assumption is that the solid (granular activated carbon) consists of one size and shape only, the sample is monodisperse, and that the number of pores present in the solid is accounted for by the sample porosity.

Method I uses a particle form factor to estimate the contribution that a nanopore's size and shape makes to the scattered intensity at large q values. Pores are modeled using the simple shapes of the cylinder and rectangular box. Method I is model-

dependent.

Method II uses the correlation function of an elongated cylinder to calculate the average pore width W_1 and the average width of the carbon matrix surrounding the pore, C_1 . Method II also gives a measurement of sample porosity from SAXS, ϕ_{SAXS} . Unlike Method I, Method II is weakly model-dependent.

A flow chart outlining the assumptions, the required user input, and the resulting output for Methods I and II is presented. This chart details the ingredients necessary for pore characterization. Together, the two methods provide a stand-alone analysis that yields at least two length scales of the fundamental building block of a nanoporous solid.

Chapter 4

KOH activated carbon samples

The carbon samples examined in this chapter are fabricated by controlled pyrolysis of ground corncob and then activated with potassium hydroxide, KOH [34]. Samples with four different ratios of KOH to carbon are considered, with the ratios ranging from 3 to 6 KOH:C. The sample name indicates how it was prepared.¹

The characterization method developed in Chapter 3 is applied repeatedly in this chapter to learn about both the sample structure and the merit of our characterization technique. The analysis of each sample is presented in conjunction with what it reveals about the advantages and disadvantages of our approach.

First, samples that can be successfully fit are discussed. Samples 3K, 4K, and AX-21/MS-30 give examples of the successful implementation of our characterization method. They are developed as individual case studies that highlight the different possible outcomes of using Methods I and II. Samples 3K and AX-21/MS-30 provide additional information about the behavior our methodology itself. A brief synopsis follows:

- Sample 3K provides a case study of a cylindrically shaped pore (Section 4.3.1).

¹For example Sample 4K was prepared with a ratio of 4 KOH:C.

The fit results are used to validate a key assumption of Method II, that the sample porosity can be estimated using only the lateral nanopore widths W_1 and C_1 (Section 4.3.2).

- Sample 4K illustrates a case in which the box and cylindrical form factors simultaneously compete for the best fit (Section 4.4).
- Sample AX-21/MS-30 (Section 4.5) provides a case study of a slit-shaped pore. In comparison to samples 3K and 4K, Sample AX-21/MS-30 shows the largest percentage error between ϕ_{SAXS} and ϕ_{N_2} . This discrepancy is used to demonstrate the weak dependence of Method II on cylindrical geometry (Section 4.5.1).

We note that as the chapter progresses, not every line plot, or chi-square contour plot will be given unless it is specifically referenced. One full illustration of their use is sufficient.

It is not possible to fit samples 5K and 6K within the framework of our analysis. This is not a surprise considering that these samples have significant volume fractions of mesopores. Our primary working assumption is that pores consist of one size and shape only. The existence of mesopores, therefore, conflicts with the foundation of our assumption.

We elect to use samples 5K and 6K to establish a working rule of thumb that assesses the potential for a successful outcome if our technique is applied to an arbitrary nanoporous sample. We develop a cost-effective metric, that qualitatively evaluates the degree of pathology introduced as different sizes and shapes of pore begin to enter into our material. The slope of the power law in the Transition Region provides sufficient information to gauge the relative degree of nanopore homogeneity within a sample.

We pause to note that samples 3K and 4K are the best overall performers in terms of hydrogen gravimetric storage capacity at 303 K and 80 K respectively. The fact that these two samples can be well-characterized with our technique highlights its relevance in determining the structure of high performing samples. In sum, it provides valuable information about nanoporous carbons that are ALL-CRAFT benchmarks for storage performance.

4.1 Introduction

ALL-CRAFT is interested in KOH activated carbons because they provide a way to increase the sample surface area through a chemical activation process. Fourier transform infrared spectroscopy (FTIR) studies of the products that result from the interaction of KOH and carbon, upon heating, have been used to propose two possible reactions that occur during the activation process [35]:

1. $4\text{KOH} + \text{C} \leftrightarrow 4\text{K} + \text{CO}_2 + 2\text{H}_2\text{O}$
2. $6\text{KOH} + \text{C} \leftrightarrow 2\text{K} + 3\text{H}_2 + 2\text{K}_2\text{CO}_3$

This means that the activation process consists of an initial redox reaction where carbon oxidizes to CO or CO₂, producing porosity and a potassium byproduct. Metallic potassium from the reduction of KOH forms intercalating compounds that increase the distance between graphene layers, allowing the activating agent better accessibility [14]. It is therefore believed, that alkaline hydroxides penetrate deeper into carbon than CO₂, steam, or physical activation methods [36].

4.2 Previous SAXS and nitrogen studies

Quantitative SAXS investigations of KOH activated carbons are rare. There are, however, a variety of N₂ adsorption studies available. The results of a few nitrogen experiments that supplement our SAXS analysis are presented in this section.

Results from two SAXS studies that provide at least one measurement of the pore size² of an activated carbon are listed. One study provides a measurement of the radius of gyration (see Section 8.3.1 and Appendix B.9). The other, is the only known SAXS study of activated carbon³ that provides measurements of two pore length scales.

4.2.1 Nitrogen studies of KOH activated carbons

The results of a few KOH activated carbon adsorption studies that give average nanopore widths are briefly discussed. These studies are of interest because the ratios of KOH:C used during sample fabrication are the same as those explored in this chapter. The main difference between samples is the choice of the precursor material. The pore widths measured by these researchers are used for comparative purposes in Section 4.7.

In 2006, a group from Mexico activated evergreen oak, using a ratio of 4 KOH:oak at a temperature of 760°C [37]. Using the Horvath-Kawazoe equation, they determined the average micropore width to be 5.5 Å.

That same year, Ubago-Perez *et. al* fabricated monolithic and granular KOH activated carbons using olive stones [38]. They produced materials with KOH:olive stone ratios of 2:1, 4:1, and 5:1 activated at 840°C. The average nanopore width⁴, measured using 3 different adsorbates, was 6Å for all KOH concentrations. The

²Excluding measurements from correlation functions.

³To the author's knowledge.

⁴Note: this is the average nanopore width, which is different from the average pore width.

authors claim that the nanopore size distribution is homogeneous.

Finally, in 2009, a systematic study of coffee beans activated with ratios of 1:1 through 5:1 KOH:coffee bean and activated at 850°C was performed by Takahata *et.al.* [39]. They found that the peak of the primary nanopore width ranged from 6-11 Å for all samples.

4.2.2 Previous SAXS investigations

There is one SAXS investigation of a KOH activated carbon that provides a measurement of the pore width. Carbide derived carbons (CDC) activated with a ratio of 3KOH:CDC at 800°C were fit using a modified version of the procedure used by Kalliat *et. al.* [40](see Section 4.6.1), in which the number of unknowns were reduced from 8 to 3 [41]. The samples produced had radius of gyration measurements of 5.5 Å and 6.1 Å. Assuming a spherical model, these values correspond to spherical pores with widths of 13.0 Å and 16.0 Å respectively.

The only SAXS study to offer two characteristic length scales of a single sample was done by Laszlo *et. al.* [42], who studied steam activated granular carbon made from poly(ethylene terephthalate) (PET) that was functionalized using NaOH. This study is unique because it gives both a sample width and length, however, the length measured is fundamentally different from the length that we measure (this is discussed in Section 4.7).

The authors included both a particle form factor and structure factor in the expression for the scattered intensity, $I(q) \propto P(q)S(q)$. The particle's radius of gyration (R_G) was found using the Debye-Bueche approximation for the particle form factor, $P(q) \sim (1 + a^2 q^2)$. The structure factor used was the Fournet approximation,

$$S(q) = \left[1 + \frac{24\phi(\sin(qL) - qL \cos(qL))}{(qL)^3} \right]^{-1}.$$

The length L measured in this study is described as an “effective filling factor,” or distance of closest approach. Three different samples measured in air had R_G values of $R_G = 6.1 \text{ \AA}$, 5.8 \AA , and 5.7 \AA and lengths of $L = 20 \text{ \AA}$, 19 \AA , and 19 \AA respectively.

4.3 Samples 3K and 4K: cylindrical pores

4.3.1 Sample 3K: cylindrical pores

The USAXS curve of Sample 3K clearly illustrates the knee considered to be the hallmark of nanopore scattering (Figure 4.1), suggesting that it is a prime candidate for our analysis.

Method I and II results

The porosity measured from N_2 is $\phi_{N_2} = 0.78$. Using this value as the input for Method I, while taking into consideration the fit criteria outlined in Section 3.6.1, the best fits are $W = 6 \text{ \AA}$ and $L = 19 \text{ \AA}$ using the cylinder form factor, and $A = 3.5 \text{ \AA}$, $B = 13 \text{ \AA}$ using the box form factor (Table 4.1 and Figure 4.2). Method II gives an average cylinder width $W_1 = 6 \text{ \AA}$ and an average carbon matrix width $C_1 \approx 2 \text{ \AA}$. The SAXS porosity is $\phi_{SAXS} = 0.77$.

Using the results of the form factor fits, we are able to calculate the corresponding pore volumes using $V_{\text{cylinder}} = \pi(W/2)^2 L$ for cylinders, and $V_{\text{box}} = AB^2$ for boxes. The cylindrical pore has a volume of 540 \AA^3 , whereas the box pore has a volume of 590 \AA^3 . In sum, there is roughly a ten percent difference between the two volumes. This suggests that these are not competing models.

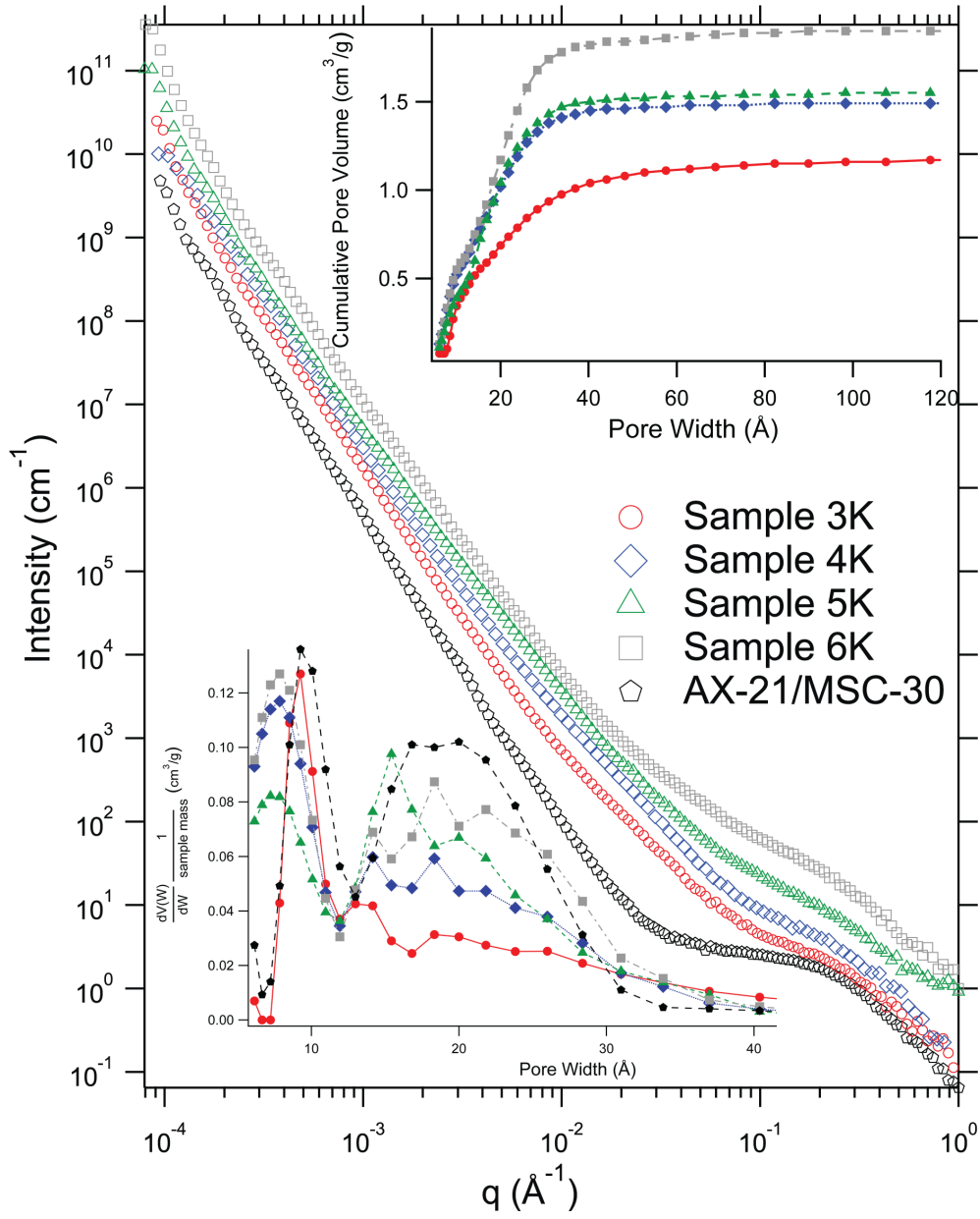


Figure 4.1: USAXS scattering curves of KOH activated carbons 3K, 4K, 5K, 6K, and AX-21/MSC-30. The graphs have been vertically offset for clarity. Bottom left: Pore size distribution of KOH activated carbons. Top right: Cumulative pore volume of KOH activated carbons.

Table 4.1: SAXS porosity, and nominal dimensions of samples 3K, 4K, and AX-21/MS-30, as measured from form factor fits and correlation function fits. The BET surface area and porosity from N₂ experiments are also provided.

Fit method		Sample		
		3K ^a	4K	AX-21/ MSC-30
	Porosity from N ₂ (ϕ_{N_2})	0.78	0.81	0.81
	Porosity from SAXS (ϕ_{SAXS})	0.77	0.83	0.76
	BET surface area (m ² /g)	2500	2600	2600
Method I Cylinder	Width (Å)	6	7	5.5
	Length (Å)	19	25	26
	Pore Volume (Å ³)	540	960	620
	Chi-square (χ^2)	28	1	14
Method I Rectangular box	Side length A (Å)	3.5	3	4
	Side length B (Å)	13	19	13
	Pore Volume (Å ³)	590	970	680
	Chi-square (χ^2)	22	3	10
Method II Correlation function	W_1 (Å)	5.6	6.8	5.8
	C_1 (Å)	1.6	1.4	1.7

^aThe fit interval for sample 3K is $0.1 < q < 1.0 \text{Å}^{-1}$; $0.1 < q < 0.84 \text{Å}^{-1}$ for sample 4K; and $0.03 < q < 1.0 \text{Å}^{-1}$ for sample AX-21/MS-30.

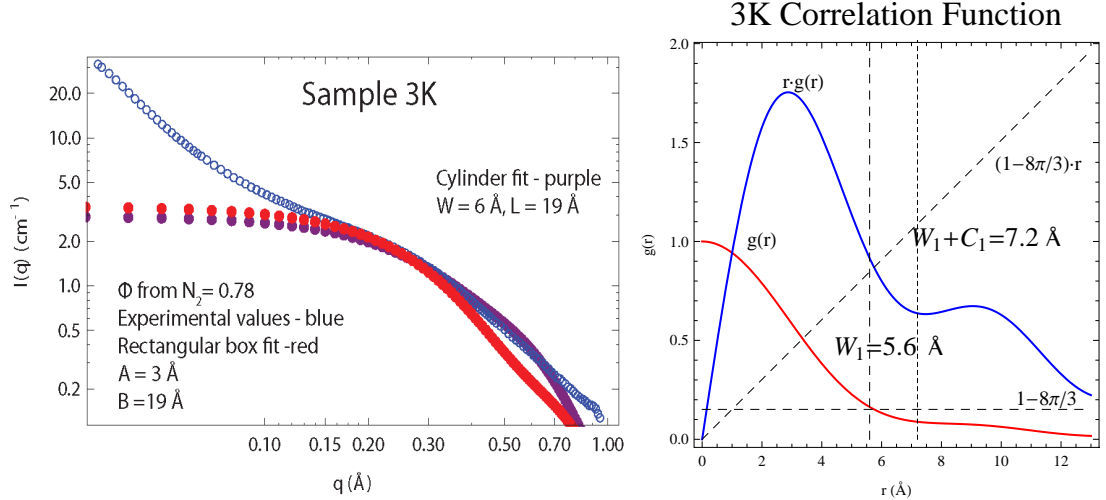


Figure 4.2: Left: Cylindrical (purple) and rectangular box (red) form factor fits for Sample 3K (blue). Right: Correlation function analysis of Sample 3K. The average cylinder width found by graphical construction is $W_1 = 5.6 \text{ Å}$ and the average width of the carbon matrix is $C_1 = 1.6 \text{ Å}$.

There are two significant results here. The first, is that ϕ_{SAXS} and ϕ_{N_2} differ by, at most, a few percent. The second, is that the cylinder width measured using Method I is almost identical to the width found using Method II. This consistency suggests that Sample 3K has cylindrically shaped pores, an assumption that is also supported by the chi-square contour plots presented in Figure 4.3.

Chi-square contour plots

The chi-square plot for the cylinder form factor has a well defined minimum at approximately $W = 6 \text{ \AA}$ and $L = 21 \text{ \AA}$. In contrast, the rectangular box form factor chi-square plot shows multiple minima in the region between $A = 3 : 6 \text{ \AA}$ and $B = 10 : 16 \text{ \AA}$. This implies that local chi-square measurements (restricted to subintervals differing by only a few angstroms) do not give unique solutions to the error minimization problem.

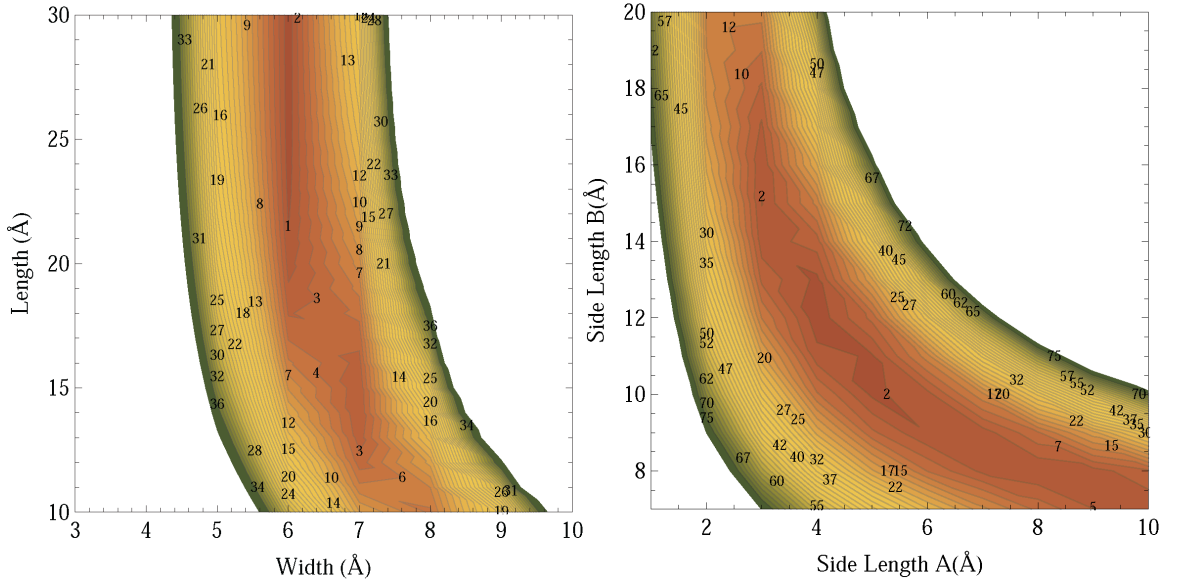


Figure 4.3: Left: Chi-square contour plot for Sample 3K using the cylinder shape form factor. Right: Chi-square contour plot for Sample 3K using the rectangular box form factor. The cylinder chi-square plot shows a minimum suggesting a unique solution. The rectangular box chi-square shows multiple minima suggesting it is not the best model for this sample.

TEM micrographs

TEM micrographs were taken at the Electron Microscopy Core (EMC) at the University of Missouri (Appendix C.1) for a preliminary investigation of Sample 3K (see Figure 4.4). A tentative analysis of the digitally inverted, edge sharpened, contrast enhanced micrographs show locally meandering, approximately cylindrical pores with widths $W \approx 5 - 6 \text{ \AA}$ and linear segments approximately 2-3 nm in length. These measurements show remarkable agreement with the results of the cylinder form factor fit and the correlation function analysis.

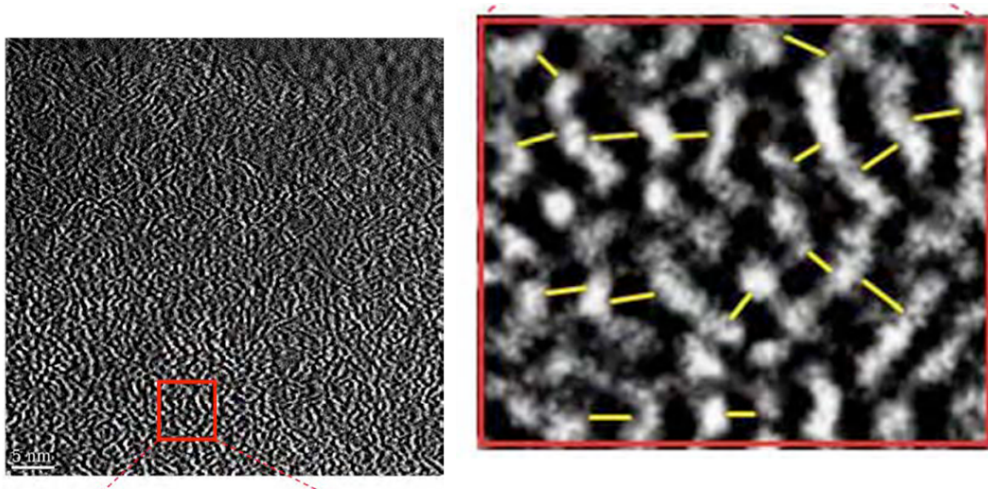


Figure 4.4: Pore widths (yellow lines) in TEM image of 3K. The average width was 5.3 \AA (measured using ImageJ software), in excellent agreement with the value measured from SAXS.

Discussion and conclusion

The chi-square contour plots, correlation function results, TEM micrographs, and line plots ultimately suggest that the cylinder form factor provides the best fit to the experimental data. The large percentage difference between the calculated pore volumes of the cylinder and box suggest that they are not competing models. Cylinders are the best choice.

4.3.2 Method II and the cylinder core-shell model

Method II is restricted to probing very small ranges of length scales. This is due to the fact that, by definition, the correlation function states that there is no new information about sample structure for lengths $r > L_{\max}$ (condition 2 in Section 3.5). We set $r = L_{\max} \approx 15\text{\AA}$ in our analysis because we wish to limit our focus to scattering from individual pores, and avoid considering features at larger length scales. Conceptually, a single pore is surrounded by a particulate carbon matrix shell, that is in turn surrounded by infinite pore space. This scenario can be represented by a set of coaxial cylinders.

Method II assumes that the sample porosity can be evaluated using two nominal lateral pore dimensions, W_1 and C_1 . That is, W_1 and C_1 are fundamental length scales of the system. One way of testing this hypothesis is by investigating whether the knee of the SAXS curve can be modeled using a form factor that depends on one length and two widths.

We wish to investigate if we can successfully work a third length scale into our expression for the scattered intensity. More importantly, we are looking to validate the conceptual model used to measure sample porosity. To do this we must proceed as follows:

1. Find a form factor that is consistent with our conceptual view that a pore and its embedding carbon matrix can be modeled as a set of concentric cylinders.
2. Fit the experimental knee using this form factor. This will confirm that our form factor fairly represents scattering from the nanopores.
3. Measure the ratio of the widths of the cylinder walls. This will give a porosity measurement that is similar in spirit to the one measured using Method II.
4. Confirm that both of the cylinder wall widths measured in (3) are within the restricted interval $1 < r < 15\text{\AA}$.

To do this, we use a cylinder core-shell form factor model (Appendix B.5.4). We

use the notation of Method II to label the cylinder walls.

The core of the cylinder has a width W_1 with electron density $\rho_{W_1} = 0$. It is surrounded by a carbon shell with a width C_1 and electron density $\rho_{C_1} = \rho_e$. The total width of the core-shell system is $W_1 + C_1$. The core-shell is embedded in an infinite pore space with $\rho_{\text{porespace}} = 0$.⁵ A schematic of the cross-section of this system is plotted as an inset in the bottom-left of Figure 4.5.

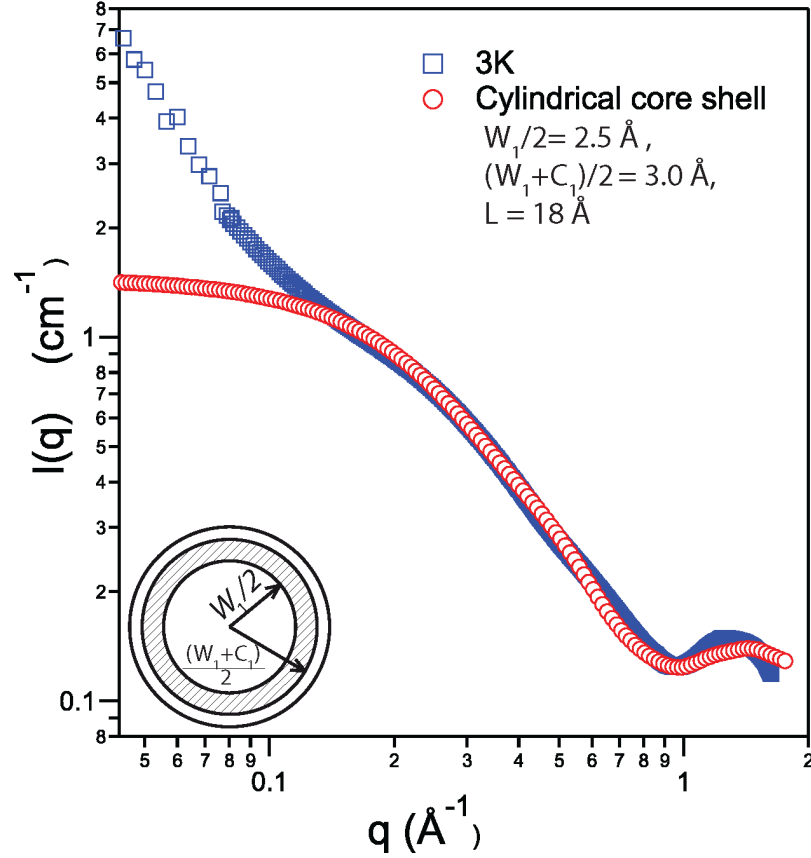


Figure 4.5: Pinhole SAXS data of sample 3K plotted with a cylindrical core-shell form factor with an inner core width $W_1=5.0$ \AA , an outer core width $W_1 + C_1=6.0$ \AA , and length of $L=18$ \AA .

⁵The pore space is drawn as a circle surrounding the carbon shell for conceptual purposes. Its true shape is not known or needed.

Results

The core shell is evaluated using the master formula (Equation (3.4)). Pinhole SAXS data for sample 3K (blue squares) and the core-shell form factor (red circles) are plotted in Figure 4.5. A flat background of 0.1 cm^{-1} is subtracted from the synthetic core-shell curve to approximate beamline resolution effects.

A cylinder core-shell with inner core width $W_1=5.0 \text{ \AA}$, outer core width of $W_1 + C_1=6.0 \text{ \AA}$, and length $L=18 \text{ \AA}$ fits the experimental curve with the proper background subtraction. It gives a SAXS porosity of $\phi_{\text{SAXS}}=0.83$. Recall the values of the cylinder fit, found using Methods I and II, were $W \approx W_1 = 6 \text{ \AA}$, $L=18 \text{ \AA}$, $C_1=1.5 \text{ \AA}$ and $\phi_{\text{SAXS}}=0.78$.

The values of W_1 and C_1 found using the core-shell cylinder form factor are slightly smaller than the values determined using Methods I and II. However, they are well within 10% error of one another. This demonstrates that the pore width and carbon matrix width measured using the correlation function of Method II give results that are in very good agreement with a form factor model that explicitly takes into account two distinct widths. We therefore conclude that our measurement of sample porosity using Method II is a good working approximation.

4.4 Sample 4K: competing models

Sample 4K is prepared with a slightly higher concentration of KOH:C than Sample 3K. Due to the fact that KOH is a harsh activation reagent, we hypothesize that an increase in the ratio of KOH:C will result in an increase in the fractional volume of mesopores in the sample. This is qualitatively confirmed by the PSD and CPV plots (Figure 6.3) in which samples treated with a ratio of $\text{KOH:C} > 3$ show an increase in features with widths in the mesopore size regime. The increase in the cumulative pore volume with increasing KOH concentration also suggests the formation of mesopores.

Although we know that increasing the concentration of KOH causes an increase in pore size and volume, we do not know how it affects pore shape.

Method I and II results

Form factor fits of sample 4K give $W = 7 \text{ \AA}$, $L = 25 \text{ \AA}$ for cylindrical pores and $A = 3 \text{ \AA}$, $B = 19 \text{ \AA}$ for rectangular pores. The 3 \AA length of the short box side suggests a very narrow slit and is viewed with some suspicion. However, the fact that all measurements have an uncertainty of $\pm 2 \text{ \AA}$ somewhat mitigates this concern. The correlation function analysis gives $W_1 = 6.8 \text{ \AA}$, $C_1 = 1.4 \text{ \AA}$, and $\phi_{\text{SAXS}}=0.83$.

The SAXS porosity of Sample 4K is greater than the nitrogen porosity, $\phi_{\text{N}_2}=0.81$. The porosity measured by SAXS should technically be larger than the porosity measured by N_2 , due to the fact that x-rays can probe pores that are inaccessible to nitrogen (Section 5.3.2). However, there are likely few, if any, closed pores given the ratios of KOH:C examined in this chapter.

A notable result is that the nanopore volumes calculated using the two different form factors are almost identical. The cylindrical pore volume is 950 \AA^3 and the rectangular box pore volume is 960 \AA^3 . The small difference between pore volumes suggests that both form factors give suitable fits. This demonstrates the case of competing models.

Chi-square contour plots

The chi-square contour plot supports this claim (Figure 4.6). Each chi-square plot has a well defined minimum as opposed to regions with multiple minima. This implies that both form factors provide a unique solution to the error minimization problem.

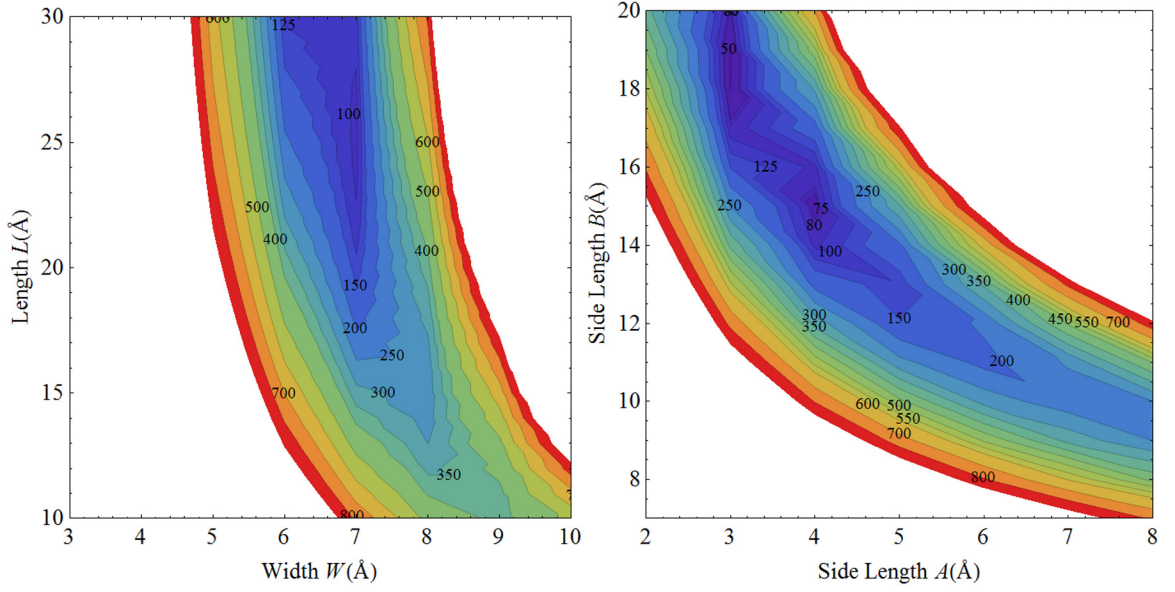


Figure 4.6: Left: Chi-square contour plot for Sample 4K using the cylinder form factor. Right: Chi-square contour plot for Sample 4K using the rectangular box form factor. Both chi-square fits have regions with a minimum, suggesting the fit gives a unique solution.

Discussion and conclusion

Method II provides the supplementary information necessary to decide which fit is best in the case of competing models. The more the results of Method II agrees with Method I, the more likely it is that the cylinder form factor gives a better fit.

For example, the nominal widths obtained using the cylinder form factor fit and correlation function analysis for Sample 4K ($W = 7 \text{ Å}$, $W_1 = 6.8 \text{ Å}$) agree to within one percent, and show the highest level of consistency between Methods I and II of any measurement in this chapter. If the rectangular box gave the best fit, we would expect to see a larger disagreement between W and W_1 . Our ultimate conclusion is that cylinders provide the best fit.

Sample 4K illustrates how measurements made using one component of our analysis can be used to check the consistency of the other. It also reveals that the hallmark of two competing fits is that they have nearly equivalent pore volumes.

4.5 Sample AX-21/MSC-30 : slit-shaped pores

Sample AX-21/MSC 30 is a commercially available activated carbon produced by Kansai Coke and Chemicals Co. Petroleum coke is mixed with KOH and dehydrated at 400 °C, followed by activation in inert atmosphere between 600 and 900 °C [43]. One of the distinctive features of sample AX-21/MSC-30 is the almost horizontal shoulder extending from $0.04 < q < 0.3 \text{ \AA}^{-1}$.

AX-21/MSC-30 is the only sample measured that can be preferentially described as having a slit-shaped pore. Although the cylindrical fit is very reasonable, visual inspection of the line plots (Figure 4.7) and the smaller chi-square value of the box fit (Figure 4.8), suggest this pore is better modeled by the rectangular box.

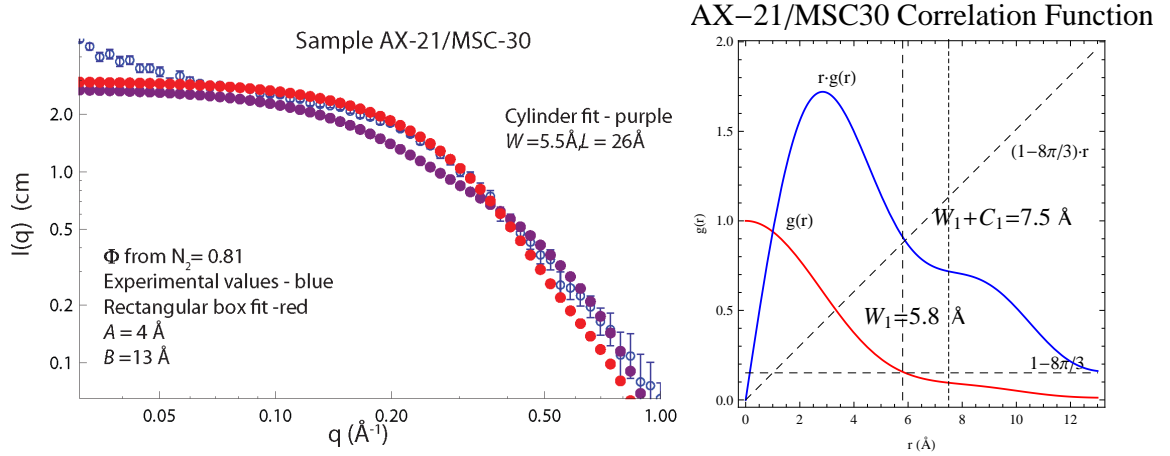


Figure 4.7: Left: Cylindrical (purple) and rectangular box (red) form factor fits for Sample AX-21/MSC-30 (blue). Right: Correlation function analysis of Sample AX-21/MSC-30.

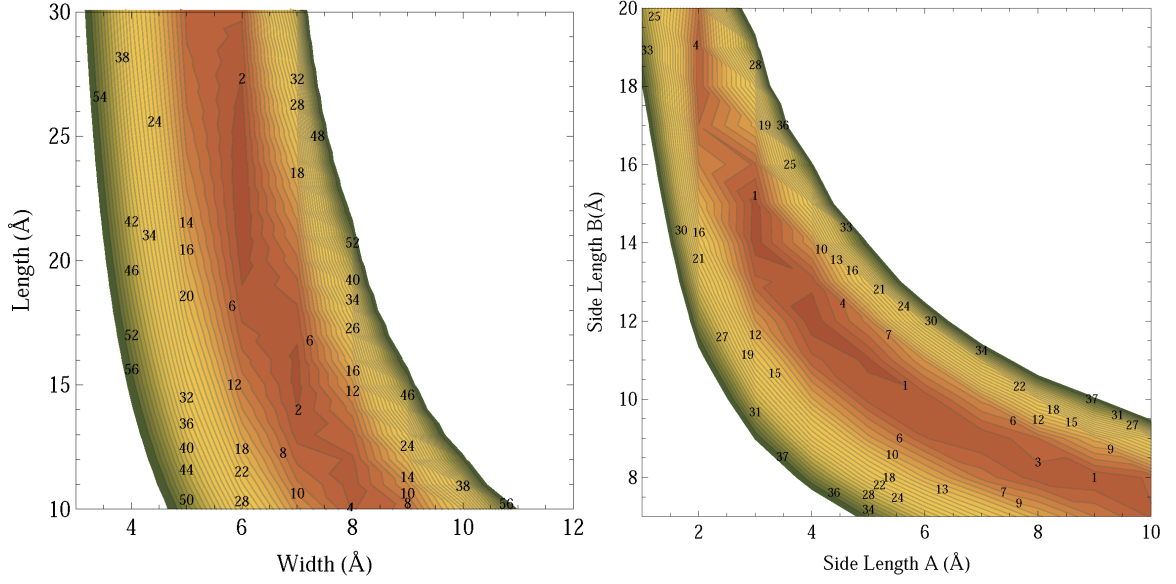


Figure 4.8: Left: Cylinder chi-square contour plot for sample AX-21/MSC-30. Right: Chi-square contour plot for rectangular boxes. From visual inspection of the contour plot the best fit is around $W = 5.5 \text{ Å}$ and $L = 26 \text{ Å}$ for cylinders and $A = 4 \text{ Å}$, $B = 13 \text{ Å}$ for the boxes.

4.5.1 Sample AX-21/MSC-30: demonstration of the weak dependence of Method II on cylindrical geometry

The correlation function analysis of Method II (Section 3.6.2) assumes that pores can be modeled as elongated rods with an oval cross-section. It was mentioned that this assumption is weakly dependent on cylindrical geometry. The fit of Sample AX-21/MSC-30 highlights this dependency.

The measured SAXS porosity for AX-21/MSC-30 is $\phi_{\text{SAXS}}=0.76$, whereas the N_2 porosity is $\phi_{\text{N}_2}=0.81$. Sample AX-21/MSC-30 shows the largest percentage difference between SAXS and N_2 porosities for KOH activated samples.

The pores of samples 3K and 4K are cylindrical, whereas the pores of AX-21/MSC-30 are box-shaped. The cross-section of a slit-shaped pore is rectangular, or square in the limiting case that $B \rightarrow A$. The oval shape cross-section assumed by Method II may, therefore, no longer hold true for the case of Sample AX-21/MSC-30. We

propose that the discrepancy between ϕ_{SAXS} , and ϕ_{N_2} is a consequence of AX-21/MS-30 having a box-shaped cross-section. Nevertheless, a 7% error is still relatively small. This is why the dependence of Method II on the assumption of an oval cross-section is considered to be weak.

4.6 Samples 5K and 6K

4.6.1 Violation of the primary working assumption

Samples 5K and 6K have BET surface areas of 3200 (m^2/g) and 2700 (m^2/g), and porosities of $\phi_{\text{N}_2}=0.81$ and $\phi_{\text{N}_2}=0.80$ respectively. They have a marked increase in mesopore-sized features in their PSDs compared to samples 3K, 4K, and AX-21/MS-30.

The presence of a sizeable mesopore population presents a particular difficulty in applying the characterization method we have developed. Our primary working assumption is that a sample consists of only one size and shape of pore (c.f. Section 3.4). Clearly, a significant amount of mesopores in the sample renders our assumption invalid.

To find a way of characterizing the degree of procedural pathology introduced into our analysis by mesopores, we begin by examining the case in which we know there are none. As we relax this criteria, we find a way to loosely quantify the contribution made by mesopores to the scattered intensity.

It is possible to write the master equation independently of q for very small angles. As stated in Appendix B.4, $P(q) \rightarrow 1$ as $q \rightarrow 0$. If we consider only nanopores we can keep the approximation $S(q) \sim 1$.⁶ As $q \rightarrow 0$, we have $I(q) \propto P(q)=\text{constant}$. That is, the scattered intensity becomes independent of q at some to be determined

⁶If we were to consider large pores at small angles we would obtain the results $P(q) \rightarrow 1$ as $q \rightarrow 0$ and $S(q) \neq 1$. $S(q)$ becomes the dominant term in the scattered intensity at middle q .

point. At this point, the scattered intensity for cylindrical pores is given by

$$\left(\frac{d\Sigma}{d\Omega}\right)_{\text{sample}} = \left(\frac{d\sigma}{d\Omega}\right)_e \left(\frac{\text{no. of electrons} \times \rho_{\text{skel}}}{m_{\text{carbon atom}}}\right)^2 \phi(1-\phi)\pi \left(\frac{W}{2}\right)^2 L = \text{constant}, \quad (4.1)$$

and for rectangular box pores by

$$\left(\frac{d\Sigma}{d\Omega}\right)_{\text{sample}} = \left(\frac{d\sigma}{d\Omega}\right)_e \left(\frac{\text{no. of electrons} \times \rho_{\text{skel}}}{m_{\text{carbon atom}}}\right)^2 \phi(1-\phi)A B^2 = \text{constant}. \quad (4.2)$$

One method of estimating the contribution to the scattered intensity from the mesopores is by evaluating the magnitude of the power law slope, n , of the USAXS curve where we would expect it to be constant if the sample consisted of only nanopores.

For example, Figure B.2 shows that for a fixed pore volume of 565 \AA^3 , $P(q) \rightarrow 1$ at approximately $q = 0.05 \text{ \AA}^{-1}$ for both the box and cylinder form factors. Therefore, any deviation from the horizontal asymptote is due to either a size distribution of nanopores or mesopores. The further the USAXS curve deviates from $n=0$ in this region, the farther the validity of our working assumption is stretched.

We can use a departure from the ideal case corresponding to a monodisperse distribution of nanopores ($n=0$), to establish a working rule of thumb that predicts when an application of our technique will yield fruitful results. We focus on the Transition Region described in Section 3.2.2.

4.6.2 Transition Region power law slope: a metric of applicability

Our analysis is very simple and considers only the slope of the power law in the Transition Region of the USAXS curve. The goal here is not to develop a detailed methodology, but to establish a low-cost metric for determining the applicability of

Methods I and II to an arbitrary nanoporous sample. We take this low-tech approach for the following reasons.

It is difficult to quantify the contribution mesopores make to the scattered intensity without knowing their characteristic size, shape, and texture. For example, smooth mesopores with a very sharp interface will have an intensity that decays as $I(q) \propto q^{-4}$, following the asymptotic Porod law. In this case, mesopore scattering vanishes rapidly and makes little contribution to the intensity at large q values.

Mesopores that have a rough interfacial surface or that are stacked like layered planes of exfoliated graphite will scatter approximately as $I(q) \propto q^{-2}$. Their intensity will decay far more slowly and may give sizeable contributions to the intensity at large angles. They will make it more difficult to discriminate between scattering from nanopores and mesopores within the Transition Region.

For the case of smooth pores, Kalliat *et. al* [40] suggested a model based on the linear superposition of three q^{-4} power laws, one for each population of macropores, mesopores, and nanopores. This detailed expression involves solving for eight unknowns and taking very precise laboratory measurements. We elect to develop a less quantitative and more qualitative approach of accounting for mesopore scattering.

Procedure

USAXS curves are fit to the power law $I_0 q^n$ in the interval $0.1 \leq q \leq 0.2 \text{ \AA}^{-1}$, where I_0 is an arbitrary prefactor. This specific fit interval is chosen because it coincides with the beginning of the nanopore knee in the USAXS curve (see Figure 4.1).

Our primary assumption is that a power law slope of $n=0$ in the Transition Region indicates the achievement of the condition $I(q) \propto \text{constant}$. That is, the horizontal asymptote that signifies that a sample consists of only one size and shape of nanopore, as $q \rightarrow 0$, has been reached.

Measurement outcomes

We consider three possible outcomes of measuring the power law slope, n :

Case 1. $n = 0$. This indicates that $P(q) = 1$ and the intensity of the master formula is given by Equations (4.1) or (4.2). There is no scattering from mesopores or from polydisperse size distributions of nanopores.

Case 2. $0 < n < m$. This indicates that there is some deviation from the ideal value of $n = 0$. Scattering from mesopores or polydisperse size distributions of nanopores give observable contributions to the scattered intensity. However, our primary working hypothesis is still obeyed for the most part. It is possible to successfully fit these samples. The master formula may or may not reduce to a constant as its asymptotic behavior will be slightly masked by scattering from other shapes and sizes of pore.

Case 3. For some value $m > n$ there is a significant scattering contribution from mesopores. The primary working hypothesis is no longer valid and our pore characterization method is no longer applicable. The master formula is not constant because there is an array of different shapes and sizes of pores.

4.6.3 Samples with $n < 1.1$

Samples 3K, 4K, and AX-21/MSC-30 have power law slope values of $n < 1.1$ (Table 4.2). Samples 3K and AX-21/MSC-30 have slopes of $n < 1$. Sample AX-21/MSC-30 has the smallest power law slope and it extends over the largest q range. The PSD of AX-21/MSC-30 shows that it does not have any pores with widths greater than 30 Å. Samples 3K and 4K do have small populations of pores greater than 30 Å, explaining why these samples have steeper power law slopes in the Transition Region. This topic is revisited in Chapter 8.

The fact that samples 3K, 4K, and AX-21/MSC-30 can be fit successfully suggests that for $n < 1$ case 1 or 2 is satisfied, but for $n > 1$ there is the possibility of either case 2, or 3.

4.6.4 Samples 5K, 6K: $n > 1.1$

Samples 5K and 6K have power law slopes of $n > 1.1$. They do not show distinct nanopore knees, and the only part of the curve that can be fit is the small q surface fractal behavior of Region I. Our technique is of little value for these samples. We suggest that, in the Transition Region, a power law slope greater than $n \approx 1.1$ corresponds to the unknown value of m in Case 3.

Sample 5K shows two distinct power laws. To fit this sample at high q would require considering mass or pore fractal structures, or power law size distributions of pores.

Sample 6K shows a very broad shoulder with a small feature at $q \approx 0.2 \text{ \AA}^{-1}$. Fitting sample 6K at large q would require considering both nanopore and mesopore populations. Modeling admixtures of two or more pore sizes can often be accomplished by using a log-normal size distribution of scatterers, power laws, or by using models that consider multiple sizes of pores (polydisperse). They cannot be fit using Methods I and II as they clearly violate our primary working assumption. Therefore a power law slope where $n > 1.1$ corresponds to Case 3.

Table 4.2: Results of power law fits of the form $I_0 q^n$ to the Transition Region ($q = 0.1 - 0.09 \text{ \AA}^{-1}$) of carbons with different KOH:C ratios.

Sample	Prefactor	$I(q) \propto q^n$ n
AX-21/MSC-30	0.82	-0.50
3K	0.22	-0.85
4K	0.31	-1.1
5K	0.25	-1.3
6K	0.33	-1.2

4.7 Discussion of results

Now, that samples 5K and 6K have been discussed, we can point out some advantages and disadvantages of our methodology in comparison to the nitrogen and SAXS studies reported in Section 4.2.

Appealing to these results, we find that the measured cylinder widths of sample 3K and 4K agree with those of Ubago-Perez *et. al* [38] and Figueroa-Torres *et. al* [37]. However, since we were unable to characterize samples 5K and 6K, the range of pore widths (6-11 Å) measured by Takahata *et. al.* [39] cannot be verified. This points to a limitation in our approach as nitrogen adsorption isotherms can apparently measure a wider spectrum of samples.

On the other hand, it can be argued that the quality of information gained from Methods I and II offsets this disadvantage. Not only have we gained information about pore widths from the SAXS analysis, but we have also gained information about pore lengths. For example, we observe that an increase in the ratio of KOH:C not only results in a larger pore width, but a longer pore length. This observation is consistent with the mechanism of KOH activation. It makes little sense for KOH intercalation and oxidation to be restricted to act in a two-dimensional plane. That is, if the width increases, chances are the length does as well. This level of detailed information simply cannot be extracted from an adsorption isotherm.

Looking at the two previous SAXS investigations, we see that both authors measured an R_G of approximately 6Å. Assuming a spherical pore, this corresponds to a pore width of 12Å. Therefore, our data for the width is consistent with the adsorption studies of KOH activated carbon, but not the SAXS studies.

The length $L=20$ Å given by Laszlo *et. al* [42], agrees with the measured length of Sample 3K. However, although these values agree, they are fundamentally different in spirit. The second length measured by this group is a calculation of the inter-particle separation. This is a measurement of the length between particles. The second

length scale provided by our technique gives an additional structural measurement of an individual pore.

4.8 Summary and conclusion

The analytical tools introduced in Chapter 3 were used to evaluate KOH activated nanoporous carbons.

Sample 3K is best fit using the cylinder form factor. This is validated by chi-square contour plots, line plots, and TEM micrographs. The results of this analysis in conjunction with pinhole SAXS data have been used to validate how Method II is used to measure sample porosity. Although limited to probing small length scales, it has been demonstrated that the correlation function of Method II provides a very reasonable estimate of the global sample porosity using two lateral length scales of an individual pore.

Sample 4K demonstrates the case of competing models. The cylinder and box form factor both give reasonable results. We have learned that if the pore volumes calculated from USAXS fits are almost equivalent, regardless of the shape of the form factor model, there is a strong likelihood that both fits are reasonable and are competing models. A series of observations ultimately resulted in the conclusion that the cylinder provides a better fit than the box.

Sample AX-21/MSC-30 is the only KOH activated carbon examined that is preferentially fit using the rectangular box form factor. The fit performed suggests a very short slit-shape pore with nominal dimensions of $4\text{\AA} \times 13\text{\AA} \times 13\text{\AA}$. This sample shows the largest difference between ϕ_{SAXS} and ϕ_{N_2} . It is believed, that this is due to the fact that AX-21/MSC-30 has more of a square than oval cross-section. This violates the weak dependence of the correlation function on cylindrical geometry.

Samples 5K, and 6K could not be successfully fit using our analysis. They were

therefore used to develop a simple metric for evaluating the applicability of our characterization procedure based on the slope of the power law in the Transition Region. Different values of the slopes are explained in terms of the relative number and size of mesopores that may be present.

Chapter 5

Polymeric carbons

In this chapter we apply our characterization technique to carbon samples that are not activated and are made from a polymeric precursor, polyvinylidene chloride (PVDC). Our goal in this chapter is to see how our characterization technique performs when applied to materials that are not KOH activated carbons.

Pore size distributions suggest that PVDC carbons are highly monodisperse and consist exclusively of nanopores at temperatures below 1000°C. As our primary working assumption stresses that pores consist of one size and shape only, PVDC samples should be ideal test cases for our analysis.

In this chapter we examine four different samples prepared from polyvinylidene chloride and verify the general working knowledge that the pore size increases with pyrolysis temperature. The scenario that PVDC carbons may offer case studies in which ϕ_{SAXS} gives a more realistic [44] measurement of sample porosity than ϕ_{N_2} is briefly considered. Finally, one unique specimen demonstrates how SAXS can be used to calculate a sample's specific surface area.

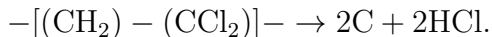
5.1 Introduction

Polymeric carbons are made by the thermal degradation of polymers. They do not graphitize, even when heated above 3000°C [45], and exhibit extensive cross-linking. Polymeric carbons heated below 700°C are commonly referred to as chars. Carbons annealed above 700°C, particularly in small, slow incremental steps to 2500°C are known as glassy carbons. These carbons have a large volume of closed pores [23, 46]. In Section 5.3.2, it is shown how closed pores can lead to discrepancies between SAXS and N₂ porosity measurements.

5.2 Polyvinylidene chloride

The carbonization of PVDC is due to thermal degradation of the polymer(-CH₂-CCl₂-)_n. It has been demonstrated that at temperatures up to 700°C these carbons show considerable open porosity, but at about 800°C cross-linking of carbon atoms reduces spaces between atoms, closing off pores to gas adsorption [14].

It is believed that during heating, effluent HCL gas escaping from the PVDC structure, “drills” very small pores according to the proposed reaction,



PVDC resins begin to decompose at 200°C. Therefore, unlike corn-cob based carbons, they do not require any physical or chemical activation process to create nanopores. For example, Quinn [47] found that pyrolyzed PVDC that was not activated had a considerable pore volume in the 4-6 Å range.

Because the use of an activation agent is not necessary for nanopore formation, the PSDs of these samples are highly monodisperse. By varying the temperature at which pyrolysis is performed, pores can be engineered to different widths.

ALL-CRAFT's main interest in these materials is to use them as laboratories of pores with adjustable widths, in order to systematically test claims that carbons consisting of only sub-nanometer pores can store 5-7 mass% of H_2 at room temperature between 20 and 100 bar [48]. These claims originate from the observation that it is only in these sub-nanometer pores that the negative tails of the van der Waals potential overlap. This creates a deep negative potential well that almost doubles the adsorption energy [16, 21, 49].

5.2.1 Previous SAXS investigations

Initial studies combining SAXS and wide-angle x-ray scattering (WAXS) investigations of PVDC were performed at large scattering angles, between 1-9 Å, with the goal of observing (hkl) reflections from individual graphitic layers [50, 51].

Fitzer [52] and Perret [53] made the observation that polymeric carbons generally demonstrate an increase in scattered intensity with heat temperature treatment. That is, pore sizes increase as the sample temperature is increased, a trend confirmed in Section 5.3. Rothwell [23] confirmed the general observation of Fitzer and Perret for the specific case of glassy carbons. He demonstrated that pores increase in size up to 3000°C at which point they resemble a uniform distribution of spheres with widths of 50 Å.

No form factor based SAXS studies have been conducted on PVDC. However, very thorough adsorption studies add to the good working knowledge of PVDC's structure [15, 54].

5.3 Results and discussion

Four PVDC samples S11, S8;4B^b, S3;5B^a, and S7 are examined in this chapter and were fabricated under the conditions listed in Table 5.1. Sample S7 is not considered

Table 5.1: Fabrication conditions of samples S11, S3;5Ba, S8;4Bb, and S7.

Sample	Fabrication Conditions
S11	Polyvinylidene chloride charred at 850°C
S3;5B ^a	Polyvinylidene chloride charred at 480°C, then heated with boric acid at 480°C
S8;4B ^b	Polyvinylidene chloride mixed with 1,2-Bis(hydroxymethyl) carborane or C ₂ B ₁₀ Diol and heated up to 790°C
S7	Polyvinylidene chloride pyrolyzed at 850°C

until Section 5.4.

The dependence of pore width on pyrolysis temperature is confirmed by the nitrogen data in Figure 5.1, where it is seen that a higher temperature of pyrolysis corresponds to a larger CPV. Samples S11, S8;4B^b, and S3;5B^a were pyrolyzed at temperatures of 850°C, 790°C, and 490°C respectively. They have CPV of 0.52 cm³/g, 0.38 cm³/g, and 0.29 cm³/g respectively. The dependence of the CPVs on temperature is plotted as an inset in the USAXS scattering curve plot (Figure 5.1).

The dependence of pore size on temperature is observed at large q based on the height of the nanopore knee.¹ The knee with the largest scattered intensity in Region II corresponds to the sample fabricated at the highest temperature. The knee with the smallest scattered intensity corresponds to the sample fabricated at the lowest temperature. At smaller values of q , the intensity of S3;5B^a is greater than S11 and S8;4B^b.² Regardless, the scattered intensity in Region II of Sample S3;5B^a is the weakest of the three samples.

¹This argument assumes that the CPV and the amplitude of the scattered intensity are indicators of the relative pore size in highly monodisperse, uniform samples, that consist only of nanopores.

²This discrepancy could be due to an erroneous measurement of the sample thickness.

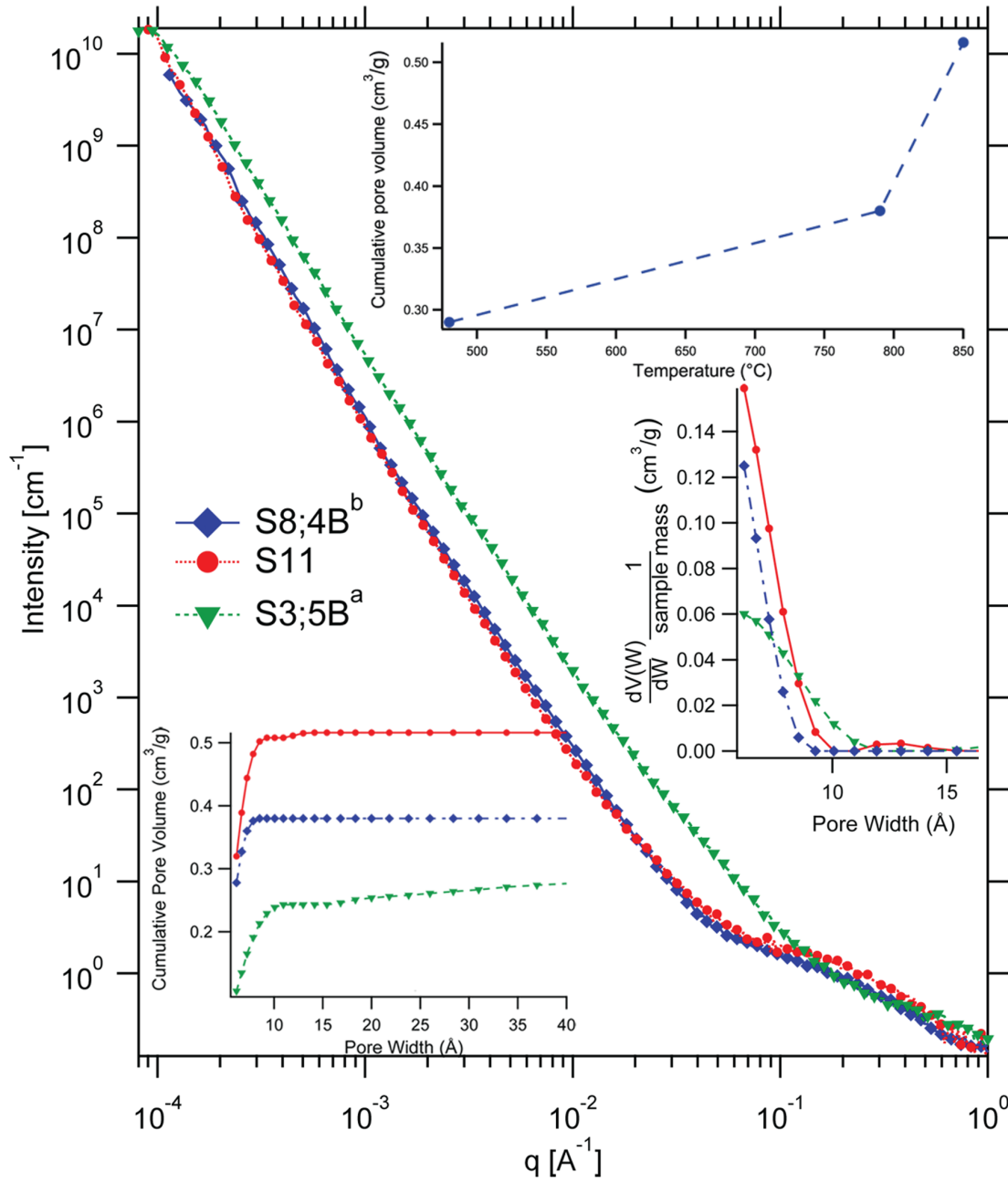


Figure 5.1: USAXS curves, PSD, and CPV of the pyrolyzed, unactivated PVDC samples S11 (red circles), S8;4B^b (blue diamonds), and S3;5B^a (green triangles). A plot of the cumulative pore volume vs. pyrolysis temperature is plotted in the upper-right hand corner.

Methods I and II

By comparing the results of the three PVDC samples, we can enhance the working knowledge of our methodology.

Sample S11 is easily characterized using Methods I and II with the cylinder form factor fit. The nominal pore width and length are $W=4\text{ \AA}$ and $L=25\text{ \AA}$, respectively (Table 5.2). However, samples S8;4B^b and S3;5B^a are more difficult to characterize. These samples cannot be fit with the rectangular box form factor. Sample S11 cannot be fit reasonably using this form factor either.

The chi-square statistic of Sample S11 is $\chi^2=19$ for the cylinder fit and $\chi^2=62$ for the box fit (Figure 5.3 and Table 5.2). In addition to having a chi-square value that is a factor of four larger than that of the cylinder fit, the dimensions measured using the box fit are not physically reasonable.

Even though all measurements of pore dimensions have an uncertainty of at least $\pm 2\text{ \AA}$, the measured fit value for side A is 1.8 \AA . In natural graphite the C-C bond length is only 1.4 \AA . A true measurement of $A=1.8\text{ \AA}$ would imply that SAXS resolves features well within the traditional XRD regime, at the atomic length scale. We know this is not the case.

Despite the success of fitting sample S11 using the cylinder form factor, the dimensions of the cylinder fit for samples S8;4B^b and S3;5B^a give length scale ratios that suggest unexpectedly long pores. These results are likely unreliable.

Table 5.2: SAXS porosity and nominal dimensions of samples S11, S3;5B^a, and S8;4B^b measured from form factor fits and correlation function analysis. Unlike the case of KOH activated samples, PVDC samples cannot be fit well with the rectangular box form factor.

Fit method		Sample		
		S11 ^a	S3;5B ^a	S8;4B ^b
	Porosity from N ₂ (ϕ_{N_2})	0.52	0.37	0.45
	Porosity from SAXS (ϕ_{SAXS})	0.71	0.70	0.70
	BET surface area (m ² /g)	850	690	1060
Method I Cylinder	Width (Å)	4.3	9	3.4
	Length (Å)	25	4	30
	Pore Volume (Å ³)	290	110	270
	Chi-square (χ^2)	19		
Method I Rectangular box	Side length A (Å)	1.8		
	Side length B (Å)	12		
	Pore Volume (Å ³)	310		
	Chi-square (χ^2)	22		
Method II Correlation function	W_1 (Å)	4.5	4.3	4.3
	C_1 (Å)	1.8	1.8	1.9

^aThe fit range for sample S11 and S3;5B^a is $0.1 < q < 1.0 \text{ Å}^{-1}$; $0.07 < q < 1.0$ for sample S8;4B^b.

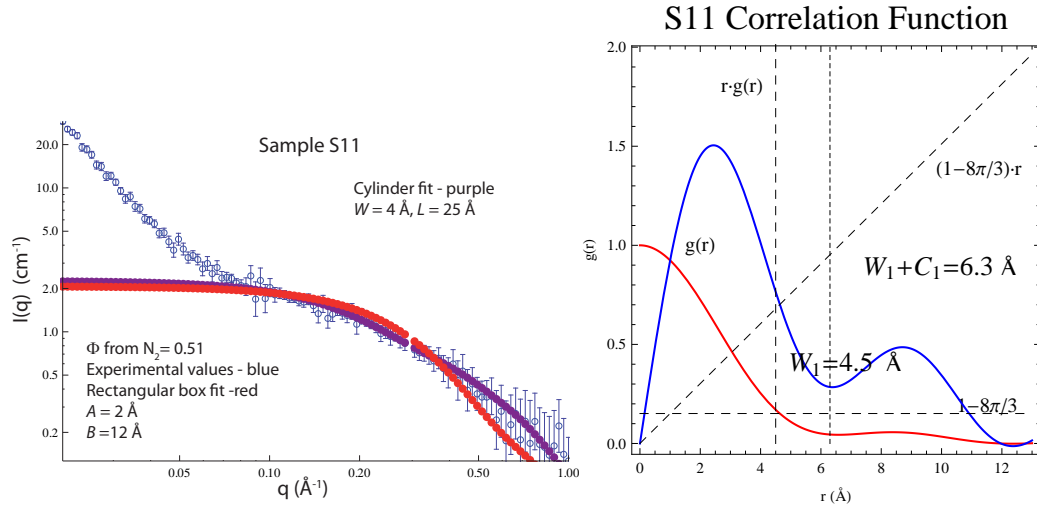


Figure 5.2: Left: Cylindrical form factor fit (purple) and rectangular box form factor fit (red) for Sample S11 (blue). Right: Correlation function analysis for Sample S11.

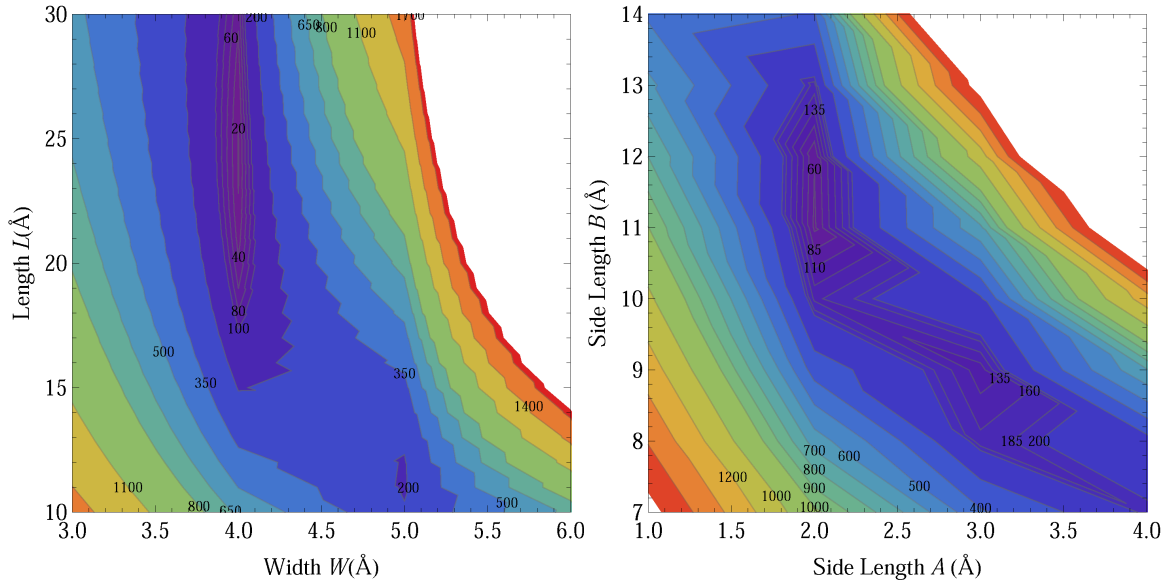


Figure 5.3: Left: Chi-square contour plots of sample S11 using the cylinder form factor. Right: Chi-square plots of Sample S11 using the rectangular box form factor. $\chi^2=19$ for the cylinder and $\chi^2=62$ for the rectangular box form factor fits.

5.3.1 A new constraint on sample characterization

The reason these samples cannot be fit properly is due to the fact that the amplitude of the scattered intensity in Region II is too small. A close look at Figure 5.1 shows that Sample S11 is the only sample whose knee has a scattered intensity greater than 1 cm^{-1} . The CPV of Sample S3;5B^a is not even half that of S11. Simply stated, there is not enough pore present to be measured in samples S3;5B^a and S8;4B^b.

We therefore find an additional constraint that must be met for a successful analysis. The sample must have some minimal pore volume in order to register successfully on the USAXS instrument. It appears that samples with a cumulative pore volume less than roughly $0.4 \text{ cm}^3/\text{g}$ give suspicious results. This issue might be resolved by simply measuring these samples on a pinhole SAXS instrument.

5.3.2 The utility of Method II: a comparison of ϕ_{SAXS} and ϕ_{N_2}

The values of ϕ_{SAXS} and ϕ_{N_2} for Sample S11 present very different pictures of sample porosity. The SAXS porosity is $\phi_{\text{SAXS}}=0.71$ whereas the nitrogen porosity is $\phi_{\text{N}_2}=0.52$. This discrepancy is partially resolved if we consider Sample S11 to be partially glass-like. As stated at the beginning of the chapter, above 700°C polymeric carbons begin to form extensive cross-linked networks that eventually result in completely close pores at temperatures of approximately 3000°C.

Heating Sample S11 to 850°C likely promotes the formation of closed pores. Nitrogen is restricted to probing only open pores. X-rays on the other hand, do not have this limitation and are able to sample the entire pore space.

If the porosity of a system with closed pores is measured with x-rays, it should be larger than if it were measured using nitrogen adsorption-desorption isotherms. It is possible that this is the case for Sample S11 and that the SAXS porosity is the more accurate measurement. Unfortunately, a third measurement technique would be necessary to justify this assertion.

We note that only small differences between ϕ_{SAXS} and ϕ_{N_2} were observed when characterizing KOH activated carbons. This is consistent with the fact that KOH activated samples have few, if any, closed pores.

5.4 Sample S7:surface area from SAXS

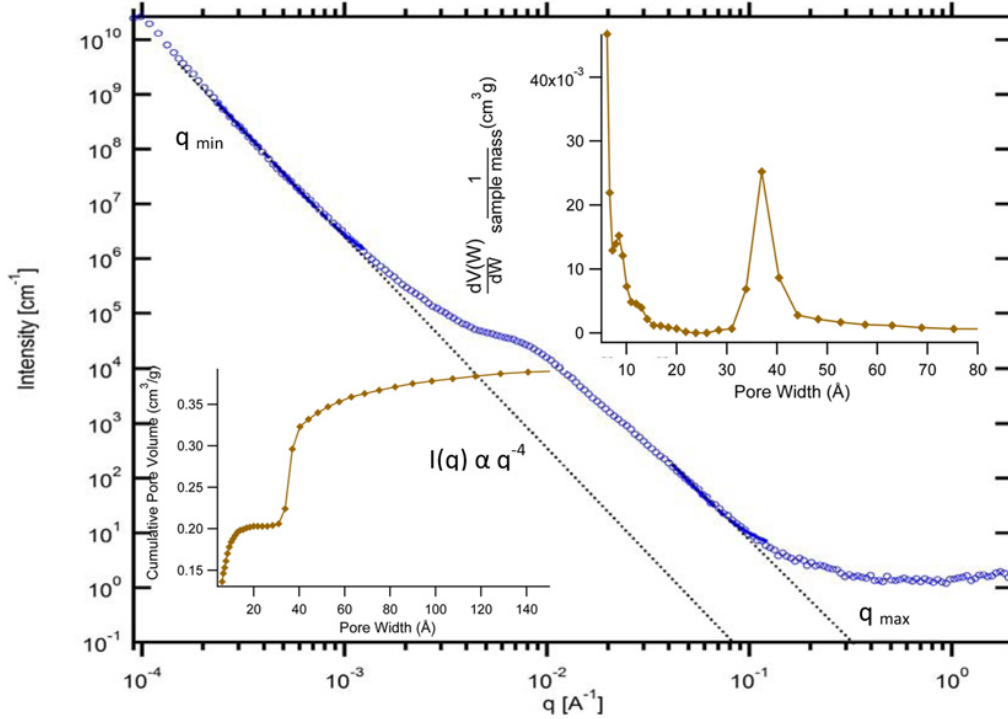


Figure 5.4: USAXS curve, PSD, and CPV of Sample S7. This is the only ALL-CRAFT sample illustrating the asymptotic Porod law. This allows the specific surface area of the sample to be calculated using SAXS.

Sample S7 is the only ALL-CRAFT sample that exhibits the asymptotic Porod law, $I(q) \sim q^{-4}$. In fact, two Porod regions are seen in Sample S7 (Figure 5.4).

The first q^{-4} power law has an upper cutoff $q=3.5 \times 10^{-3} \text{ \AA}^{-1}$ and an inner cutoff of $q=1.0 \times 10^{-3} \text{ \AA}^{-1}$. The second q^{-4} power law has an upper cutoff $q=8.2 \times 10^{-3} \text{ \AA}^{-1}$, suggesting a structural unit of 800 Å. The sample is then smooth from $8.2 \times 10^{-3} < q < 0.17 \text{ \AA}^{-1}$, or at length scales between 37 and 800 Å, with the inner cutoff suggesting a structural feature of approximately 37 Å. The q^{-4} behavior is then masked by pores with widths less than 37 Å. The PSD of S7 is bimodal, with its second peak occurring at 35 Å.

The presence of q^{-4} scattering behavior makes Sample S7 amenable to specific

surface area (Σ)(m²/g) calculations. This is traditionally found using the relation

$$\Sigma = \frac{\pi\phi(1-\phi)}{\rho_{\text{skeleton}}} \frac{\lim_{q \rightarrow \infty} [I(q) q^4]}{\int_0^\infty I(q) q^2 dq}. \quad (5.1)$$

The integral $\int_0^\infty I(q) q^2 dq$ gives a quantity known as the Porod invariant, Q (cm⁻⁴). The modified Porod invariant is found using an alteration of this procedure that allows the subtraction of background noise at large q [55].

In this procedure, a plot of $I(q) \cdot q^{-4}$ vs q^{-4} is fit using the linear form $I(q) = K + bq^{-4}$. The values of b and K are the slope and intercept of the fit, respectively. A background corrected, discrete form of the Porod invariant is found using the expression

$$Q = \Delta q \sum_{q_{\min}}^{q_{\max}} (I(q) - bq) q^2 + K/q_{\max}$$

where q_{\min} and q_{\max} are the values of q corresponding to the first point of the first Porod scattering region, and the last point of the second Porod scattering region, respectively.

The specific surface area is found using the relation

$$\Sigma = 10^4 \pi \phi (1 - \phi) (K / (Q \rho_{\text{skeleton}})).$$

Using the values $\phi_{\text{N}_2}=0.46$, $\rho_{\text{skeleton}}=2.0\text{g/cm}^3$, $q_{\min}=3.5 \times 10^{-3} \text{ \AA}^{-1}$, $q_{\max}=0.23 \text{ \AA}^{-1}$, and the fit values of $K=1.4 \times 10^{-2}$ and $b=8.3 \times 10^{-3}$, gives a surface area measurement of approximately $\Sigma = 580 \text{ m}^2/\text{g}$.

This is in excellent agreement with the BET surface area analysis value of $\Sigma=625 \text{ m}^2/\text{g}$. The result demonstrates that given the proper conditions, SAXS can, in theory, yield sample porosity, pore shape, pore dimensions, and specific surface area.

5.5 Summary and conclusion

Our analysis of PVDC carbons confirms that the pore size increases with pyrolysis temperature.

PVDC samples could not be fit using the box form factor and, except for Sample S11, were fit rather poorly using the cylinder form factor as well.

The incredibly monodisperse population of nanopores thought to be ideal for testing our methodology, turned out to be too ideal. The pore volume of samples S8;4B^b and S3;5B^a proved to be at the edge of the detection for the USAXS instrument.

This does not necessarily indicate a flaw in our analysis or in the USAXS instrument. PVDC samples may still provide the opportunity to benchmark our characterization method. To test this hypothesis, samples need to be measured on a pinhole SAXS instrument. This will provide the resolution necessary to evaluate the very slender features of PVDC samples. A new criteria for a successful analysis using the USAXS instrument is proposed. The cumulative pore volume of the sample must exceed approximately 0.35 cm³/g.

Finally, we illustrated that if scattering follows a power law where $I(q) \propto q^{-4}$, the specific surface area of a sample can be calculated using the modified Porod invariant.

Chapter 6

Boron-doped and irradiated activated carbons

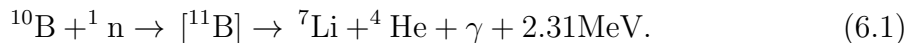
Two boron-doped samples and one boron-doped irradiated sample are investigated in this chapter. The structure of the boron-doped sample, 3K-H6 (II,A), is examined before and after one minute of irradiation. Then sample 3K*¹, boron-doped using two different methods, is interpreted using a very light fractal analysis.

6.1 Introduction

In order to realize the large binding energies predicted by boron-doping activated carbons - 10-13.5 kJ/mol [56]- ALL-CRAFT began evaluating different boron doping methods. These methods include boron-doping by impregnation using synthetic boron containing compounds or thermolysis of B₁₀H₁₄ (decaborane). In addition to serving as a dopant that would increase the H₂-graphene binding energy, boron was chosen in particular for another reason.

¹The star annotation, denotes that the sample was prepared in an alumina crucible in order to avoid contamination from Fe, Cr, and other metals.

When irradiated with thermal neutrons, the capture of a neutron by the ^{10}B isotope results in the following reaction [49]



It is believed that the alpha particle drills additional pore space and that the lithium provides additional centers for adsorption. Estimates of surface areas as high as 6,000 m²/g have been calculated.

6.1.1 SAXS for evaluating boron-doped carbons

Unfortunately, the exciting and beneficial increases in storage performance that result from boron-doping cannot be measured by SAXS. Even the structural impact that the boron-doping procedure has on its parent carbon is undetectable.

Although the addition of boron technically makes our system a three phase system, it changes our analysis very little. This is due to the fact that the number of electrons in boron is essentially identical to the number in carbon. This results in only a small change in $(\Delta\rho)^2$. Consequently, SAXS will not by-in-large discriminate between a pure carbon sample and a sample that is a mixture of carbon and boron.

The one caveat to this statement, that illustrates where SAXS can be quite useful in monitoring the boron doping process (Section 6.3), is if the boron is not successfully embedded within the carbon matrix. The change in $(\Delta\rho)^2$ before and after doping is still trivial in this case; however, secondary structures that form exterior to the pore (e.g. pore clogging) will be visible to x-rays as structural inhomogeneties.

A very positive way of looking at the fact that carbon and boron have nearly identical numbers of electrons is that the tools we have developed should be fully transferable to boron-doped samples. In fact, SAXS can provide a significant consistency check for boron-doped samples. Comparing measurements before and after

doping can help ensure that the process itself has not significantly distorted the structure of its parent carbon.

6.2 Samples 3K-H6 (II,A) and 3K-H6 (II,A) Irr. 1 min.

Sample 3K-H6 (II,A)² is prepared by saturating sample 3K with decaborane vapor followed by thermolysis. It is then annealed at 600°C in a high-pressure stainless steel container. Sample 3K-H6 (II,A) Irr. 1 min. is sample 3K-H6 (II,A) subjected to one minute of irradiation at the University of Missouri Research Reactor (MURR).

Nitrogen data fails to illustrate a difference before and after irradiation. Examination of the nitrogen CPV and PSD data (Figure 6.1) gives the impression that the structure of both samples are identical.

The USAXS data also suggests that the structure in Region II isn't changed by the irradiation treatment.³ The poor quality of the data at large q prevents the calculation of correlation functions with well-defined values. Consequently, SAXS porosities cannot be measured for these samples. Chi-square contour plots are also unmerited due to the large error that will result from the poor resolution of the data in Region II.⁴ Form factor fits however, are still possible.

²See Appendix C.7 for a description of Method (II,A).

³The difference observed at smaller q between Sample 3K-H6 (II,A) and 3K-H6 (II,A) Irr. 1 min. may even be the result of an instrument upgrade performed in the summer of 2009. Sample 3K-H6 (II,A) was measured before the upgrade, while 3K-H6 (II,A) Irr. 1 min. was measured afterwards.

⁴Prior to the upgrade approximately 70-90 data points were collected per scan. After the upgrade, approximately 170-210 data points were collected per scan. The samples presented in earlier chapters were measured after the upgrade.

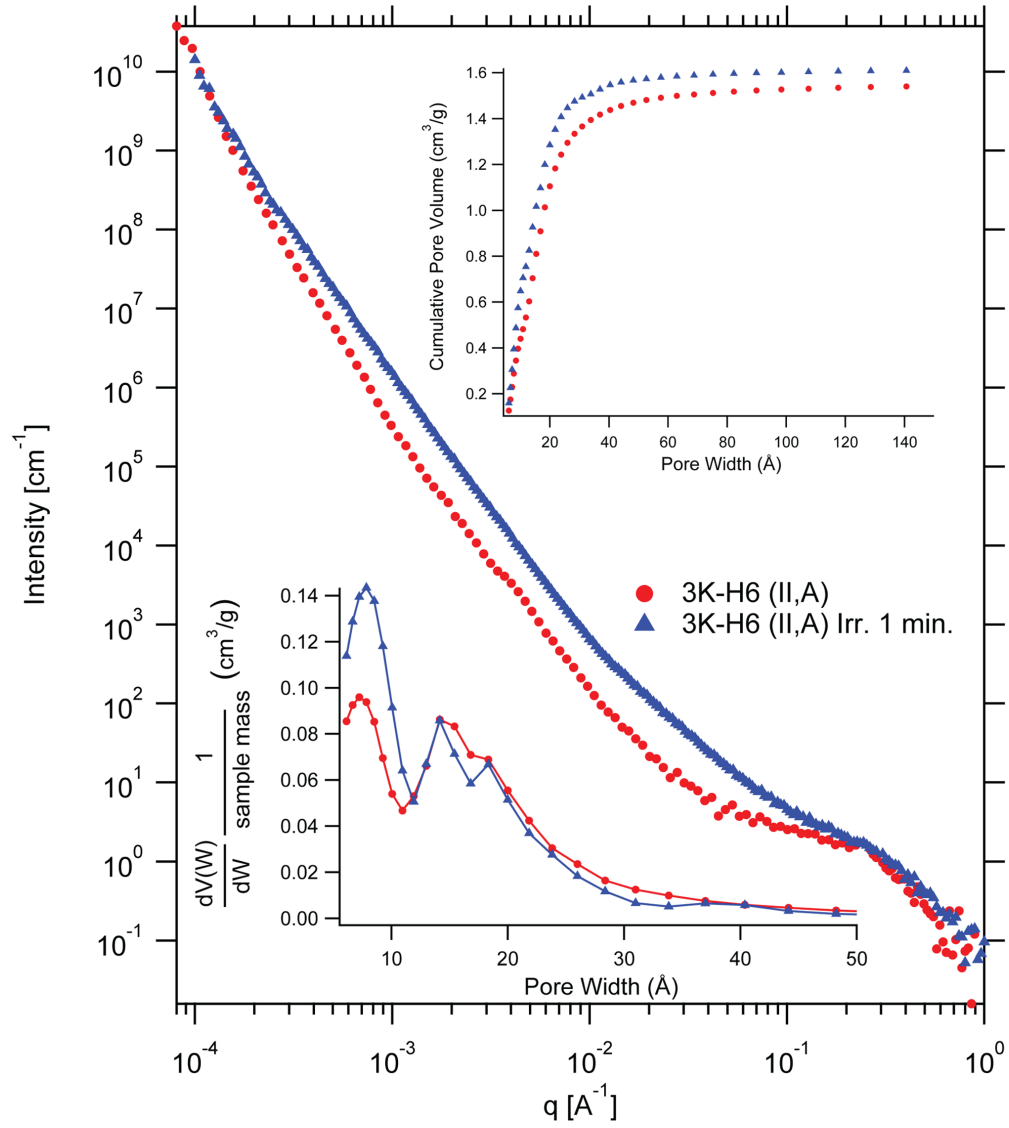


Figure 6.1: Samples 3K-H6 (II,A) (red open circles) and 3K-H6 (II,A) Irr. 1 min. (open blue triangles). The two samples are almost identical in Region II. The CPV and PSD from N₂ are plotted as insets.

6.2.1 Form factor fits

The form factor fits of samples 3K-H6 (II,A) give $W=5.7 \text{ \AA}$, $L=23 \text{ \AA}$ and $W=6 \text{ \AA}$, $L=24 \text{ \AA}$ for samples 3K-H6 (II,A) and 3K-H6 (II,A) Irr. 1 min., respectively (Table 6.1). Given that the uncertainties in the measurements are on the order of $\pm 2 \text{ \AA}$, they can be considered the same.

The side lengths of the rectangular box fits are $A=3.7 \text{ \AA}$, $B=12 \text{ \AA}$ and $A=4.4 \text{ \AA}$, $B=12 \text{ \AA}$ for sample 3K-H6 (II,A) and 3K-H6 (II,A) irr. 1 min., respectively. We claim these measurements can also be considered the same.

Table 6.1: Nominal dimensions of samples 3K-H6 (II,A) and 3K-H6 (II,A) Irr. 1 min. measured using form factor fits. There are no correlation function or ϕ_{SAXS} results due to the fact that the data did not give well defined values. The BET surface area and porosity from N_2 experiments are listed.

Fit method		Sample	
		3K-H6 (II,A) ^a	3K-H6 (II,A) Irr. 1 min.
	Porosity from N_2 (ϕ_{N_2})	0.77	0.78
	Porosity from SAXS (ϕ_{SAXS})	-	-
	BET surface area (m^2/g)	3300	3000
Method I Cylinder	Width (\AA)	5.7	6
	Length (\AA)	23	24
	Pore Volume (\AA^3)	590	680
	Chi-square (χ^2)	28	1
Method I Rectangular box	Side length A (\AA)	3.7	4.4
	Side length B (\AA)	12	12
	Pore Volume (\AA^3)	530	630
	Chi-square (χ^2)	22	3
Method II Correlation function	W_1 (\AA)	-	-
	C_1 (\AA)	-	-

^aThe fit interval for sample 3K-H6 (II,A) and 3K-H6 (II,A) Irr. 1 min is $0.1 < q < 1.0 \text{ \AA}^{-1}$.

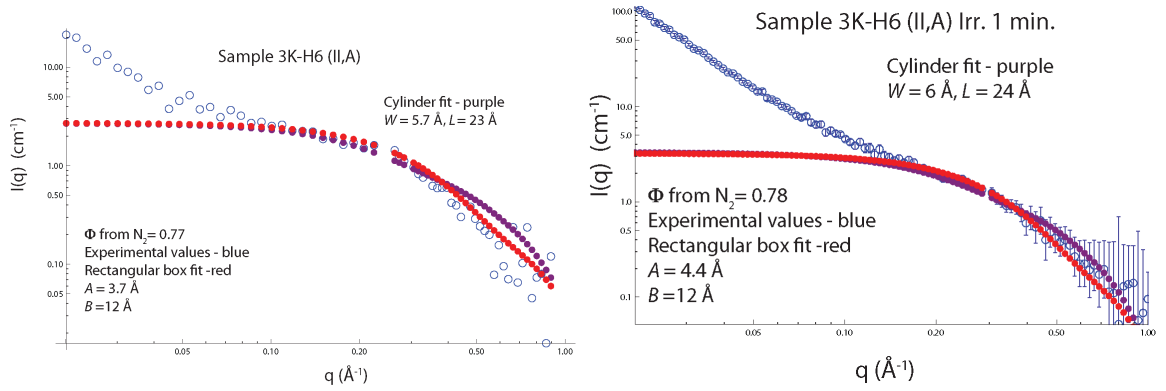


Figure 6.2: Left: Cylindrical (purple) and rectangular box (red) form factor fits for Sample, 3K-H6 (II,A) (blue). Right: Cylindrical and rectangular form factor fits for Sample 3K-H6 (II,A) after being irradiated for 1 minute. There is no significant difference in the measured widths or lengths of either form factor that is caused by the irradiation treatment.

6.2.2 Discussion

The results of our brief SAXS analysis confirms what is suggested by the nitrogen data, that there is no significant structural difference between Sample 3K-H6 (II,A) and Sample 3K-H6 (II,A) Irr. 1 min.

The advantage provided by the SAXS analysis is that it demonstrates that neither the width, nor the length of 3K-H6 (II,A) changed outside of the margin of error. Nitrogen measurements only indicate that the distribution of a pore width did not change. Again, we return to the recurring theme that SAXS data gives information about two characteristic lengths, whereas nitrogen data provides information about one characteristic length.

6.2.3 Hydrogen results

Although SAXS and nitrogen present a consistent story of samples 3K-H6 (II,A) and 3K-H6 (II,A) Irr. 1 min, hydrogen isotherms present a different picture. The measured gravimetric excess adsorption ($G_{\text{ex,H}_2}$) at 80 K and 50 bar is 49 g/kg for

3K-H6 (II,A) and 47 g/kg for 3K-H6 (II,A) Irr. 1 min. This seems to support the conclusion that irradiation does not change the sample structure.

However, an analysis of the pressure at which the local maximum in the excess adsorption occurs indicates that the binding energy increases from 6.2 kJ/mol (3K-H6 (II,A)) to 6.5 kJ/mol (3K-H6 (II,A) Irr. 1 min.) after irradiation. This implies that both nitrogen and SAXS provide insufficient measuring sticks for characterizing these novel materials.

Dr. Peter Pfeifer [57] has suggested that this phenomena may be due to discontinuities at the edges of newly created pores from fission tracks. The question as to whether hydrogen sees the same surface area as nitrogen and SAXS is an exciting item for future investigation.

6.3 Samples 3K*, 3K*-H6 (II,A), and 3K*-H7 (I,A)

Samples 3K*-H6 (II,A) and 3K*-H7 (I,A)⁵ are boron-doped samples with 1.6 wt.% and 6.9 wt.% boron (from prompt-gamma activation analysis spectrometer (PGAA)), respectively. The fabrication conditions and B:C ratios are listed in Table 6.2.

The parent compound for both samples is 3K*, which has a scattering curve similar to 3K. That is, there is a distinct nanopore knee at large q ($q \sim 0.02 - 0.05 \text{ \AA}^{-1}$) (Figure 6.3). Sample 3K* is best fit using a rectangular box with nominal dimensions $A = 3 \text{ \AA}$ and $B = 13 \text{ \AA}$ (Figure 6.4).

⁵See Appendix C.6.1 for a description of Method (I,A).

Table 6.2: Fabrication conditions and boron wt.% for samples 3K*, 3K*-H6 (II,A), and 3K*-H7 (I,A).

Sample	Fabrication method	B:C
3K*	3 KOH:C	
3K*-H6 (II,A)	3 KOH:C \rightarrow B ₁₀ H ₁₄ deposited as thin liquid film followed by thermal decomposition of B ₁₀ H ₁₄ /B _{10x} H _z	1.6 wt.%
3K*-H7 (I,A)	3 KOH:C \rightarrow submonolayer of B _{10x} H _z is created by thermal decomposition of B ₁₀ H ₁₄ liquid/vapor followed by thermal decomposition of B _{10x} H _z	6.9 wt.%

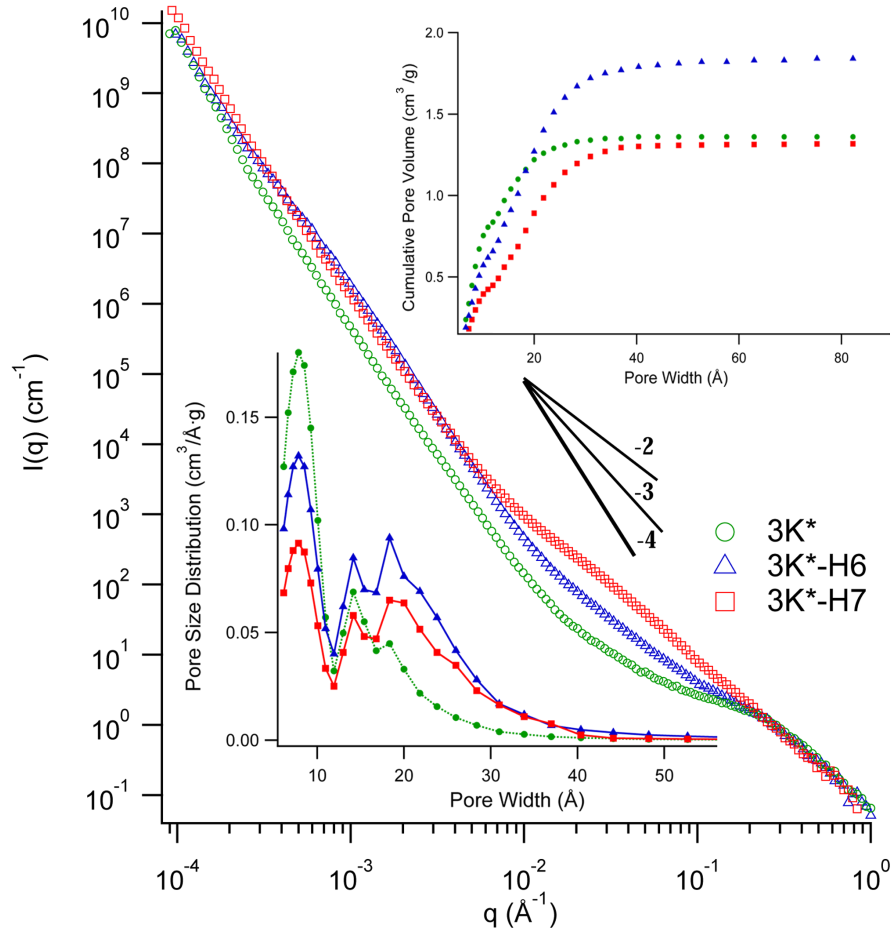


Figure 6.3: USAXS curves of samples 3K* (green open circles), 3K*-H6 (II,A) (blue open triangles), and 3K*-H7 (I,A) (red open squares). The three samples have the same surface fractal dimension, $D_s = 2.4 \pm 0.1$. Sample 3K* shows the familiar nanopore knee, however samples 3K*-H6 (II,A) (1.6 wt.% boron) and 3K*-H7 (I,A) (6.9 wt.% boron) exhibit a second power law with fractal dimensions $D = 1.7 \pm 0.1$ and $D = 2.1 \pm 0.1$ respectively.

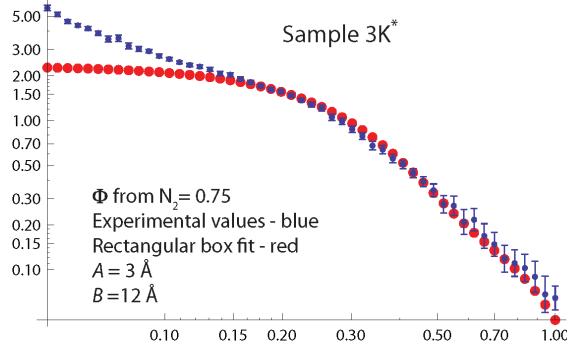


Figure 6.4: Sample 3K* fit using the rectangular box fit. Unlike samples 3K*-H6 (II,A) and 3K*-H7 (I,A), Sample 3K* clearly shows a nanoporous knee that is similar to Sample 3K.

In contrast to 3K*, samples 3K*-H6 (II,A) and 3K*-H7 (I,A) lack the nanopore knee and instead exhibit two distinct, independent power laws. The small q power law ($q \leq 10^{-2} \text{Å}^{-1}$) in all three samples is consistent with surface fractal behavior. In fact, all three samples share a common surface fractal dimension, $D_s = 2.3 \pm 0.1$ (Table 6.3).

Sample 3K*-H6 (II,A), 1.6 wt.% boron, demonstrates an increased BET surface area and porosity in comparison with its parent sample 3K*. In contrast, Sample 3K*-H7 (I,A), 6.9 wt.% boron, shows a decrease in surface area and porosity in comparison with 3K*.

Since the three samples have the same surface fractal dimension, but different BET surface areas and porosities, it can be concluded quite generally that D_s is not correlated with either of these measurements. The differences in the measured BET surface areas and porosities, therefore, must originate from the point at which the three samples diverge on the USAXS curve, $q \geq 0.02 \text{Å}^{-1}$.

Table 6.3: Porosity, BET surface area, and surface fractal dimension D_s (with inner and outer cutoffs) for samples 3K*, 3K*-H6 (II,A), and 3K*-H7 (I,A). The fractal dimension D (with inner and outer cutoffs) for the large q power laws observed in samples 3K*-H6 (II,A), and 3K*-H7 (I,A). The inner and outer cutoffs demonstrate that the power laws span a minimum of one decade.

Sample	Porosity from N ₂	BET surface area (m ² /g)	Outer cutoff (Å ⁻¹)	Inner cutoff (Å ⁻¹)	D_s	Outer cutoff (Å ⁻¹)	Inner cutoff (Å ⁻¹)	D
3K*	0.75	2850	2.0×10^{-4}	8.3×10^{-3}	2.3			
3K*-H6 (II,A)	0.80	2900	4.6×10^{-4}	7.7×10^{-3}	2.4	3.7×10^{-2}	6.2×10^{-1}	1.7
3K*-H7 (I,A)	0.74	2000	2.5×10^{-4}	4.3×10^{-3}	2.4	1.7×10^{-2}	3.6×10^{-1}	2.1

6.3.1 Non-fractal explanation

The power law behavior seen at large q in Sample 3K*-H6 (II,A) has a slope of $n = -1.7$. This means that the scattered intensity follows the relation $I(q) \propto q^{-1.7}$.⁶ We recall that scattering from a long thin rod or filament is given by the expression $I(q) \propto q^{-1}$ and that scattering from a thin platelet or surface is given by the expression $I(q) \propto q^{-2}$. A potential non-fractal explanation for this power law slope could be a power law size distribution of primary particles that are long rods or infinitesimally thin discs.

The high q power law seen in sample 3K*-H6 (II,A) has a power law slope of $n = -2.1$, implying $I(q) \propto q^{-2.1}$. This suggests a sheet-like structure with $I(q) \propto q^{-2}$. A non-fractal explanation for this power law slope could be a power law size distribution of platelets, thin disks, or slit-shaped primary scattering particles.

⁶Neither sample 3K*-H6 (II,A) or 3K*-H7 (I,A) has been classified as a mass or pore fractal yet because the physical mechanism of their formation is undetermined.

6.3.2 Fractal interpretation

The difference between samples 3K*, 3K*-H6 (II,A), and 3K*-H7 (I,A) is that 3K*-H6 (II,A) and 3K*-H7 (I,A) have been boron-doped. If we accept the explanation that the power law behavior at high q for samples 3K*-H6 (II,A) and 3K*-H7 (I,A) is due to a power law distribution of pore sizes, then our fundamental working assumption does not hold and our analysis cannot be used.⁷

If the power law distribution explanation is correct, it implies that adding 1.6 wt.% boron to Sample 3K* causes a monodisperse sample to become a very polydisperse sample. This is a reasonable conjecture; however, it doesn't provide any explanation for the increase in scattered intensity observed in the two doped samples at $q \geq 0.02 \text{ \AA}^{-1}$. As mentioned in Section 6.1.1, carbon and boron have essentially the same number of electrons. If the nanopores in Sample 3K* were simply filled with boron, the expected result would be an overall *decrease* in the scattered intensity.

Previous studies have found that 2D non-interacting clusters undergoing diffusion-limited aggregation have fractal dimension $D=1.8$ [58, 59]. These aggregation clusters resemble dendrite-like structures. Reaction-limited aggregation, under similar conditions, has a fractal dimension $D= 2.1$.

Due to the increase in intensity, in the absence of a notable change in the electron density of the sample, it is proposed that the second set of power laws observed in samples 3K*-H6 (II,A) and 3K*-H7 (I,A) are characteristic length scales of a secondary structure, not secondary length scales of a primary carbon structure. Thermal decomposition of $B_{10}H_{14}$ can result in the formation of a yellow solid residue. This is the proposed secondary structure.

The power law seen in Sample 3K*-H6 (II,A), with fractal dimension $D=1.7$ is postulated to be due to a dendritic growth of the yellow boron solid on the sample

⁷This is not meant to imply that our framework does incorporate fractal objects. It only serves to illustrate that a different analytical approach needs to be taken.

surface. In light of this interpretation, the fractal dimension $D=2.1$ of Sample 3K*-H7 (I,A) is consistent with a more regular sheet-like film on the sample surface.

The increase in scattered intensity is explained as being due to the layering of two different structures with the same electron density. The fact that sample 3K*-H7 (I,A) is almost 7 wt.% boron supports the idea that if it were distributed on the surface it would have more complete surface coverage than 3K*-H6 (II,A), which has only 1.6 wt.% boron.

The PSD of all three samples show one predominant peak corresponding to nanopores with widths $W < 10 \text{ \AA}$. The peak is located in the same position for each sample. It is largest for Sample 3K*, the parent material. The magnitude of the peak is diminished as the boron content of the sample is increased. This suggests pore clogging. Furthermore, according to the PSD data, samples 3K*-H6 (II,A) and 3K*-H7 (I,A) show an increase in features with widths $W > 20 \text{ \AA}$ in comparison to Sample 3K*.

This is interpreted as a consequence of the dendritic structures of Sample 3K*-H6 (II,A) and the thin film of Sample 3K*-H7 (I,A). The cumulative pore volume of Sample 3K*-H7 (I,A) is approximately a factor of two less than Sample 3K*, suggesting that a thin sheet of boron could be clogging pores, effectively smoothing out the surface.

Sample 3K*-H6 (II,A) on the other hand, has a larger CPV than Sample 3K*. This is consistent with the scenario that nitrogen is probing an extended surface area provided by a dendritic growth on the sample surface. In sum, it is tempting to conclude that SAXS:

1. Sees the nanopore structure of the undoped parent Sample 3K* at small length scales.
2. Sees a dendritic-like growth of a boron film on the pore surface of Sample 3K*-H6 (II,A). This results in scattering that follows a power law $I(q) \propto q^{-1.7}$. The nanopore structure of Sample 3K* is masked at $q \geq 0.02 \text{ \AA}^{-1}$ in the x-ray data

(but is still visible in the N_2 PSD). The surface fractal behavior seen in Sample $3K^*$ dominates at large length scales.

3. Sees a contiguous boron film on the pore surface of Sample $3K^*$ -H7 (I,A). This results in scattering that follows a power law $I(q) \propto q^{-2.1}$. The nanopore structure of Sample $3K^*$ is masked at $q \geq 0.02 \text{ \AA}^{-1}$. The surface fractal behavior seen in Sample $3K^*$ dominates at large length scales.

This is summarized pictorially in Figure 6.5.

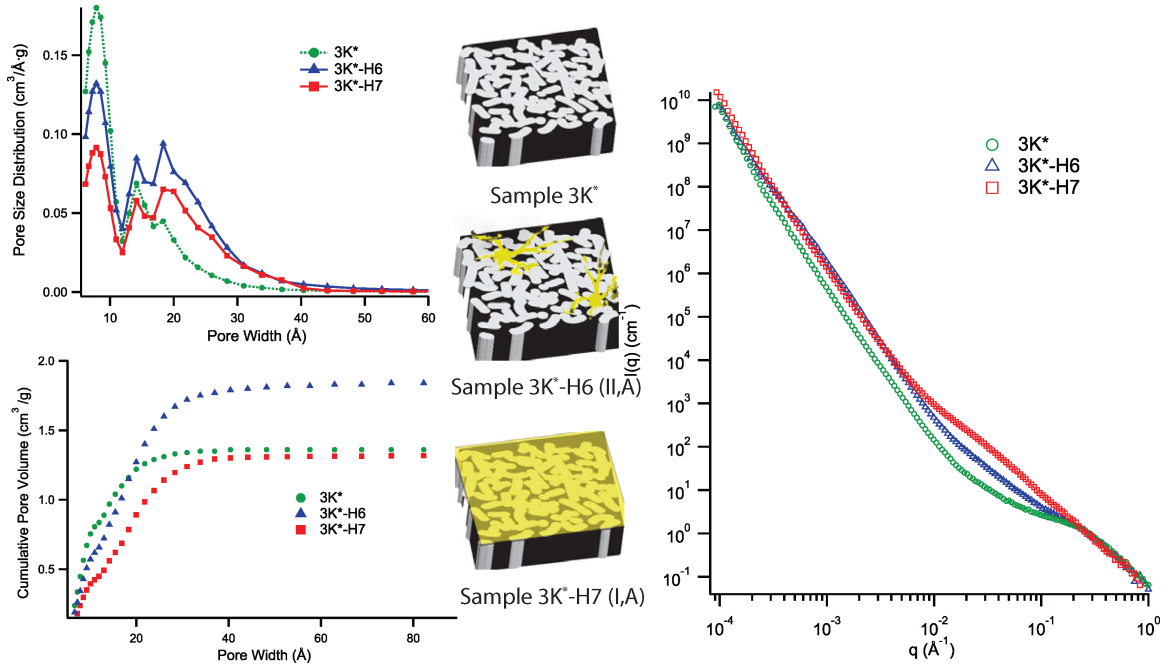


Figure 6.5: Graphical illustration of the proposed boron pore clogging scenario. The USAXS curve, CPV, and PSD of the individual samples are given along with the proposed surface topology features (resulting from pore clogging) that could give rise to power law scattering behavior seen in the boron-doped samples.

6.4 Summary and conclusion

The structure of one boron-doped sample measured before and after irradiation was investigated. No significant structural difference was measured using SAXS or nitrogen isotherms. Hydrogen isotherms, however, present a very different picture of

the sample morphology. Sample 3K-H6 (II,A) Irr. 1 min. may preliminarily be considered a case study of a sample whose structure neither SAXS, nor nitrogen can adequately probe.

The boron-doped samples 3K*-H6 (II,A) and 3K*-H7 (I,A) have scattering curves that are different in comparison to their parent sample, 3K*. The scattering curve of Sample 3K* resembles the standard curve discussed in Section 3.2. Samples 3K*-H6 (II,A) and 3K*-H7 (I,A), on the other hand, show power law scattering at large q values where the nanopore knee is typically observed.

Assuming the increased scattered intensity is due to a secondary structure, we have made an effort to explain how the two different power laws might describe surface topology resulting from pore clogging. The difference in the slope of the power laws is attributed to the amount of boron deposited on the pore surface.

Chapter 7

SAXS measurements: hydrogen and methane storage performance

7.1 Connection to ALL-CRAFT work

The ultimate goal of any characterization technique is to relate structure and function. This is where the bulk of future USAXS and SAXS work will be focused. In this chapter, some very preliminary findings are presented in which the pore dimensions measured and presented in Chapter 4 are connected to hydrogen and methane storage measurements.

The data considered in this chapter is restricted to samples 3K, 4K, and AX-21/MS-30. These three samples have complete sets of methane, nitrogen, and hydrogen isotherms. As the ALL-CRAFT project matures, full data sets measured on all instruments are becoming available. The result is a comprehensive examination of sample structure that incorporates several different characterization techniques.

To this point, the main bottle-neck has been measurement time. A pinhole SAXS scan takes 10 to 20 seconds per sample; a USAXS scan takes approximately 5 to 8 minutes per sample; a full nitrogen isotherm takes 3 to 4 days per sample; a full

hydrogen isotherm takes over a week per sample; and a full low-pressure methane isotherm is measured manually, one point at a time, and can take several weeks.

7.2 Trends between SAXS measurements and storage performance

The purpose of this section is to relate the SAXS parameters measured in Chapter 4 to hydrogen and methane storage measurements. The hydrogen measurements consist of the gravimetric excess adsorption ($G_{\text{ex,H}_2}$) (g/kg), and the gravimetric storage capacity ($G_{\text{sc,H}_2}$) (g/kg). These quantities are calculated from hydrogen adsorption isotherms measured at 303 K and 50 bar, and at 80 K and 50 bar (Table 7.1).

Methane storage measurements consist of the gravimetric excess adsorption ($G_{\text{ex,CH}_4}$) (g/kg), gravimetric storage capacity ($G_{\text{sc,CH}_4}$) (g/kg), and volumetric storage density ($V_{\text{sd,CH}_4}$) (g/l). These quantities are calculated from methane isotherms measured at 293 K and 35 bar (Table 7.2). The hydrogen and methane measurements are graciously provided by Matt Beckner and Jimmy Romanos, respectively.

Table 7.1: Hydrogen storage measurements of $G_{\text{ex,H}_2}$, and $G_{\text{sc,H}_2}$ recorded at 80 K and 50 bar, and at 303 K and 50 bar.

Sample	$G_{\text{ex,H}_2}$ (g/kg) at 80 K and 50 bar	$G_{\text{sc,H}_2}$ (g/kg) at 80 K and 50 bar	$G_{\text{ex,H}_2}$ (g/kg) at 303 K and 50 bar	$G_{\text{sc,H}_2}$ (g/kg) at 293 K and 50 bar
3K	68.6	97.5	6.6	13.7
4K	52.4		4.9	12.7
AX-21/ MSC-30	55.7	90.5	4.7	13.1

Table 7.2: Methane storage measurements of $G_{\text{ex,CH}_4}$, $G_{\text{sc,CH}_4}$, and $V_{\text{sd,CH}_4}$ recorded at 293K and 35 bar.

Sample	$G_{\text{ex,CH}_4}$ (g/kg) at 303 K and 35 bar	$G_{\text{sc,CH}_4}$ (g/kg) at 293 K and 35 bar	$V_{\text{sd,CH}_4}$ (g/l) at 303 K at 35 bar
3K	192	236	104
4K	203	256	97
AX-21/ MSC-30	188	242	92

7.2.1 Methodology

In order to relate the storage parameters to the measured pore dimensions requires looking for trends between all permutations of the SAXS data and storage measurements.

Matrix scatter plots (MSP) are a visually efficient method of preliminarily identifying trends within potentially large data sets. Figure 7.1 gives an example, for illustrative purposes only, of the type of MSP used in this chapter.

In this particular case, the rectangular box form factor fit parameters and methane storage measurements are investigated. The side lengths A , B , and the corresponding pore volume are plotted for samples 3K, 4K, and AX-21/MSC-30 on the x -axis. The values of $G_{\text{ex,CH}_4}$, $G_{\text{sc,CH}_4}$, and $V_{\text{sd,CH}_4}$ calculated from the methane isotherms are plotted on the y -axis.

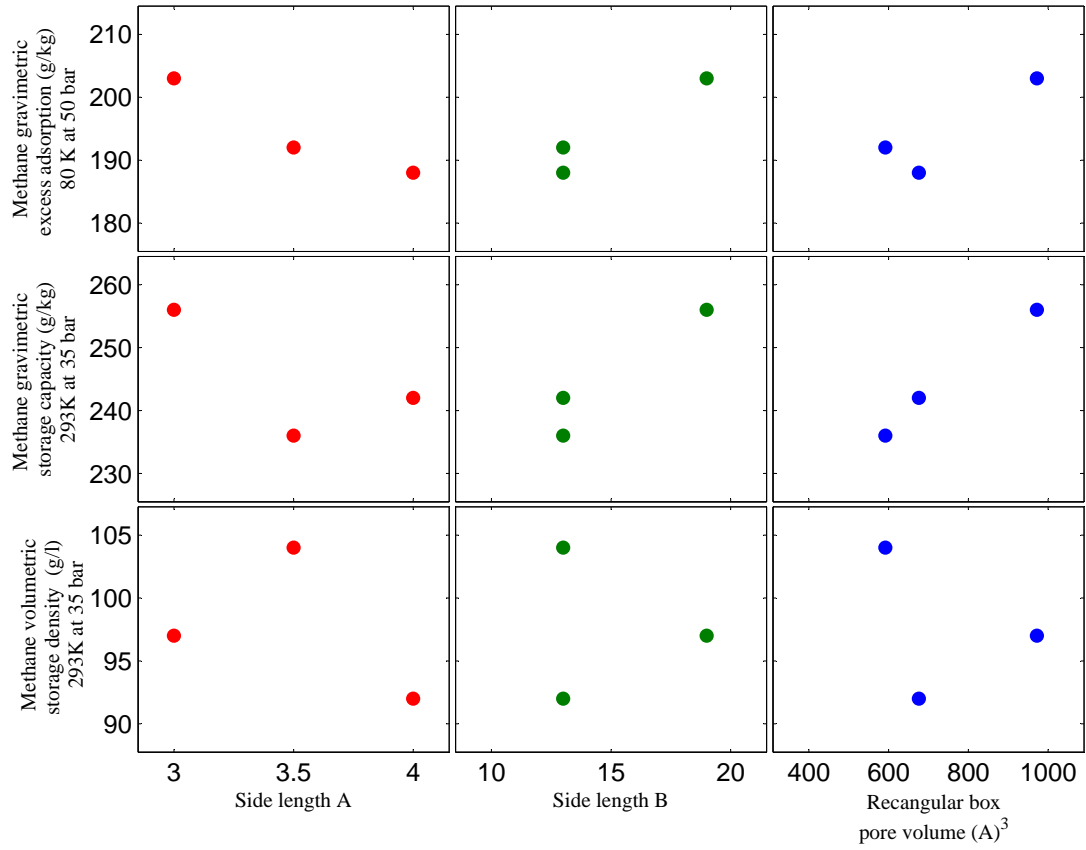


Figure 7.1: An illustrative example of a matrix scatter plot of the rectangular box fit values from SAXS plotted against the corresponding methane storage values. The plots are not color coded by sample identity, they are color coded according to the SAXS parameter measured.

Again, the goal of this plot is not to evaluate individual sample performance, but to look for trends that relate the sample structure to its storage ability. To examine all potential relations between the form factor fit results and the hydrogen and methane data requires two 3×3 and four 2×3 MSP. These are not included for brevity. Observed trends were fit using linear regression analysis, Table 7.3.

Table 7.3: Linear regression analysis for the two observable trends between storage measurements and SAXS parameters

Storage parameter	SAXS parameter	a	b	Regression coefficient
$G_{\text{sc,CH}_4}$ at 303 K and 35 bar	Cylinder pore volume	204	0.052	
	Rectangular box pore volume	210	0.047	
$G_{\text{ex,CH}_4}$ at 293 K and 35 bar	Cylinder width (W)	10	132	0.99
$G_{\text{ex,H}_2}$ at 303 K and 50 bar	Cylinder length (L)	-0.3	13	0.99

7.3 Results

Six different quantities are measured using the SAXS form factor fits from Chapter 4: nominal cylinder widths W and lengths L ; nominal rectangular box side lengths A and B ; and cylindrical and rectangular box pore volumes.

A comparison of these six quantities and the array of storage measurements listed in Section 7.2 gives three trends. These are:

1. Dependence of $G_{\text{sc,CH}_4}$ at 293 K and 35 bar on the pore volume. This is observed for the case of both cylinders and boxes.
2. Dependence of $G_{\text{ex,CH}_4}$ at 293 K and 35 bar on cylinder width.
3. Dependence of $G_{\text{ex,H}_2}$ at 303 K and 50 bar on cylinder length.

The first two of these trends are completely in line with the conventional wisdom that an increase in pore width can accommodate more adsorbate. The third trend illustrates the danger of interpreting the nominal measurements of pore dimensions too literally.

7.3.1 $G_{\text{sc,CH}_4}$ and SAXS pore volume

The pore volume is the only parameter common to both form factor fits. Although the volume calculation depends on the shape of the chosen pore model, if we assume that the two fits are reasonably comparable in merit, this quantity should show the least dependence on the specific pore model used. The cylinder pore volumes (blue) and the box pore volumes (red) are plotted against $G_{\text{sc,CH}_4}$ in Figure 7.2. Both the cylinder and box pore volumes scale linearly with the $G_{\text{sc,CH}_4}$.

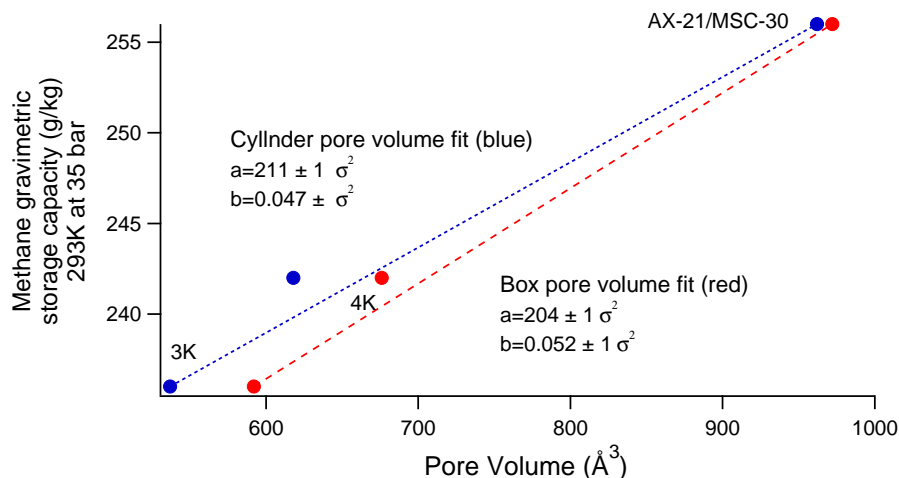


Figure 7.2: Left: Cylinder pore volumes (blue) and rectangular box pore volumes (red) vs $G_{\text{sc,CH}_4}$ capacity (g/kg) at 293 K and 35 bar. The individual samples are labeled. The measurements are made with an uncertainty of $\pm \sigma^2$, which represents one standard deviation.

Although trend lines are independently calculated based on pore shape, visual inspection demonstrates that it would be plausible to fit a global trend line to the complete set of pore volume measurements. The slopes and intercepts of the linear regressions are nearly equal. No regression coefficient is given for this fit, the data were simply fit to within one standard deviation.

A larger pore volume can obviously accommodate more methane molecules. This relationship is therefore reasonable. It is a simple statement that increased space results in increased storage. This trend is discussed a little more in terms of the

second trend (below) as extensive studies have been done that relate pore widths to gravimetric excess adsorption.

7.3.2 $G_{\text{ex,CH}_4}$ and SAXS pore width

An increase in pore width should result in an increase in storage capacity at room temperature as submonolayer coverage is proceeded by monolayer coverage, and finally by multilayer adsorption.

The molecular width of methane is ~ 3.7 Å. The cylinder widths measured from SAXS range between 5-7 Å, Figure 7.3. Above $W \approx 5$ Å, a slit-shaped pore can easily accommodate a monolayer of methane molecules.¹ The optimum slit pore size for methane delivery in carbons has been estimated to be $W = 10$ Å [60]. The measured pore widths measured here are between 5 and 10 Å. A schematic of two scenarios with different coverages, based on pore width, are sketched as an inset in Figure 7.3.

The linear trend that is observed is artificial due to the fact that, based on physical grounds, it cannot be extrapolated in either direction and therefore must have a different form. This is clear for the following reasons.

Since a methane molecule is approximately ~ 3.7 Å in diameter, below a certain length scale there will not even be submonolayer coverage as the methane molecule will be restricted from entering the pore. At larger length scales, the width of the pore cannot increasingly accommodate more and more molecules. That is, adsorption of methane on carbon is strong enough that it will quickly go to saturation.

In conclusion, although the dependence of $G_{\text{ex,CH}_4}$, and $G_{\text{sc,CH}_4}$ on pore volume and width may not be truly linear², the proposed correlation that a larger pore width

¹The ideal comparison of these results would be with cylindrically shaped pores, but this shape is not as common in the literature.

²Or may be linear only over a limited regime.

and volume result in increased gravimetric excess adsorption and gravimetric storage capacity of methane are perfectly reasonable.

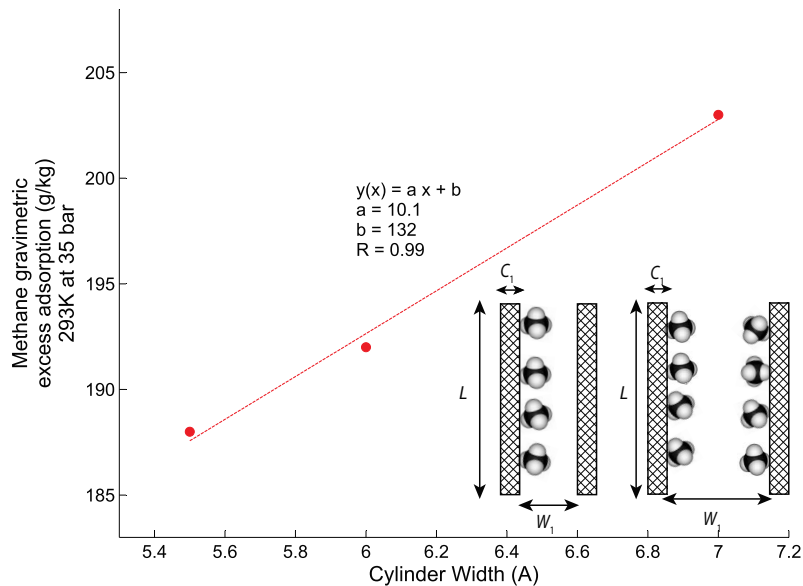


Figure 7.3: Linear dependence of methane gravimetric excess adsorption (g/kg) at 293 K and 50 bar on cylinder width. The inset (bottom right) is a sketch of how an increase in pore width could lead to increased gravimetric excess adsorption.

7.3.3 $G_{\text{ex,H}_2}$ and SAXS pore length

The inverse linear dependence of $G_{\text{ex,H}_2}$ on cylinder length makes little physical sense. It contradicts the finding of Rzepka *et. al.* [61], who state that the gravimetric excess adsorption of hydrogen at room temperature should be approximately independent of the pore size and geometry but depend on its specific surface area. If the gravimetric excess were inversely proportional to the cylinder length, this would imply that the gravimetric excess adsorption increases with decreasing specific surface area.

These results reinforce the universal discipline-independent danger of putting too much emphasis on too few measurements.

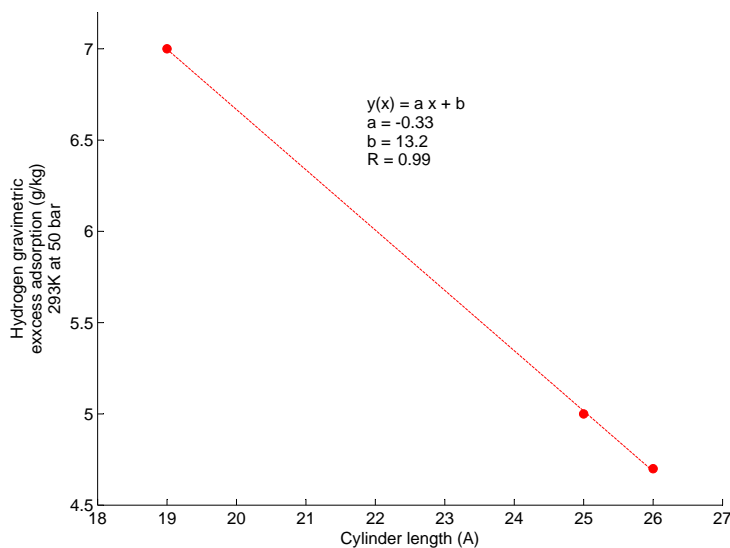


Figure 7.4: The apparent inverse linear dependence of the hydrogen gravimetric excess adsorption at 303 K and 50 bar on cylinder length.

7.4 Summary and conclusion

An attempt has been made to find simple trends between the nominal pore dimensions of samples 3K, 4K, and AX-21/MS-30 (measured using SAXS in Chapter 4), to hydrogen and methane storage measurements. Matrix scatter plots were constructed that compared the widths and lengths of cylindrical pores, the side lengths of rectangular box pores, and the corresponding pore volumes to the quantities: $G_{\text{ex,H}_2}$ and $G_{\text{sc,H}_2}$ measured at 303 K and 50 bar; $G_{\text{ex,H}_2}$ and $G_{\text{sc,H}_2}$ measured at 77 K and 50 bar; and $G_{\text{ex,CH}_4}$, $V_{\text{sd,CH}_4}$, and $G_{\text{sc,CH}_4}$, measured at 293 K and 35 bar.

A linear relationship was observed between pore volume and $G_{\text{sc,CH}_4}$, and cylinder width and $G_{\text{ex,CH}_4}$ at 293 K and 35 bar. An inverse linear relationship was found between cylinder length and $G_{\text{ex,H}_2}$ at 77 K and 50 bar. The trends involving the methane data are in agreement with conventional wisdom of how pores with widths between 5 and 11 Å influence methane adsorption. The trend between cylinder length

and $G_{\text{ex,H}_2}$ does not represent any particular physical phenomena.

Chapter 8

Effect of activation temperature on pore structure

Previous chapters have relied on the methodology developed in Chapter 3 to characterize pore shapes and sizes. Unfortunately, SAXS curves do not always offer enough information to make a quantitative assessment of pore geometry. For example, if the SAXS data cannot be scaled to units of absolute intensity then measurements of individual pore dimensions may be in error by a factor of two or more. In Section 4.6.4, it was discussed how the presence of mesopores can lead to a breakdown of the primary working assumption formulated in Chapter 3.

An incorrectly calibrated SAXS curve and/or the presence of a large volume fraction of mesopores provide two examples of cases in which a quantitative analysis of pore dimensions will give poor results. In this chapter we simultaneously deal with both of these scenarios. Our best option is to use a model-independent SAXS characterization technique to roughly estimate pore sizes.

The approach of this chapter is fundamentally different from previous chapters. SAXS and nitrogen data are used together to qualitatively interpret the change in pore structure accompanying an increase in activation temperature. PSD and CPV

data will be used in the same capacity as before, but SAXS measurements will be limited to using Guinier’s approximation for the radius of gyration, R_g (Appendix B.9). This means that our SAXS analysis will only provide one characteristic pore length instead of two.

A contrast matching pilot study is also introduced as a new method of probing pore space. The goal of the contrast matching study is to fill pores with a liquid that has a similar electron density to carbon. This reduces the difference in the mean scattering length density between the carbon and pore. A successfully filled pore will show minimal scattering. The length scale at which wetted pores demonstrate successful contrast matching gives an indirect estimate of the breadth of the pore network.

8.1 Introduction

Samples with a ratio of 3 KOH:C were activated at 700°C, 800°C, 900°C, and 1000°C.

¹ Sample 3K is ordinarily activated at 790°C. Nitrogen data of Sample 3K 790°C will be substituted for 3K 800°C, as it has not been measured on the Autosorb.

8.2 Effect of activation temperature on pore structure

Nitrogen data provides a quantitative measurement of how the cumulative pore volume and its distribution (PSD) within sample 3K change as the activation temperature is increased.

The PSD and CPV data clearly indicate that changing the activation temperature from 700°C to 1000°C increases the cumulative pore volume from 1.0 cm³/g to 2.6

¹Samples 3K 700°C, 3K 800°C, 3K 900°C, and 3K 1000°C respectively.

cm^3/g (Figure 8.1 and Table 8.1).

Sample 3K 700°C (red circles) consists almost exclusively of nanopores. The additional $1.6 \text{ cm}^3/\text{g}$ of pore volume found in Sample 3K 1000°C (grey squares) is almost exclusively distributed within the mesopore size range.

Although an increase in the fractional volume of mesopores must come at the cost of a reduction in the fractional volume available to nanopores, all samples still show intact nanopore populations. The change in the CPV with temperature (per 100°C), demonstrates that there is not a linear relationship between the CPV and the percentage of nanopores in the sample having widths less than 20 \AA .

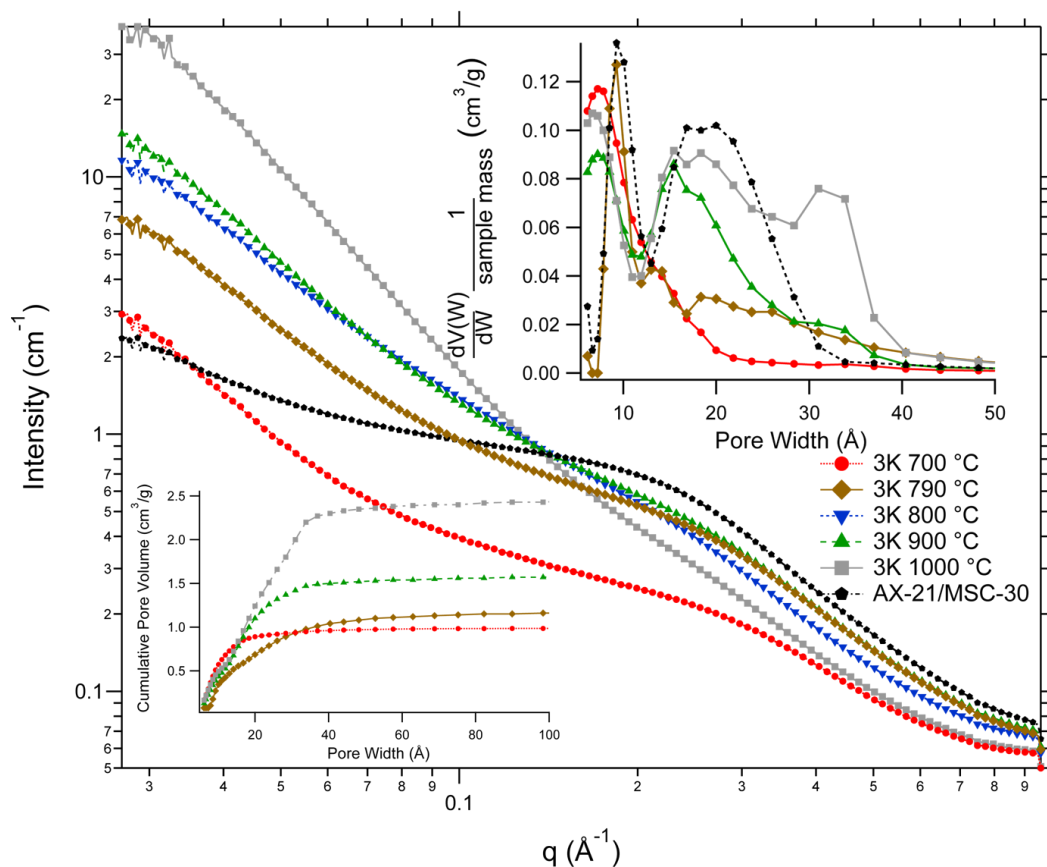


Figure 8.1: SAXS curves for samples 3K 700°C (red circle), 3K 790°C (brown diamond), 3K 800°C (blue upside-down triangle), 3K 900°C (green triangle), 3K 1000°C (gray square), and AX-21/MS-30 (black pentagon). The PSD and CPV are provided as insets.

Table 8.1: Cumulative pore volume, change in CPV per 100°C, and percentage of pores with widths $W < 20 \text{ \AA}$ for samples 3K 700°C, 3K 790°C, 3K 900°C, 3K 1000°C.

Sample	Cumulative pore volume (cm^3/g)	$\Delta \text{CPV}/\Delta 100^\circ\text{C}$	Percentage of nanopores ($W < 20 \text{ \AA}$)
3K 700°C	1.0		90
3K 790°C	1.2	0.2	60
3K 900°C	1.6	0.4	70
3K 1000°C	2.6	1	50

8.2.1 Sample 3K 700°C and AX-21/MSC-30

The PSD for sample 3K 700°C consists almost entirely of nanopores (Figure 8.2). All other samples have mesopore populations that increase in width and fractional pore volume as the temperature is increased. The contribution made by mesopores to the scattered intensity can be qualitatively illustrated by directly comparing the PSD and corresponding SAXS curves of samples 3K 700°C and AX-21/MSC-30 (The hatched area gives the difference between the two samples).

Because the only difference between the PSD of Sample AX-21/MSC-30 and Sample 3K 700°C is the presence or absence of mesopores, it can be concluded that the mesopores are responsible for the difference in scattered intensity between the two SAXS curves (Figure 8.2, left).

8.2.2 Samples 3K 800°C , 3K 900°C , 3K 1000°C : the contribution from mesopores

Section 8.2.1 provides an adequate qualitative picture of the influence that mesopores have on the magnitude of the scattered intensity. To make things somewhat more quantitative, these samples are examined in the same way as samples 5K and 6K in Section 4.6.4.

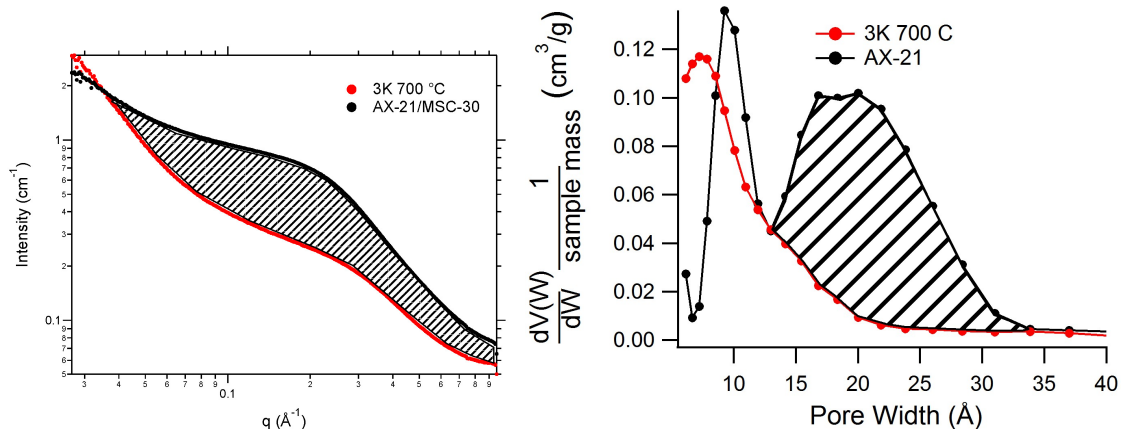


Figure 8.2: The contribution of mesopores to the scattered intensity as illustrated by samples 3K 700°C and AX-21/MSC-30. Left: SAXS curves 3K 700°C and AX-21/MSC-30. Right: PSD of 3K 700°C and AX-21/MSC-30. The hatched area of the scattering curve corresponds to the hatched area of the PSD.

In that section, it was demonstrated that non-negligible mesopore populations manifest themselves in SAXS curves by making the power law slope steeper in the Transition Region. That trend is seen here as well (Table 8.2). The only difference between the two studies is that the ratio of KOH:C was varied in one case, while the activation temperature was varied in the other.

The results demonstrate the general trend that the power law slope in the Transition Region becomes increasingly negative as the temperature increases. We point out that the slope n is steeper for Sample 3K 800°C than Sample 3K 900°C. This trend is not understood, and is also observed for the radius of gyration measurements (in the following section).

Table 8.2: Power law slopes, prefactors, and the radius of gyration fits made to the Transition Region of the SAXS curve.

Sample	Power Law slope $I(q) \propto q^n$	Prefactor	Radius of gyration (Å)
AX-21/MSC-30	$n = -0.39$	0.96	5.2
3K 700°C	$n = -0.64$	0.31	4.2
3K 790°C	$n = -0.82$	0.71	4.9
3K 800°C	$n = -1.40$	0.76	5.6
3K 900°C	$n = -1.25$	0.86	5.5
3K 1000°C	$n = -2.25$		

8.3 Model-independent SAXS analysis

8.3.1 Guinier approximation

A model-independent SAXS analysis is performed to validate the effect of activation temperature on pore structure deduced from nitrogen PSD and CPV data. The analysis is done in an effort to help quantify the assertion that increasing the activation temperature results in an increase in pore size. Because the power law slopes in the Transition Region of the SAXS curve become increasingly steep with temperature, we expect to find that the average pore size increases as well.

As explained in Appendix B.9, the Guinier approximation can be used to estimate the relative size of pores. A measurement of the radius of gyration for samples 3K 700°C through 3K 900°C does indeed show that R_G increases with activation temperature (Table 8.2).²

Sample 3K 700°C has a radius of gyration of $R_G=4.2$ Å. This is followed by 3K 900°C, and 3K 800°C. Sample 3K 900°C has an R_G that is less than Sample 3K 800°C ($R_G=6.0$ Å and $R_G=5.8$ Å, respectively). We expect Sample 3K 900°C to

²With the exception that 3K 900°C has a smaller radius of gyration than 3K 800°C.

have a larger R_G value since it was activated at a higher temperature than Sample 3K 800°C, but note that it is well within the uncertainty (which is likely around $\pm 1\text{\AA}$).³ As mentioned in Section 8.2.2, 3K 800°C had a steeper power law slope in the Transition Region than 3K 900°C. So this serves as a consistency check that an increasingly negative power law slope implies an increase in the average pore size.

In addition to the increase in R_G with activation temperature, there is a corresponding increase in the prefactor of the Guinier fit. The value of the prefactor increases from 0.31 to 0.9 for samples 3K 700°C through 3K 900°C. This is significant for the following reasons.

The Guinier approximation is a fit involving only two fit parameters R_G , and I_0 . R_G is a measurement of the relative size of a pore, whereas the prefactor $I(0)$ is a measurement of the forward scattered intensity. In Appendix B.9.1 it is shown that the forward scattered intensity is related to the volume of the scattering object by $I(0) \sim V^2 \rho^2$. Because the electron density of a sample is considered constant in the small-angle scattering regime, the only way $I(0)$ can increase is if the volume of the pore increases (c.f. Equation (B.18)). The increase of R_G and $I(0)$ with temperature, therefore, is consistent with an increase in pore size.

We point out that Sample 3K 1000°C has been left out of this discussion because it was too pathological to be fit using the Guinier approximation. The fact that the power law tail of 3K 1000°C almost spans one decade, is a strong indication of a power-law size distribution of pores or fractal behavior.

8.3.2 Conclusion

Both SAXS and nitrogen isotherm data confirm that an increase in the activation temperature from 3K 700°C to 3K 1000°C causes a change in the pore structure.

³Additionally, the prefactor of 3K 900°C is larger than that of 3K 800°C.

What begins as an almost exclusively monodisperse system of nanopores at 700°C becomes a primarily mesoporous system at 1000°C.

8.4 Contrast matching as a method to explore pore space

8.4.1 Introduction

Small-angle x-ray scattering is a technique that measures the difference in the mean scattering length density between, at least, two phases. In the two phase activated carbon system we have considered, we have pores that effectively scatter with an electron density of carbon (ρ_e) and a carbon skeleton that scatters with an effective electron density of vacuum. The difference in the electron density of the two phases is $(\Delta\rho)^2 = \rho_e^2$ (c.f. Section 3.4.3). If a contrast agent with $\rho_{\text{contrast}} \approx \rho_e$ is used, the result will be $(\Delta\rho)^2 = 0$. The intensity will be zero when the electron density of the two phases are equal. The corollary to this statement, is that an intensity of zero indicates a successfully filled pore.

8.4.2 Previous SAXS contrast matching work

Contrast matching is a technique more commonly employed in SANS studies than in SAXS studies. Nevertheless, it has been used in a few SAXS studies of carbon materials. Laszlo *et. al.* have used contrast matching to estimate how the surface chemistry of activated carbon affects the pore-filling ability of different solvents as a function of their polarity [42, 62].

Recently, a series of detailed contrast matching studies involving cylindrically-shaped pores were performed that evaluated the contributions made by ordered versus disordered pores to the scattered intensity [63, 64]. Unfortunately, the results of

these studies can not be easily applied here, as the authors investigated a highly controlled, ordered, mesoscopic silica sample. Their choice of contrast agent was dibromomethane.⁴

In a DOE report about NMR techniques used for the structural analysis of coal, Smith [65] concluded that liquid halogenated hydrocarbons, and dibromomethane (CH_2Br_2) in particular, are the best contrast matching agents for carbon and silica materials.⁵

Dibromomethane

A successful contrast matching agent must have approximately the same electron density in the bulk liquid state as carbon in the solid state. As per Smith's recommendation [65], the solvent we use is dibromomethane (DBM).

Dibromomethane has a density of 2.5 g/cm^3 and a scattering contrast of $\Delta((d\Omega/d\sigma)_e \rho)^2 = 362 \times 10^{20} \text{ cm}^{-4}$. Activated carbon on the other hand, has a skeletal density of $\rho_{\text{skeleton}} = 2.0 \text{ g/cm}^3$ and scattering contrast of $((d\Omega/d\sigma)_e \rho)^2 = 287 \times 10^{20} \text{ cm}^{-4}$. The difference in contrast between DBM and carbon is $((d\Omega/d\sigma)_e \rho)^2 = 4.3 \times 10^{20} \text{ cm}^{-4}$. Although this is not a perfect match, it has been noted that complete contrast matching is not a requirement to investigate pore-filling [62].

There are two other properties that make DBM a desirable contrast matching agent. First, it has an incredibly large mass absorption coefficient $\mu_{\text{CH}_2\text{Br}_2} = 83.3 \text{ cm}^2/\text{g}$, in comparison to carbon, $\mu_{\text{carbon}} = 4.2 \text{ cm}^2/\text{g}$. This ensures that the presence of DBM on or inside of a pore will eliminate any sign of the primary beam. Second, it has a saturation vapor pressure of 40 torr (5.3 KPa) at room temperature and ambient pressure. This means that it will evaporate quickly, adsorbing rapidly onto our carbon adsorbent. In other words, the relatively high vapor pressure at ambient

⁴Hoinkis [46] mentions several SANS studies of carbon involving adsorption and pore filling using C_6H_6 if more direction is needed.

⁵The study contained results from SAS experiments as well.

temperature and pressure facilitates vapor adsorption.

8.4.3 Contrast matching examination of the effect of activation temperature on Sample 3K

To simplify the analysis we assume that the vapor from DBM completely replaces the vacuum phase in our sample. No interface profiles, partial wetting, or condensation phenomena are considered.

The samples investigated in section 8.2 are each wetted with 10 μL of DBM. The sample is given at least ten minutes to stabilize (see Appendix C.5.1 for methodology details).

Results

The results are plotted in Figure 8.3, where the wetted samples are plotted using open symbols and the dry samples are plotted using closed symbols. The dry and wetted counterpart of each sample are plotted using the same color and symbol.

We begin our preliminary interpretation of the results by examining Sample AX-21/MS-30. This sample shows a very different wetting behavior than any of the 3K samples.

Wetting behavior of AX-21/MS-30

Wetted Sample AX-21/MS-30 shows an increase in the scattered intensity for $q \leq 0.1 \text{ \AA}^{-1}$ and $q \geq 0.6 \text{ \AA}^{-1}$. This means that features between approximately 65 \AA and 10 \AA are successfully filled with DBM.

The greater intensity of the wetted sample in comparison to the dry sample at length scales less than 65 \AA can be explained (see Section 8.4.4 below for the explanation using the results from Sample 3K). The reason for the increase in scattered

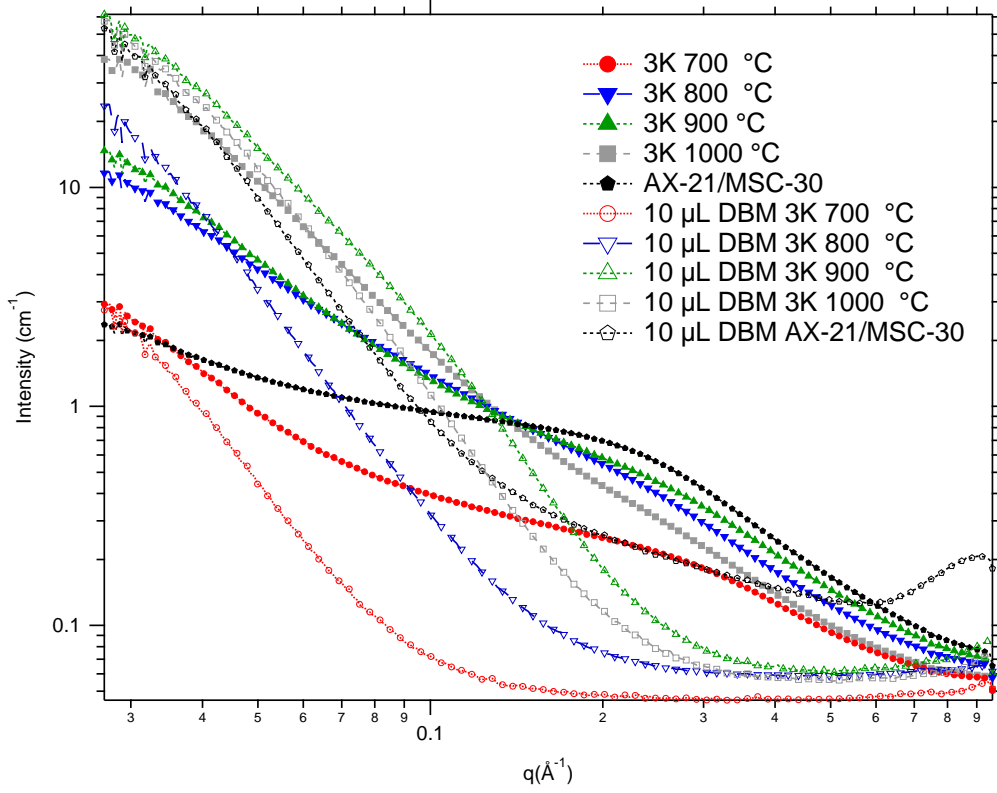


Figure 8.3: SAXS curves of dry and dibromomethane wetted samples of 3K produced at different activation temperatures, and Sample AX-21/MSC-30. Dry samples are plotted using closed markers and wetted samples are plotted using open markers. Each dry sample and its wetted counterpart have the same color and symbol.

intensity at length scales that are less than 10 Å for Sample AX-21/MSC-30, however, is more puzzling.

One possible explanation for the difference in wetting behavior is that samples AX-21/MSC-30 and 3K have different levels of surface roughness at the nanometer size scale. From TEM micrographs and the long horizontal plateau seen in the SAXS curve of AX-21/MSC-30, this sample appears to have a very smooth surface between 20 Å and 60 Å. Sample 3K on the other hand, seems to have a rougher surface at these length scales. This is an item for future investigation.

Wetting behavior of Sample 3K

From Figure 8.3 it is clear that all of the 3K samples show virtually no scattering at large q values ($q > 0.2 \text{ \AA}^{-1}$). This indicates that features less than 30 \AA have been successfully filled with DBM. There is no mechanism other than contrast matching that can account for the drop in intensity observed between the dry and wetted samples.

For the case of samples 3K 700°C and 3K 800°C the intensity of the wetted sample is always less than that of the dry sample. This means that features less than approximately 200 \AA have made some contact with DBM. On the other hand, for samples 3K 900°C and 3K 1000°C, the scattered intensity of the wetted sample is less than the dry sample only at large q values ($q > 0.2 \text{ \AA}^{-1}$). At smaller q values, the intensity of the wetted sample is actually greater than the dry sample.

8.4.4 Explanation: percolation threshold

The current interpretation for this behavior is that carbon-carbon links are progressively destroyed with an increase in temperature. This destruction is more or less complete at 1000°C. Intermediate regions, above 800°C may have complex structures of both percolating pore and carbon skeleton. At low levels of pore destruction (e.g. 3K 700°C) nanopores exist within an intact carbon matrix. Wetting the intact pores with DBM causes them to fill and the intensity is reduced due to the contrast matching mechanism. This implies that for 3K 700°C the grain size is at least on the order of 200 \AA , as the entire wetted region show evidence of contrast matching.

At higher levels of pore destruction (i.e. 3K 900°C and 3K 1000°C), there is likely little carbon matrix left to host nanopore networks. There are only very fine flakey particles that are coated with DBM. These non-uniform flakes may also contain pores.

At large q values, the pores within the flakes are filled with DBM and contrast matching causes the signal to disappear. However, at smaller q values, the particles appear to the beam as very small grains coated with DBM. The DBM coating effectively increases the electron density of the particles, enhancing the contrast, and causing the wetted samples to have a greater intensity than the dry samples. This implies that the grain size for these samples is less than approximately 35 \AA (as the intensity goes to zero at $q \approx 0.2 \text{ \AA}^{-1}$ for these samples).

A very crude illustration of this scenario is given in Figure 8.4. In this illustration, the drawings in the top row represents the perspective normal to the surface (overhead view) of pores with $W \approx 6 \text{ \AA}$ (circles) in a block of solid (square). The middle row of the drawings gives a cross-sectional profile of the wetted carbon. The bottom row has sketches of the proposed scattering curves for the scenario of a low level of pore destruction (left) and a high level of pore destruction (right), as well as representative sketch of the corresponding dry sample. The diamond stripe fill indicates a carbon surface wetted by DBM. The forward diagonal stripe fill indicates carbon (it is only visible in the profile view). The backwards diagonal stripe fill indicates the DBM wetting phase (fluid or vapor).

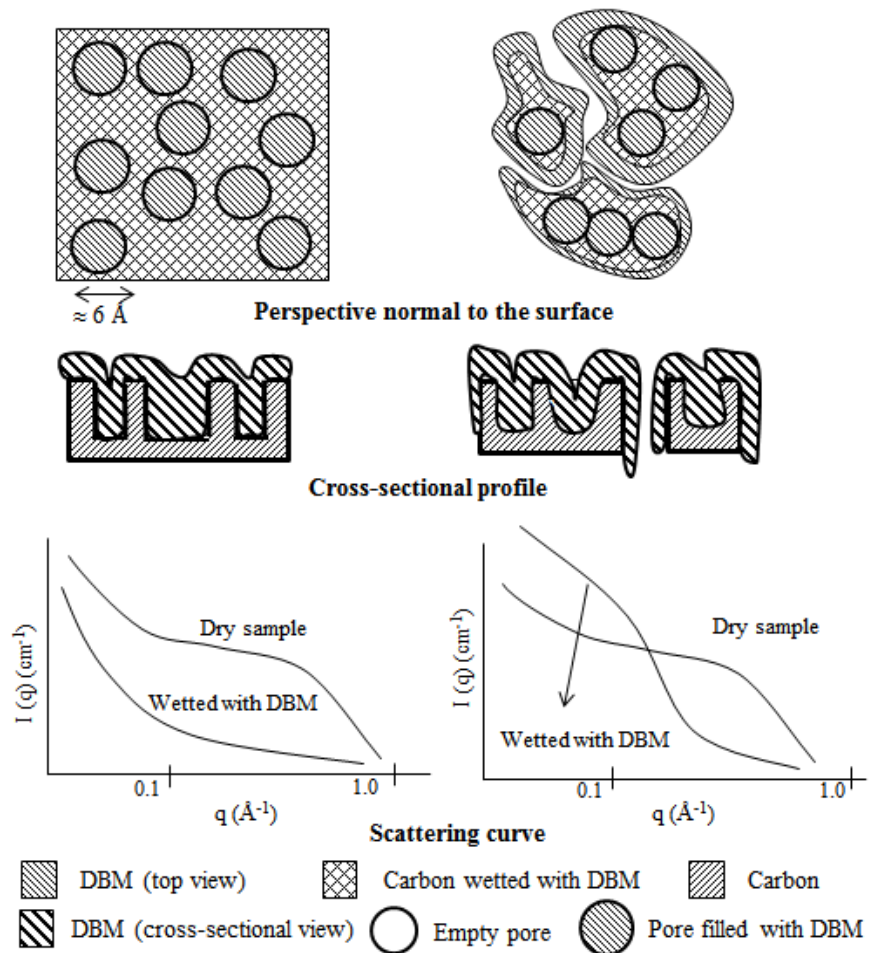


Figure 8.4: Conceptual schematic of DBM wetting the carbon pores. The case on the left represents pores within an intact carbon matrix (e.g. 3K 700°C). The case on the right corresponds to a system in which the carbon has been broken into small flakes coated with DBM containing pores that are additionally filled with DBM (this scenario corresponds to high levels of sample destruction, e.g. 3K 1000°C).

8.5 Summary and conclusion

Pinhole SAXS, nitrogen isotherm data, and contrast matching studies have been used to jointly piece together a coherent story about the structural changes that result when the activation temperature of Sample 3K is increased from 700°C to 1000°C.

All three experiments suggest that as the temperature is increased the average pore size increases, or larger pores sizes are additionally introduced into the sample.

Although there are indications that nanopores are still present in the sample, the actual pore networks have likely become disconnected. Progressive destruction of walls that separate individual pores have collapsed forming large voids consistent with mesopores.

The complete pore filling seen in samples 3K 700°C and 3K 800°C, but not in 3K 900°C or 3K 1000°C, implies that the ability of the wetting fluid to permeate and fill the entire pore network has been diminished. At very high levels of pore destruction, the dibromomethane doesn't just fill pores, but coats them. It is proposed that this is a result of the fact that at lower levels of pore destruction (e.g. 3K 700°C) the average grain sizes are larger

Sample AX-21/MS-30 shows a very different behavior when wetted with DBM in comparison with any 3K sample. The wetted sample has a greater intensity than the dry sample at both small and large q . This suggests that AX-21/MS-30:

1. has very different wetting properties compared to Sample 3K at the length scales probed by pinhole SAXS,
2. has a different structure at large q than Sample 3K, as proposed in Section 4.6.3,
3. or both.

Having complete data sets from all of the characterization techniques available to the lab will answer these questions and hopefully raise new and exciting ones in the near future.

Chapter 9

Summary and concluding remarks

A procedure combining two different particle characterization techniques has been presented that allows the measurement of at least two characteristic lengths of the fundamental building block of a nanoporous material.

Samples 3K and 4K, presented in Chapter 3, show that given the proper conditions this procedure is capable of measuring up to three representative lengths of a nanoporous solid in addition to its porosity. In those particular cases, the three lengths corresponded to a nominal pore width, length, and the width of the carbon phase surrounding the pore. We are very fortunate to have TEM micrographs that corroborate our results for Sample 3K.

The goal of this study was to develop a methodology which extracted structural information from USAXS scattering data that exceeded the distribution of pore widths provided by adsorption-desorption isotherm experiments. Although not explicitly stated, it was equally important to demonstrate that there is sufficient information in the content of a SAXS curve to extract structural details that extend beyond R_G as well.

The achievement of obtaining similar results using two different measurement techniques is a rarity, often overlooked. The level of agreement we have obtained

between the particle form factor and correlation function analysis applied to our nanoporous carbons, especially for samples 3K and 4K, is quite remarkable.

The successful application of our procedure has been demonstrated through case studies distributed over several chapters. Having mapped the structure of pores in KOH activated carbons, polymeric carbons, boron-doped carbons, and even one irradiated boron-doped sample, we claim that we have achieved our goal.

The next step in the chain of development is to link the structural characteristics of samples found using the methods developed in this study to methane and hydrogen storage measurements. The lack of detail in Chapter 7 demonstrates just how much progress remains to be made in this area. Our quick retreat to the safety of the radius of gyration measurement used in Chapter 8 demonstrates why it is used ubiquitously, it works. Our analysis is far from achieving a similar level of robustness.

Our heavy reliance on nitrogen data in Chapter 8 illustrates by way of example, that even for the cases in which we cannot use the analysis method that we have developed, a simple combination of SAXS and adsorption data can provide a very coherent narrative of sample structure, no matter how complicated it may be. It is difficult to think of a more complicated solid material to characterize than an amorphous nanoporous media near a critical point.

Hopefully this study provides affirmation that the structure of very complicated materials can be explained remarkably well using very simple models.

Appendix A

ALL-CRAFT

The Alliance for Collaborative Research in Alternative Fuel Technology (ALL-CRAFT) is a partnership of the University of Missouri-Columbia (MU, lead institution), the Midwest Research Institute (MRI) in Kansas City, and other partners to develop low-pressure, high-capacity storage technologies for natural gas (NG, methane) and hydrogen as alternative fuels for advanced transportation [66]. Its specific goal is to fabricate high surface area, multiply surface-functionalized nanoporous carbon from corncob and other precursors that optimize gravimetric and volumetric storage capacities of hydrogen and methane via reversible physisorption [57, 67].

Initial success was achieved when monolithic nanoporous carbon was produced from corncob with a storage capacity of 117 g CH₄/liter carbon and 235 g CH₄/kg carbon at 34 bar and 300 K [67] [68]. As the scope of research broadened to hydrogen storage, chemically activated powdered granular carbons were produced using potassium hydroxide (KOH) as an activating agent. The use of an activating agent causes an increase in the spacing between pores and a broadening of the distribution of pore sizes within the material. This leads to an increase in the surface area of the sample. An increase in surface area paves the way for increased storage capacity.

Samples produced with ratios of 3 and 4 KOH:C, named Sample 3K and Sample

4K respectively, demonstrated record storage capacities for activated carbons. Sample 3K yielded gravimetric excess adsorption measurements of 7 wt.% and a gravimetric storage capacity of 9 wt.% at 50 bar. Sample 4K yielded gravimetric excess adsorption measurements of 7 wt.% and storage of 11 wt.% .

Despite this success, numerical calculations and simulations predicted that the use of pure carbon would fall short of the Department of Energy’s (DOE) 2015 target for on-board hydrogen storage for light-duty vehicles.¹ It was demonstrated that the total amount of hydrogen adsorbed for pure carbons at a pressure of 100 bar could not exceed 2 wt.% at room temperature and 10 wt.% at 77 K [21, 49].

The primary obstacle to higher storage values is the low energy of adsorption of activated carbons, (4-8 kJ/mol). Higher binding energies require chemical modifications of the carbon matrix. It has been suggested that boron could be incorporated into the graphene skeleton (boron-doping), increasing the strength of the hydrogen interaction with the carbon, and increasing the energy of adsorption to more than 10-15 kJ/mol [49, 57]. In an attempt to realize this prediction, boron-doped carbons were manufactured at the laboratory scale. ALL-CRAFT is currently working towards the goal of fabricating boron-doped carbons with controlled nanopores and storage capacities in excess of 60g H₂/kg carbon at a target pressure of 34 bar and temperature of 300 K.

¹The 2015 DOE target storage parameters are 60 g H₂/kg carbon (5.7 wt.%) and 45 g H₂/liter carbon at 50 bar and 300 K on monoliths.

Appendix B

Terminology and definitions

B.1 Scattering refresher

The following adopts the notation of Pfeifer [69].

A monochromatic beam of x-rays with an incident wave vector \vec{q}_{in} is scattered by a sample through a scattering angle, θ . The scattered wave has a wave vector \vec{q}_{out} . To meet the condition of elastic scattering requires $|\vec{q}_{\text{in}}| = |\vec{q}_{\text{out}}|$. The length q of the scattered wave is given by $|\vec{q}| = |\vec{q}_{\text{out}} - \vec{q}_{\text{in}}| = 4\pi/\lambda \sin(\theta/2)$, where λ = wavelength (Å).

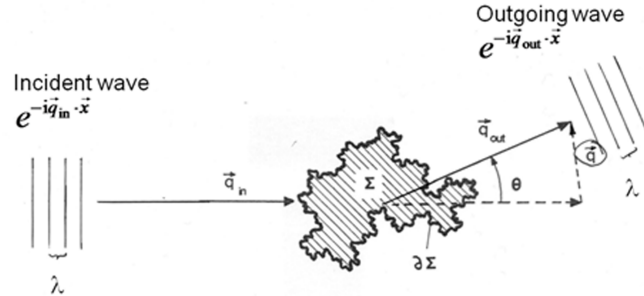


Figure B.1: An incident monochromatic plane wave of x-rays with scattering vector \vec{q}_{in} scatters off a sample through a scattering angle, θ . The outgoing wave has a wave vector \vec{q}_{out} . The scattered wave has length $|\vec{q}| = |\vec{q}_{\text{out}} - \vec{q}_{\text{in}}|$. From [69].

The scattered intensity $I(q)$ is measured as a function of the length q of the scattered wave vector.

B.2 Differential scattering cross-section

The measure of experimental intensity recorded by SAXS and USAXS instruments is the differential scattering cross-section per unit volume (cm^{-1}). This is also referred to as the absolute intensity or absolute scattered intensity, and is written $d\Sigma/d\Omega$.

The general relation between the differential scattering cross-section $d\sigma/d\Omega$ (cm^2) and the differential scattering cross-section per unit volume is given by

$$\left(\frac{d\sigma}{d\Omega}\right) = \frac{N_{\text{solid particles}}}{V_{\text{sample}}} \left(\frac{d\Sigma}{d\Omega}\right), \quad (\text{B.1})$$

where $N_{\text{solid particles}}$ is the number of solid particles in the sample volume (V_{sample}) illuminated by the beam.

B.3 Absolute scattered intensity from monodisperse solid particles

The differential scattering cross-section per unit volume measures the product of two physically significant terms: the particle form factor $P(q)$, and the particle structure factor $S(q)$.

The particle form factor $P(q)$ gives the contribution to the scattered intensity that is due to particle shape. The structure factor $S(q)$ gives the contribution to the scattered intensity that is due to the position and spatial arrangement of particles. These two terms will be discussed in more detail in Appendices B.5 and B.6. They are now worked into the expression for the scattered intensity.

Restricting ourselves to the case of a monodisperse sample consisting of one size and shape of particle, the absolute intensity of the sample is

$$I(q) = \left(\frac{d\Sigma}{d\Omega} \right)_{\text{sample}} = \left(\frac{d\sigma}{d\Omega} \right)_e (\Delta\rho)^2 \frac{N_{\text{solid particles}}}{V_{\text{particle}}} (V_{\text{single solid particle}})^2 P(q) S(q), \quad (\text{B.2})$$

where $V_{\text{single solid particle}}$ is the volume of a single solid particle and $(d\Sigma/d\Omega)_e$ is the differential scattering cross section of the electron.

The differential scattering cross-section of the electron can be written in terms of more elementary units

$$\left(\frac{d\sigma}{d\Omega} \right)_e = r_0^2 \overbrace{\frac{1 + \cos^2 \theta}{2}}^P,$$

where P is the polarization ($P \approx 1$ in the vertical scattering plane of a synchrotron source), and r_0 is the classical electron radius $r_0 = e^2/m_e c^2$, where e is the electron charge (2.81×10^{-13} cm), m_e is the mass of the electron (9.11×10^{-28} g), and $c = 3 \times 10^{10}$ cm/s.

The term $\Delta\rho = (\rho_{\text{solid particle}} - \rho_{\text{solvent}})$ is the difference in the mean electron density of the solid particles ($\rho_{\text{solid particle}}$) and solvent (ρ_{solvent}) in which it is immersed. The term $(d\Sigma/d\Omega)_e (\rho_{\text{solid particle}} - \rho_{\text{solvent}})^2$ is the difference in the mean scattering length density of the solid particle and solvent.

If the particles are in vacuum or air, the term $\rho_{\text{solvent}} = 0$. This causes a simplification as now $\Delta\rho = \rho_{\text{solid particle}}$ and consequently $(\Delta\rho)^2 = (\Delta\rho_{\text{solid particle}})^2$.

B.4 Particle form factor

From Equation (B.2) we note that $I(q) \propto S(q)P(q)$. In the very dilute limit, there is no interaction among particles, therefore $S(q) \approx 1$. Additionally, at large q values

where the dimensions of individual particles can be resolved, $S(q) \rightarrow 1$. This implies that $P(q)$ is the dominant term in Equation (B.2) for large scattering angles.

B.4.1 Form factor recipe

The prescription for finding the form factor of a particle of arbitrary shape is as follows:

1. Evaluating the Fourier transform of unity, or an indicator function, in the coordinate system most suited to the shape considered. This gives $F(\vec{q})$.
2. Squaring it, $|F(\vec{q})|^2 = |F(\vec{q}) \star F(\vec{q})|$.
3. Orientationally averaging the result, $P(q) = \langle |F(\vec{q})|^2 \rangle$.

$P(q)$ is normalized to the volume of the particle so that $P(q) \rightarrow 1$ as $q \rightarrow 0$. The calculation of $F(\vec{q})$ is done according to

$$F(\vec{q}) = \frac{1}{V_{\text{particle}}} \int e^{i\vec{q} \cdot \vec{r}} d\vec{r}, \quad (\text{B.3})$$

where V_{particle} is the volume of the shape considered. The form factor $P(q)$ is defined as

$$P(q) = \langle |F(\vec{q})|^2 \rangle. \quad (\text{B.4})$$

In small angle scattering the form factor is always orientationally averaged. For spherically symmetric particles this makes no difference in their calculation as $\langle e^{i\vec{q} \cdot \vec{r}} \rangle = \langle e^{-i\vec{q} \cdot \vec{r}} \rangle = \frac{\sin(qr)}{qr}$ in Equation (B.3). Put somewhat differently, for spherically symmetric objects $\langle |F(\vec{q})|^2 \rangle = \langle |F(\vec{q})|^2 \rangle$. Objects that do not have spherical symmetry do not simplify this nicely and as a result, are much more complicated. A large majority of form factors need to be handled numerically due to this detail.

B.4.2 Terminology note

The letters $P(q)$, and $F(\vec{q})$ have been chosen explicitly to denote the particle form factor and its amplitude respectively. Analogously, the scattered intensity is denoted by the letter $I(q)$ and its corresponding amplitude is written $A(\vec{q})$. The amplitude of the scattered intensity is the convolution of the amplitude of the particle form factor with the electron density.

$$A(\vec{q}) = \rho \star F(\vec{q}), \quad (\text{B.5})$$

giving

$$I(q) = |A(\vec{q})A(\vec{q})^*| \quad (\text{B.6})$$

The electron density for the region of interest in small angle scattering is considered constant, therefore the intensity is simply expressed as

$$I(q) = \rho^2 |F(\vec{q})|^2.$$

Many different sources use different notations for the structure factor, form factor, etc. The main purpose of this section is to point out that that $P(q)$, $F(\vec{q})$, $I(q)$, and $A(\vec{q})$ are all different quantities. More succinctly, $F(\vec{q}) \neq A(\vec{q})$.

B.5 Form factors of interest

B.5.1 Sphere

Example calculation

The calculation of the form factor of a sphere is given by first finding the amplitude of the averaged $\langle F(\vec{q}) \rangle$ and then squaring the results. The order of operations can be performed this way, because for spherically symmetric particles $\langle |F(\vec{q})|^2 \rangle = \langle |F(\vec{q})| \rangle^2$.

The result is

$$\begin{aligned}
\langle F(\vec{q}) \rangle &= \left\langle \frac{1}{V_{\text{particle}}} \int_0^{2\pi} \int_0^\pi \int_0^R e^{-i\vec{q} \cdot \vec{r}} r^2 \sin \theta dr d\theta d\phi \right\rangle \\
&= \frac{4\pi}{V_{\text{particle}}} \int_0^R r^2 \frac{\sin(qr)}{qr} dr = \frac{4\pi}{q V_{\text{particle}}} \int_0^R r \frac{\sin(qr)}{qr} dr \\
&\stackrel{V_{\text{particle}}=4/3\pi R^3}{=} \frac{4}{3} \pi R^3 \frac{3(\sin(qR) - qR \cos(qR))}{(qR)^3}
\end{aligned}$$

According to Equation(B.4)

$$P(q)_{\text{sphere}} = \langle |F(\vec{q})|^2 \rangle = \langle |F(\vec{q})| \rangle^2 = \left(\frac{3(\sin qR - qR \cos qR)}{(qR)^3} \right)^2. \quad (\text{B.7})$$

Again the equality $\langle |F(\vec{q})|^2 \rangle = \langle |F(\vec{q})| \rangle^2$ holds only for spherically symmetric particles.

B.5.2 Cylinder

For the case of a cylinder of width W and length L :

$$P(q)_{\text{cylinder}} = \int_0^{\frac{\pi}{2}} \left[\frac{2J_1(q \frac{W}{2} \sin \theta) \sin(q \frac{L}{2} \cos \theta)}{q \frac{L}{2} \cos \theta q \frac{W}{2} \sin \theta} \right]^2 \sin \theta d\theta \quad (\text{B.8})$$

B.5.3 Rectangular box

For the rectangular box, orientational averages have to be taken over the side lengths A , B , and C . The form factor can be decomposed into components perpendicular and parallel to the scattered beam, q_\perp and q_\parallel , respectively. The form factor is given by

$$P(q) = \frac{2}{\pi} \int_0^{\frac{\pi}{2}} \int_0^{\frac{\pi}{2}} q_\perp \cdot q_\parallel \sin \theta d\theta d\phi \quad (\text{B.9})$$

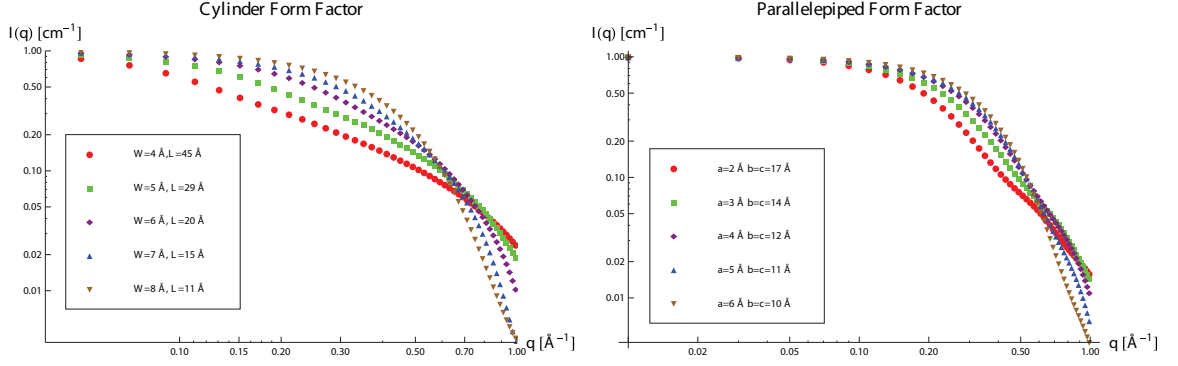


Figure B.2: The volume of the scatterer is fixed at 565 \AA^3 for each plot. Left: Plot of the form factor of a cylinder for varying widths and lengths. Right: Rectangular box for varying side lengths A and $B = C$.

The contributions given by the two components are

$$q_{\perp} = \left[\frac{\sin(q \frac{C}{2} \cos \theta)}{q \frac{C}{2}} \right]^2,$$

and

$$q_{\parallel} = \left[\frac{\sin(q \frac{A}{2} \sin \phi) \sin(q \frac{B}{2} \cos \phi)}{q \frac{A}{2} \sin \phi q \frac{B}{2} \cos \phi} \right]^2.$$

The complete form factor is

$$P(q) = \frac{2}{\pi} \int_0^{\frac{\pi}{2}} \int_0^{\frac{\pi}{2}} \left[\frac{\sin(q \frac{A}{2} \sin \phi) \sin(q \frac{B}{2} \cos \phi)}{q \frac{A}{2} \sin \phi q \frac{B}{2} \cos \phi} \right]^2 \cdot \left[\frac{\sin(q \frac{C}{2} \cos \theta)}{q \frac{C}{2}} \right]^2 \sin \theta d\theta d\phi. \quad (\text{B.10})$$

Integrating Equation (B.10) gives the average over all orientations. If the step of orientational averaging was not required, we would have the much simpler result

$$P(q) = \left[\left(\frac{2 \sin(\frac{qA}{2})}{qA} \right) \left(\frac{2 \sin(\frac{qB}{2})}{qB} \right) \left(\frac{2 \sin(\frac{qC}{2})}{qC} \right) \right]^2$$

A plot of the cylinder and rectangular box for a fixed scatterer volume of 565 \AA^3 is given in Figure B.2.

B.5.4 Cylindrical core shell model

A model for the scattered intensity of a cylinder core-shell model consisting of two concentric cylinders is given in terms of the notation of Method II and the master formula as

$$I_{\text{cs}}(q, W_1, W_1 + C_1, L) = \int_0^{\frac{\pi}{2}} \left(\frac{d\sigma}{d\Omega} \right)_e \phi \left[(\rho_{\text{core}} - \rho_{\text{shell}}) \left(\frac{\pi W_1}{2} \right)^2 L \left[\frac{2J_1(q \frac{W_1}{2} \sin \theta) \cdot \sin(q \frac{L}{2} \cos \theta)}{q \frac{L}{2} \cos \theta \cdot q \frac{W_1}{2} \sin \theta} \right]^2 + (\rho_{\text{shell}} - \rho_{\text{solvent}}) \left(\frac{\pi(W_1 + C_1)}{2} \right)^2 L \left[\frac{2J_1(\frac{W_1 + C_1}{2} \sin \theta) \cdot \sin(q \frac{L}{2} \cos \theta)}{q \frac{L}{2} \cos \theta \cdot q \frac{W_1 + C_1}{2} \sin \theta} \right]^2 \right] \sin \theta d\theta$$

There is no term $(1 - \phi)$ in this expression. This form factor explicitly takes into account interference of the core and shell through the cross-terms that are absent in Equation (3.4).

B.6 Structure factor

At very small angles, $P(q) \rightarrow 1$ as $q \rightarrow 0$. The structure factor $S(q)$, becomes the dominant term in Equation (B.2). Inter-particle interferences and interactions are probed at this length scale. The scattering angle is too small to resolve the features of individual particles, unless they happen to be very large.

At middle q , both $S(q)$ and $P(q)$ contribute to the scattered intensity. Therefore, inter-particle interferences cause a reduction in the scattered intensity.

B.6.1 Integral form

The structure factor is used quite often in colloidal, macromolecular studies, and studies of the liquid state [70, 71]. Many different notations are used. We adopt the

notation used by Hoinkis [46] since it is fairly representative of the literature. The structure factor is defined as

$$S(\vec{q}) \equiv \frac{|\int \rho(\vec{r}) \exp(-i\vec{q} \cdot \vec{r}) d^3r|^2}{\int \rho(\vec{r}) d^3r}.$$

An integral form of this equation, referred to as the Zernicke-Prins form, is

$$S(q) = 1 + \frac{N_{\text{solid particles}}}{V_{\text{sample}}} \int (g(r) - 1) e^{-i\vec{q} \cdot \vec{r}} d^3r,^{1,2}$$

where $g(r)$ is the pair correlation function.

The structure factor is almost exclusively defined numerically, as there are relatively few analytic forms [72]. Some algorithms and minimization techniques have been introduced to numerically determine the particle form and structure factors simultaneously from the scattered intensity [73].

Methods for including structure factor contributions to the differential scattering cross-section per unit volume include the monodisperse approach, decoupling approximation, local monodisperse approximation, partial structure factors, and scaling approximations. These are discussed in detail in the manual of the SASfit program [74] available at <http://kur.web.psi.ch/sans1/SANSSoft/sasfit.html>.

B.7 Master formula derivation

To keep the notation consistent with Chapters 3 and 4, the particulate carbon surrounding a pore is given the label *solid particle*. The pore is labeled *pore*. Taking into account both the population of carbon and pore, the differential scattering cross-section per unit volume of the sample can be written following Equation (B.2) as

¹This form assumes the sample is isotropic $|\vec{r}| = r$.

²The choice of $N_{\text{solid particles}}$ is arbitrary the expression could also be written in terms of N_{pores} .

$$\left(\frac{d\Sigma}{d\Omega}\right)_{\text{sample}} = \left(\frac{d\sigma}{d\Omega}\right)_e (\Delta\rho)^2 [(1 - \phi) V_{\text{solid particle}} P(q)S(q) + \phi V_{\text{pore}} P(q)S(q)], \quad (\text{B.11})$$

where $V_{\text{solid particle}}$ is the total volume of the solid phase, and V_{pore} is the total pore volume. The term $\Delta\rho = \rho_{\text{pore}} - \rho_{\text{solid particle}}$ is the difference between the electron density of the pore and solid respectively. The pore phase, however, consists of vacuum and has an electron density of zero, $\rho_{\text{pore}} = 0$. This gives $(\Delta\rho)^2 = \rho_{\text{solid particle}}^2$.

The term $\rho_{\text{solid particle}}$ is by definition the electron density of the solid material. The solid material is carbon with a skeletal density, ρ_{skeleton} . The electron density for this material is given by

$$\rho_e = \frac{\text{no of electrons} \times \rho_{\text{skeleton}}}{m_{\text{carbon atom}}} \quad (\text{B.12})$$

Using Babinet's complementarity principle, a consequence of Fourier inversion (Section B.7.1), the pore is effectively assigned the electron density of the carbon and the carbon is effectively assigned the electron density of the vacuum phase. In sum, $\Delta\rho = \rho_{\text{pore}} \rightleftharpoons \rho_{\text{solid particle}} = \rho_e$.

Making these substitutions into Equation (B.11) and using the approximation that at large q values $S(q) \approx 1$, the final result is

$$\left(\frac{d\Sigma}{d\Omega}\right)_{\text{sample}} = \left(\frac{d\sigma}{d\Omega}\right)_e \underbrace{\left(\frac{\text{no. of electrons} \times \rho_{\text{skeleton}}}{m_{\text{carbon atom}}}\right)^2}_{\Delta\rho=\rho_e} \phi(1 - \phi)V_{\text{pore}}P(q). \quad (\text{B.13})$$

We are interested in the fluctuation of the difference in the average scattering length densities of the pore and solid. This is reflected by the term $(\Delta\rho)^2\phi(1 - \phi)$ in Equation (B.13).

B.7.1 Mathematical statement of Babinet's principle

For a system with a volume $V_{\text{sample}} = V_{\text{pore}} + V_{\text{solid}}$ and scattering length density

$$\rho(r) = \begin{cases} \rho_{\text{pore}} & \text{for } r \in V_{\text{pore}} \\ \rho_{\text{solid}} & \text{for } r \in V_{\text{solid}} \end{cases}$$

the Babinet principle of complementarity is stated as

$$\begin{aligned} \left(\frac{d\Sigma}{d\Omega} \right)_{\text{sample}} &= \frac{1}{V} \left| \int_{V_{\text{pore}}} \rho_{\text{pore}} e^{i\vec{q} \cdot \vec{r}} d\vec{r}_{\text{pore}} + \int_{V_{\text{solid}}} \rho_{\text{solid}} e^{i\vec{q} \cdot \vec{r}} d\vec{r}_{\text{solid}} \right|^2 \\ &= \frac{1}{V} \left| \int_{V_{\text{pore}}} \rho_{\text{pore}} e^{i\vec{q} \cdot \vec{r}} d\vec{r}_{\text{pore}} + \rho_{\text{solid}} \left(\int_{V_{\text{sample}}} e^{i\vec{q} \cdot \vec{r}} d\vec{r}_{\text{sample}} - \int_{V_{\text{pore}}} e^{i\vec{q} \cdot \vec{r}} d\vec{r}_{\text{pore}} \right) \right|^2 \\ &= \frac{1}{V} (\rho_{\text{pore}} - \rho_{\text{solid}})^2 \left| \int_{V_{\text{pore}}} e^{i\vec{q} \cdot \vec{r}} d\vec{r}_{\text{pore}} \right|^2 \end{aligned}$$

B.8 Correlation Function

The correlation function is not just defined geometrically (Section 3.6.2). It is equivalently defined as the normalized convolution square of the electron density fluctuations in the sample:

$$g(r) = \frac{\int_0^L \rho(\vec{x} + \vec{r}) \rho(\vec{x}) dx}{\int_0^L \rho^2(x) dx}, \quad (\text{B.14})$$

satisfying the conditions $g(0) = 1$ and $g(L_{\text{max}}) = 0$. This definition is more difficult to visualize and is less intuitive than the illustration given in Figure 3.4. Using Equation (B.14), the correlation function and intensity can be written as a pair of integral transforms:

$$g(r) = \frac{\int_0^\infty q^2 I(q) \frac{\sin(qr)}{qr} dq}{\int_0^\infty q^2 I(q) dq} \Leftrightarrow I(q) = \frac{\int_0^L 4\pi r^2 g(r) \frac{\sin(qr)}{qr} dr}{\int_0^L 4\pi r^2 g(r) dr} \quad (\text{B.15})$$

This relation is used to calculate the correlation function from the experimental data.

The correlation function can also be written as a series

$$g(r) = 1 + c_1 r + c_2 r^2 + c_3 r^3 + c_4 r^4 + \dots \quad (\text{B.16})$$

The first coefficient $c_1 = S/4V$ is the internal surface-to-volume ratio. A non-zero quadratic coefficient, c_2 , indicates the existence of edges and tips. The coefficient c_3 is determined by the curvature of the particle [75].

Dr. Peter Pfeifer has written an extensive general treatise on the correlation function for fractal, subfractal, and non-fractal scatterers that should be consulted for more detail [27].

B.9 Guinier approximation

The Guinier approximation is a model-independent analysis that is typically applied to the low angle part of the scattering curve, $qR_G \ll 1$, where R_G is the radius of gyration. The radius of gyration borrows directly from classical mechanics, "with the role of the mass played by electrons" [33]. It has the equivalent form as its dynamical counterpart $R_G^2 = (\int r^2 \rho(r) d^3r / \int \rho(r) d^3r)$.

B.9.1 Derivation

The derivation of R_G begins with the scattered intensity for a single sphere,

$$I(q) = V_{\text{sphere}}^2 \rho^2 \left(\frac{3(\sin qR - qR \cos qR)}{(qR)^3} \right)^2.$$

Using the series expansion

$$\frac{\sin(qR)}{qR} \approx 1 - \frac{q^2 R^2}{3!} + \frac{q^4 R^4}{5!} - \dots,$$

and

$$\cos(qR) \approx 1 - \frac{q^2 R^2}{2!} + \frac{q^4 R^4}{4!} - \dots$$

gives

$$I(q) \approx V_{\text{sphere}}^2 \rho^2 \left[1 - \frac{q^2 R^2}{10} \right]^2 \approx V_{\text{sphere}}^2 \rho^2 e^{-(q^2 R^2)/5}.$$

Using the classical relation $R_G = \sqrt{5/3}R$, and substituting it into Equation (B.17) gives an expression for the intensity in terms of the radius of gyration of a sphere

$$I(q) \approx V_{\text{sphere}}^2 \rho^2 e^{-(q^2 R_G^2)/3} \quad (\text{B.17})$$

The radius of gyration can be used for several different shapes and is not limited to the case of the sphere. The R_G and its associated parameters for some common shapes are listed in Table B.1.

Table B.1: R_G^2 for some common shapes and the relation to their parameters.

Shape	Parameters	R_G^2
Sphere	sphere radius, R	$3/5 R^2$
Elliptical cylinder	semi-axis a and b and height h	$\frac{a^2+b^2}{4} + \frac{h^2}{12}$
Rectangular box	side lengths a, b, c	$\frac{a^2+b^2+c^2}{12}$
Spherically hollow shell	inner radius R_1 and outer radius R_2	$\frac{3}{5} \frac{R_2^5 - R_1^5}{R_2^3 - R_1^3}$

Forward scattered intensity

In the case that the volume of the scatterer or its electron density is known to some degree of precision, the forward scattering intensity $I(0)$ can be calculated by evalu-

ating Equation (B.17) at $q=0$. This gives

$$I(0) \sim V_{\text{sphere}}^2 \rho^2. \quad (\text{B.18})$$

Because the the electron density is taken to be constant in the small-angle regime, $I_0 \propto V_{\text{sphere}}^2$ and therefore gives a rough indication of the particle size.

Experimentally the value of R_G is found by extrapolating the plateau of the SAS curve to $q = 0$, if it is sufficiently behaved. However, It is considered better practice to find the value of R_G by measuring the slope of a plot of $(d\Sigma/d\Omega)_{\text{sample}}$ vs. q^2 .

$$I(q) = I(0)e^{-(q^2 R_G^2)^2/3}. \quad (\text{B.19})$$

Appendix C

Experimental setup

C.1 Transmission electron microscope

Transmission electron micrographs were taken at the Electron Microscopy Core (EMC) at the University of Missouri using a JEOL 1400 transmission electron microscope operating at 120 keV. Samples were prepared for TEM by dispersing the carbon in methyl alcohol and depositing it on holey carbon films [76].

C.2 Hydrogen isotherms

Hydrogen isotherms were measured using a Hiden HTP1-V volumetric analyzer capable of performing measurements for pressures between 1-100 bar and temperatures between 77-775 K (Hiden Analytical, Warrington, UK). The instrument records the Gibbsian excess adsorption, most commonly measured by our group at temperatures of 80 K and 303 K and pressures between 50-100 bar.

Before measurements are made, the sample cell is outgassed at room temperature for 30 minutes and the mass is measured under vacuum. Then the sample cell with

sample is outgassed at 400°C for two hours and the mass is measured under vacuum. After the sample is loaded into the instrument, a leak test is performed at pressures ranging from 50 to 100 bar. The sample is then outgassed under ultra-high vacuum (10^{-8} mbar) at 200°C for three hours.

C.3 Nitrogen isotherms

Nitrogen adsorption isotherms for pressures 10^{-7} -1 bar at 77 K (sub-critical temperature and pressure) were measured using a Quantachrome Instruments Autosorb 1-C. The porosity, ϕ was measured as the ratio of cumulative pore volume to total sample volume measured from N₂ isotherms at $p/p_0 = 0.995$. Pore size distributions (PSD) were calculated using the slit pore, QSDFT equilibrium model kernel. Further details can be found in [16]. Calculations assume a skeletal density, $\rho_{\text{skeleton}} = 2.0\text{g/cm}^3$. The option of using a cylindrical equilibrium NLDFT kernel is available in the software and we note that its use would be consistent with our assertion of cylindrically shaped pores. However, there is no cylindrical QSDFT kernel available. The QSDFT model is described by the instrument manufacturer as the proper selection for “geometrically and chemically disordered micro-mesoporous carbons.” Previous ALL-CRAFT analyses have relied on the QSDFT routine, so its continued use also allows us to compare current and previous results.

C.4 X-ray scattering

C.4.1 Sample outgassing

Samples are placed in glass ampules and connected by a tube to a roughing vacuum pump with several glass fiber filters inserted to prevent vacuum and sample con-

tamination. After applying vacuum for ten minutes, the samples are then outgassed (still under vacuum) at either 400 °C for one hour, or 200°C for 4 hours. After the outgassing process, the glass ampules are sealed by torch. The vacuum is then disconnected. This procedure ensures that the samples are not exposed to moisture or ambient gases prior to measurement.

C.4.2 Ultra-small-angle x-ray scattering

Ultra Small Angle X-ray Scattering (USAXS) experiments were performed on beam-line 32-ID-B at the Advanced Photon Source (APS), Argonne National Laboratory (ANL), Chicago. The operational energy range of this instrument is 8 to 18 keV, with a dynamic intensity range of $10^8 - 10^9$ photons per unit solid angle per second (nine decades of intensity after desmearing), and q range of 10^{-4} to 10^{-1} \AA^{-1} [77].

A beam energy of 11.9 keV, (1.0149 \AA) is used. The carbon content of the glass ampule is dispersed between two pieces of blank scotch tape and positioned over holes in a pre-drilled aluminum paddle. The paddle is mounted onto a motorized stage whose translation allows sequential measurements of different samples.

Scotch tape has a high transparency and gives little diffuse background scattering. This tape is preferred to Kapton tape which has a diffraction peak located anywhere between the angles of $\theta=18$ and 6.5 degrees. A single side of scotch tape is 40-60 μm thick. The amount of sample dispersed between the two pieces of tape ranges from 60-270 μm . Thin sample sizes are used to reduce the possibility of multiple scattering. The thickness of the sample is measured using a digital micrometer, after the micrometer is zeroed to the thickness of the two tape. A blank sample, without carbon, is recorded approximately every ten scans for background subtraction purposes.

The one dimensional collimated USAXS setup is used, with a beam size of approximately $1 \times 2 \text{ mm}^2$, and sample to detector distance of 485 mm. Data acquisition

sition and reduction of the raw data is performed using the Igor Pro based *In-dra* and *Irena* data analysis suites developed by Jan Ilavsky and Pete Jemian [78] (<http://usaxs.xor.aps.anl.gov/staff/ilavsky/irena.html>). The Data reduction suite performs the calibration that scales relative units to units of absolute intensity units. The data reduction package also performs the necessary operation of desmearing the sample to data.

C.5 Small-angle x-ray scattering

Pinhole small-angle x-ray scattering experiments were performed on beamline 15-ID-B at the APS,ANL. This instrument has an x-ray energy range of 6-30 KeV and wavelength range of 0.4-2.0Å. A beam energy of 12.0 keV (1.033Å) was used. All efforts were made to match the energy of the SAXS beamline to the USAXS beamline so that the SAXS data collected could be compared with USAXS data, in the region where the two instruments overlap.

A BAS2500 imaging plate scanner (2000x2500 mm, 100 μ pixel size) was used with a sample to detector distance of 570 mm. Exposures of 10, 20, 40 and sometimes 60 seconds were taken for each sample. Dark frames were collected for exposures of 10, 20, 30, 40, 60, and 80 seconds. The optimal sample exposure time was 20 seconds. Data was imported and reduced in *Igor pro* using the *Nika* 2D to 1D SAS reduction macros written by Jan Ilavsky (<http://usaxs.xor.aps.anl.gov/staff/ilavsky/nika.html>).

Sample were outgassed using the same technique discussed in Appendix ???. Carbon powder was placed between two 25x25 mm glass cover slide slips with thicknesses between 170 and 250 μ m. One cover slip was attached to one side of an *Imaging Spacer* chamber with two-sided adhesive backing (purchased from Grace Bio-Labs). Sample chambers have a thickness of approximately 1 mm.

Carbon was placed inside the imaging spacer. The second cover slip was then

mounted to the second side of the imaging spacer, creating a water-tight sealed cell. Unlike the case of USAXS, multiple scattering and sample thicknesses are not major concerns for the pinhole SAXS setup due to the narrow beam size used.

C.5.1 Contrast matching

For each sample 10 μL of dibromomethane, CH_2Br_2 , (Sigma-Aldrich $\geq 99\%$) was micro-pipetted into a small slot cut into the top of the sample cells made for the dry sample SAXS measurements. The slots were v-shaped, allowing us to load DBM from the top, minimizing sample exposure to ambient conditions. DBM evaporated fairly quickly.

Ideally, the dry samples would be wetted first and then sealed, following the same procedure used for preparing the dry samples. However, the DBM attacked the adhesive backing of the imaging spacer chamber causing it to leak. This made it impossible to wet the sample before attaching the second glass cover slip.

Samples were measured in 20, 30, and 60 second exposures before and after wetting with (DBM).

C.6 Boron doping procedures

C.6.1 Method I,A

Ten mg of $\text{B}_{10}\text{H}_{14}$ and 1 gram of carbon were mixed in a glass reaction vessel. The reaction vessel is cooled down to -30°C and outgassed under vacuum for 1 hour. The reaction mixture was heated to 120°C for 1 hour and then cooled to ambient temperature under argon atmosphere. It was transferred to a sealed stainless steel tube under argon atmosphere in a glove box. Finally, it was annealed at 600°C , 800°C , or 1000°C .

C.7 Method II, A

Ten mg of $B_{10}H_{14}$ and 1 gram of carbon parent sample were mixed in a glass reaction vessel. The reaction vessel containing decaborane and carbon was cooled down to $-30^{\circ}C$ and put under vacuum for 1 hour. The reaction mixture was heated to $250^{\circ}C$ for 4 hours and then cooled to ambient temperature under argon atmosphere. It was transferred to a stainless steel tube under argon atmosphere in a glove box. Then it was then annealed at $600^{\circ}C$, $800^{\circ}C$, or $1000^{\circ}C$.

Appendix D

Mathematica and SAXS

Mathematica is known for its ability to perform symbolic computation. Its user interface in comparison to other data processing programs is less friendly. From the notebook front end all commands must be typed and there are no local scripting operations to help expedite the process. There is also no *bona fide* debugger. What Mathematica does have is the capacity for making customized user interfaces. The cost is cheap for a simple interface.

The form factors used throughout this study are highly oscillatory. Minimization of the chi-square error via non-linear least squares methods gives terrible results. Since the human eye is the most precise instrument for fitting SAXS curves, a goal was set to make a Mathematica interface for SAXS curve fitting that used technology to recapture the reliability of human judgement.

The primary aim was to make the data fitting process interactive. This was accomplished by leveraging three key mathematica commands: Manipulate, Dynamic, and DynamicModule. The entire code consists of nested structures of these commands.

The following are screen shots of the Mathematica program built for SAS fitting. The program has the capability to perform every task presented in this study: form factor fits, chi-square contour plots, correlation function analysis, etc.

D.1 Top panel

The top panel of the user interface includes a button that allows the user to browse and open any file on the computer and automatically import it (Figure D.1). The slider on the left hand side of the panel controls the selection of the region of the curve the user wants to fit. On the right hand side are several tabs. The three form factors are available for interactive fitting. These are the cylinder, rectangular box, and sphere. Clicking on the tab gives the user access to all of the fit parameters. In this particular case the experimental data is green, and the form factor fit is blue. Changing any of the form factor fit parameters will cause the graph to update.

Another view of the top panel shows that the appearance of the curves can be completely customized. All of the different choices are housed in drop down boxes that allow the user to choose the shape of the data marker, its color, etc (Figure D.2).

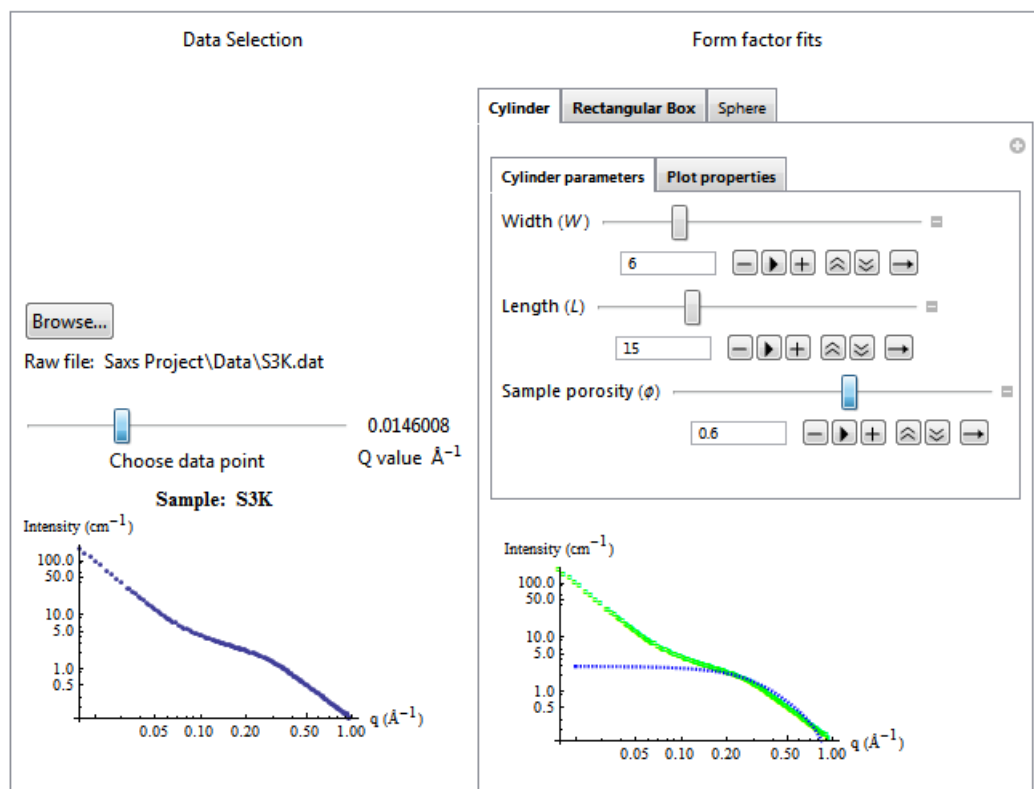


Figure D.1: This figure shows the top panel of the interface.

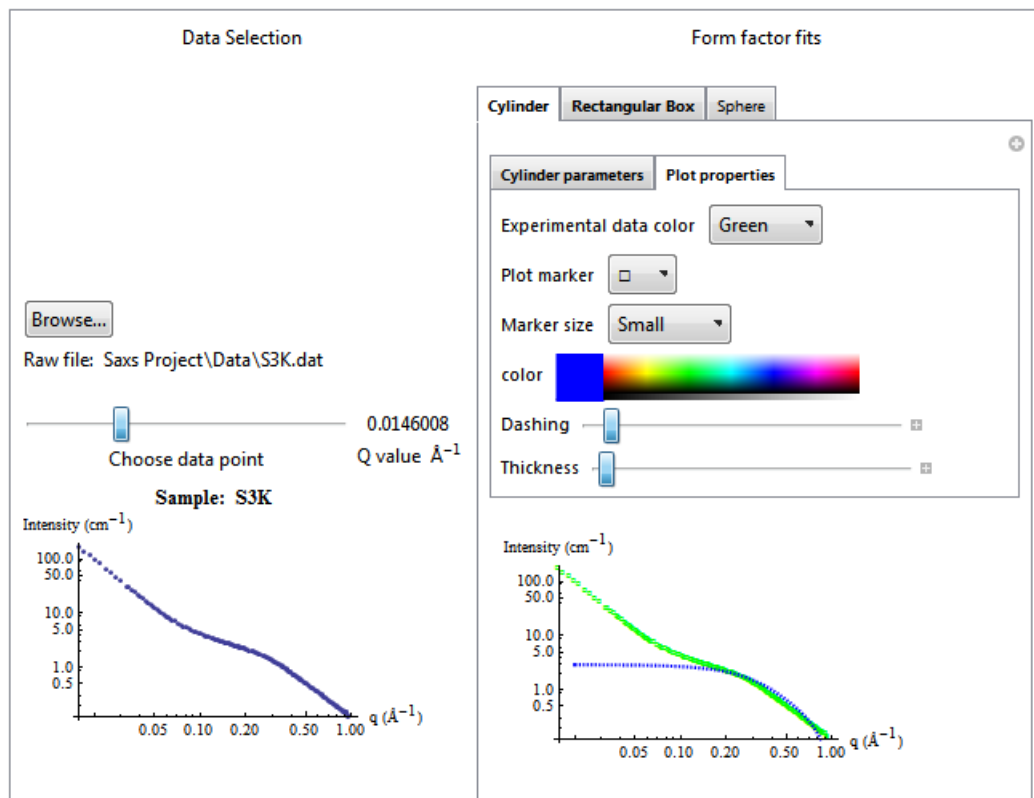


Figure D.2: This figure shows the ability of the user to customize the appearance of all plots.

D.2 Bottom panel

The bottom panel of the interface allows the user to automatically plot contour plots or to perform a correlation function analysis by clicking a checkbox (Figure D.3). The cylindrical or rectangular chi-square plot can be chosen by the user. Additionally there is the option to choose the intervals for all width, lengths, and side lengths that the program will tabulate. Even the step size can be chosen. There is also a popup-menu allowing a choice of different color selection schemes.

The right hand side of the bottom panel lets the user perform the correlation function analysis. There are two input boxes to type proposed values of W_1 and C_1 . This causes the plot to redraw all of the graphical intercepts and relabel all portions of the graph automatically. The porosity is calculated and printed in the blue box

marked SAXS porosity.

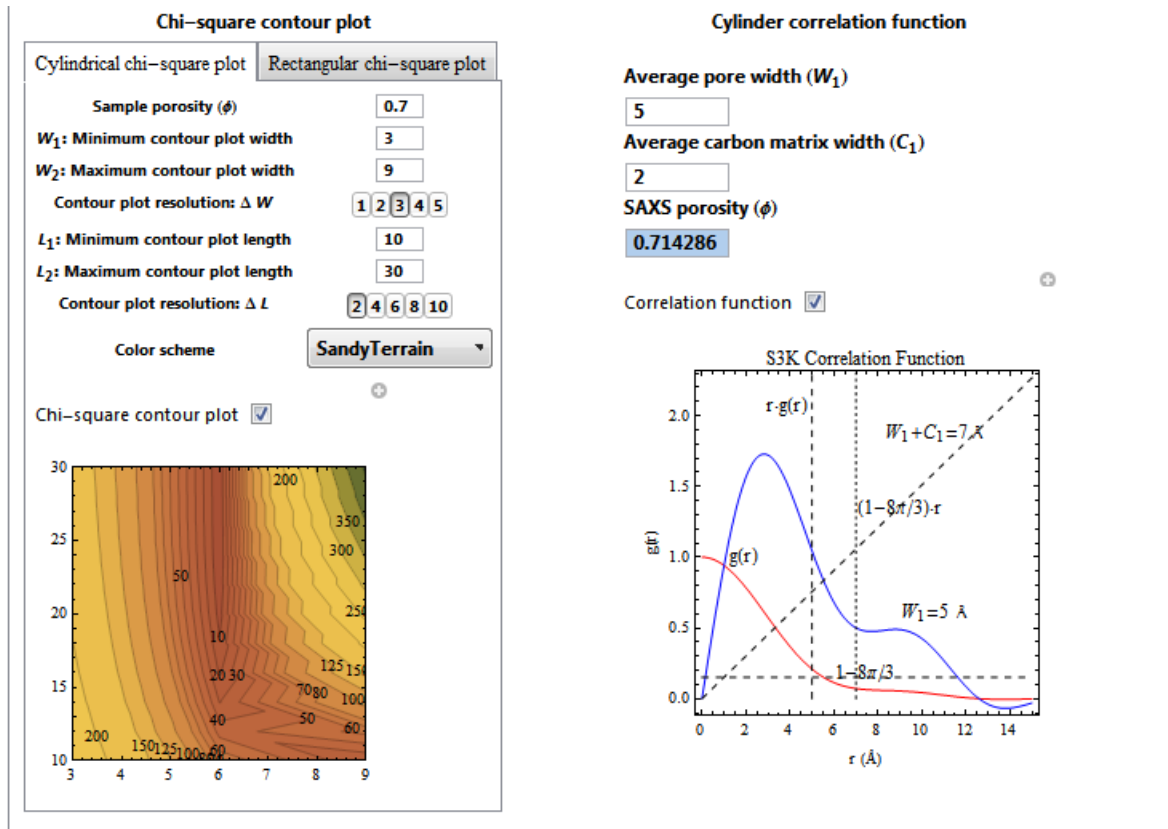


Figure D.3: This figure shows the bottom panel of the interface. This contains the portion of the interface that allows the user to make chi-square plots and perform a correlation function analysis.

Bibliography

- [1] P. Adler. *Porous media: geometry and transports*. Butterworth-Heinemann, New York, 1992.
- [2] Y Yortsos. Probing pore structures by sorption isotherms and mercury porosimetry. In Po zen Wong, editor, *Methods of the physics of porous media*, pages 69–117. Academic Press, 1999.
- [3] P. Pfeifer and A. Salli. The distribution of voids in fractal and other disordered structures. Unpublished manuscript.
- [4] Po-zen Wong, editor. *Methods in the physics of porous media*. Academic Press, 1999.
- [5] M Sahimi. *Flow and transport in porous media and fractured rock: from classical methods to modern approaches*. VCH Publishers, 1995.
- [6] M. Sahimi. Flow phenomena in rocks: from continuum models to fractals, percolation, cellular automata, and simulated annealing. *Reviews of Modern Physics*, 4:1394–1534, 1993.
- [7] R.L. Kleinberg. Nuclear magnetic resonance. In Po zen Wong, editor, *Methods in the physics of porous media*, pages 337–385. Academic Press, 1999.
- [8] A.A. Garca Blanco, J.C. Alexandre de Oliveira, R. Lpez, J.C. Moreno-Piraj, L. Giraldo, G. Zgrablich, and K. Sapag. A study of the pore size distribution for

- activated carbon monoliths and their relationship with the storage of methane and hydrogen. *Colloids and Surfaces A: Physicochemical and Engineering Aspects*, 357:74 – 83, 2010.
- [9] P. Pfeifer. Small-angle scattering laws for intermediates between surface, mass, and pore fractals. In V.K. Varadan and V.V. Varadan, editors, *Multiple Scattering of Waves in Random Media and Random Rough Surfaces*, pages 45–49, Pennsylvania State University, 1987. The Pennsylvania State University.
- [10] P. Pfeifer, F. Ehrburger-Dolle, T. P. Rieker, M. T. Gonzalez, W. P. Hoffman, M. Molina-Sabio, F. Rodriguez-Reinoso, P. W. Schmidt, and D. J. Voss. Nearly space-filling fractal networks of carbon nanopores. *Physical Review Letters*, 88(11):1155021–1155024, 2002.
- [11] P. Pfeifer and D. Avnir. Chemistry in noninteger dimensions between two and three. i. fractal theory of heterogeneous surfaces. *The Journal of Chemical Physics*, 79(7):3558–3565, 1983.
- [12] G. M. Davies and N. A. Seaton. The effect of the choice of pore model on the characterization of the internal structure of microporous carbons using pore size distributions. *Carbon*, 36(10):1473–1490, 1998.
- [13] P. Mittelbach and G. Porod. Zur rontgenkleinwinkelstreuung verdünnter kolloider systeme. die berechnung der strukturen von parallelepipedern. *Acta Physica Austriaca*, 14:185–211, 1961.
- [14] H. Marsh and F. Rodriguez-Reinoso. *Activated Carbon*. Elsevier, New York : Elsevier, 2006.
- [15] R.C. Bansal and M. Goyal. *Activated Carbon Adsorption*. CRC Press, 2005.

- [16] J. Burress, M. Kraus, M. Beckner, R. Cepel, G. Suppes, C. Wexler, and P. Pfeifer. Hydrogen storage in engineered carbon nanospaces. *Nanotechnology*, 20(20):33333, 2009.
- [17] J. Burress. *Gas adsorption in engineered carbon nanospaces*. PhD thesis, University of Missouri, 2009.
- [18] M.M. Dubinin and H.F. Stoeckli. Homogeneous and heterogeneous micropore structures in carbonaceous adsorbents. *Journal of Colloid And Interface Science*, 75(1):34–42, 1980.
- [19] C. Lastoskie, K.E. Gubbins, and N. Quirke. Pore size distribution analysis of microporous carbons: A density functional theory approach. *Journal of Physical Chemistry*, 97(18):4786–4796, 1993.
- [20] R. J. Dombrowski, D.R. Hyduke, and C. M. Lastoskie. Pore size analysis of activated carbons from argon and nitrogen porosimetry using density functional theory. *Langmuir*, 16(11):5041–5050, 2000.
- [21] B. Kuchta, L. Firlej, P. Pfeifer, and C. Wexler. Numerical estimation of hydrogen storage limits in carbon-based nanospaces. *Carbon*, 48:223–331, 2010.
- [22] A. Braun, M. Bartsch, B. Schnyder, R. Katz, O. Haas, H. G. Haubold, and G. Goerigk. X-ray scattering and adsorption studies of thermally oxidized glassy carbon. *Journal of Non-Crystalline Solids*, 260(1-2):1–14, 1999.
- [23] W. S. Rothwell. Small-angle x-ray scattering from glassy carbon. *Journal of Applied Physics*, 39(3):1840–1845, 1968.
- [24] E. Hoinkis. Small-angle scattering studies of adsorption and of capillary condensation in porous solids. *Particle and Particle Systems Characterization*, 21(2):80–100, 2004.

- [25] A. Guinier and G. Fournet. *Small-angle scattering of X-rays*. Structure of matter series. Wiley, New York,, 1955.
- [26] W. Gille. The small-angle scattering correlation function of the cuboid. *Journal of Applied Crystallography*, 32(6):1100–1104, 1999.
- [27] P. Pfeifer. Exact results for the small angle scattering correlation function for fractal, subfractal, and non-fractal scatterers. Unpublished manuscript.
- [28] H. S. Sukiasian and Wilfried Gille. Relation between the chord length distribution of an infinitely long cylinder and that of its base. *Journal of Mathematical Physics*, 48(5):053305, 2007.
- [29] W. Gille. Characteristics of the sas correlation function of long cylinders with oval cross-section. *Journal of Applied Crystallography*, 43:222, 2010.
- [30] A. Mazzolo, B. Roesslinger, and W. Gille. Properties of chord length distributions of nonconvex bodies. *Journal of Mathematical Physics*, 44(12):6195–6208, 2003.
- [31] W. Gille, D. Enke, and F. Janowski. Order distance estimation in porous glasses via transformed correlation function of small-angle scattering. *Journal of Porous Materials*, 8(2):111–117, 2001.
- [32] W. Gille, D. Enke, and F. Janowski. Stereological macropore analysis of a controlled pore glass by use of small-angle scattering. *Journal of Porous Materials*, 8(3):179–191, 2001.
- [33] O. Glatter and O. Kratky. *Small angle x-ray scattering*. Academic Press, London ; New York, 1982.
- [34] P. Pfeifer, G.J. Suppes, P.S. Shah, and J.W. Burres. US Patent application, 2007. 11/937,150.

- [35] M.A. Lillo-Rdenas, D. Cazorla-Amors, and A. Linares-Solano. Understanding chemical reactions between carbons and naoh and koh: An insight into the chemical activation mechanism. *Carbon*, 41(2):267 – 275, 2003.
- [36] J.A. Macia-Agullo, B.C. Moore, D. Cazorla-Amoros, and A. Linares-Solano. Influence of carbon fibres crystallinities on their chemical activation by koh and naoh. *Microporous and Mesoporous Materials*, 101:397–405, 2007.
- [37] M.Z. Figueroa-Torres, A. Robau-Snchez, L. Torre-Senz, and A. Aguilar-Elguzabal. Hydrogen adsorption by nanostructured carbons synthesized by chemical activation. *Microporous and Mesoporous Materials*, 98(1-3):89 – 93, 2007.
- [38] R. Ubago-Prez, F. Carrasco-Marn, D. Fairn-Jimnez, and C. Moreno-Castilla. Granular and monolithic activated carbons from koh-activation of olive stones. *Microporous and Mesoporous Materials*, 92(1-3):64 – 70, 2006.
- [39] T. Tomokazu, T. Ikumi, O. Hiroki, O. Shigeo, H. Hiroki, A. and Syuji, K. Toshinori, and S. Hidetoshi. Detailed structural analyses of koh activated carbon from waste coffee beans. *Japanese Journal of Applied Physics*, 48(11):117001, 2009.
- [40] M. Kalliat, C. Kwak, and P. Schmidt. Small angle x-ray investigation of the porosity in coals. In *New Approaches in Coal Chemistry*. American Chemical Society, 1981.
- [41] S. Yeon, S. Osswald, Y. Gogotsi, J.P. Singer, J.M. Simmons, J.E. Fischer, M.A. Lillo-Rdenas, and A. Linares-Solano. Enhanced methane storage of chemically and physically activated carbide-derived carbon. *Journal of Power Sources*, 191:560 – 567, 2009.

- [42] K. Laszlo, O. Czakkel, K. Josepovits, C. Rochas, and E. Geissler. Influence of surface chemistry on the saxs response of polymer-based activated carbons. *Langmuir*, 21(18):8443–8451, 2005.
- [43] O. Toshiro, T. Ritsuo, and I. Masao. Production and adsorption characteristics of maxsorb: High-surface-area active carbon. *Gas Separation and Purification*, 7(4):241–245, 1993.
- [44] W. Gille, D. Enke, F. Janowski, and T. Hahn. About the realistic porosity of porous glasses. *Journal of Porous Materials*, 10(3):179–187, 2003.
- [45] R. Franklin. The structure of graphitic carbons. *Acta Crystallographica*, 4(3):253–261, 1951.
- [46] E. Hoinkis. Small-angle scattering of neutrons and x-rays from carbons and graphites. In P.A. Thrower, editor, *Chemistry and physics of carbon*, volume 25. M. Dekker etc., 1997.
- [47] D. F. Quinn. Supercritical adsorption of permanent gases under corresponding states on various carbons. *Carbon*, 40(15):2767 – 2773, 2002.
- [48] P. Pfeifer, C. Wexler, and F. Hawthorne. Networks of boron-doped carbon nanopores for low-pressure reversible hydrogen storage. Technical report, University of Missouri, 2006.
- [49] B. Kuchta, L. Firlej, R. Cepel, P. Pfeifer, and C. Wexler. Structural and energetic factors in designing a nanoporous sorbent for hydrogen storage. *Colloids and Surfaces A: Physicochemical and Engineering Aspects*, 357:61–66, 2010.
- [50] R. Franklin. The interpretation of diffuse x-ray diagrams of carbon. *Acta Crystallographica*, 3(2):107–121, 1950.

- [51] R.E. Franklin. Crystallite growth in graphitizing and non-graphitizing carbons. *Proceedings of the Royal Society of London. Series A, Mathematical and Physical Sciences*, 209(1097):196–218, 1951.
- [52] E. Fitzer, W. Schaefer, and S. Yamada. The formation of glasslike carbon by pyrolysis of polyfuryl alcohol and phenolic resin. *Carbon*, 7:643–646, 1969.
- [53] R. Perret and W. Ruland. X-ray small-angle scattering of glassy carbon. *Journal of Applied Crystallography*, 5:183–187, 1972.
- [54] K.A. Sosin, D. F. Quinn, and J.F. MacDonald. Changes in PSD of progressively activated carbons obtained from their supercritical methane isotherms. *Carbon*, 34:1335–1341, 1996.
- [55] D. Fairn-Jimnez, F. Carrasco-Marin, D. Djurado, F. Bley, F. Ehrburger-Dolle, and C. Moreno-Castilla. Surface area and microporosity of carbon aerogels from gas adsorption and small- and wide-angle x-ray scattering measurements. *The Journal of Physical Chemistry B*, 110:8681–8688, 2006.
- [56] L. Firlej, S. Roszak, B. Kuchta, P. Pfeifer, and C. Wexler. Enhanced hydrogen adsorption in boron substituted carbon nanopores. *Journal of Chemical Physics*, 131:164702, 2009.
- [57] P. Pfeifer, C. Wexler, G. Suppes, F. Hawthorne, S. Jalisatgi, M. Lee, and D. Robertson. Multiply surface-functionalized nanoporous carbon for vehicular hydrogen storage. In *2010 DOE Hydrogen Program Annual Merit Review*, Washington, D.C., June 2010. 2010 DOE Hydrogen Program Annual Merit Review. Presentation.
- [58] Meakin. *Fractals, scaling and growth far from equilibrium*. Number 5 in Cambridge nonlinear science series. Cambridge University Press, New York, 1998.

- [59] J.F. Gouyet. *Physics and fractal structures*. Springer, New York, 1996.
- [60] S.K. Bhatia and A.L. Myers. Optimum conditions for adsorptive storage. *Langmuir*, 22:1688–1700, 2006.
- [61] M. Rzepka, P. Lamp, and M.A. de la Casa-Lillo. Physisorption of hydrogen on microporous carbon and carbon nanotubes. *Journal of Physical Chemistry B*, 102:10894–10898, 1998.
- [62] K. Laszlo and E. Geissler. Surface chemistry and contrast-modified saxs in polymer-based activated carbons. *Carbon*, 44:2437–2444, 2006.
- [63] S. Jahnert, D. Muter, J. Prass, G.A. Zickler, O. Paris, and G.H. Findenegg. Pore structure and fluid sorption in ordered mesoporous silica. i. experimental study by in situ small-angle x-ray scattering. *Journal of Physical Chemistry C*, 113(34):15201–15210, 2009.
- [64] D. Muter, S. Jahnert, J.W.C. Dunlop, G.H. Findenegg, and O. Paris. Pore structure and fluid sorption in ordered mesoporous silica. ii. modeling. *Journal of Physical Chemistry C*, 113(34):15211–15217, 2009.
- [65] D.M Smith, W. Earl, and D.W. Hua. Advanced nmr-based techniques for pore structure analysis of coal. Final Project Report, March 1995. DOE/PC/91296-15.
- [66] The Alliance for Collaborative Research in Alternative Fuel Technology website. <http://all-craft.missouri.edu/>.
- [67] P. Pfeifer, C. Wexler, G. Suppes, F. Hawthorne, S. Jalisatgi, M. Lee, and D. Robertson. Multiply surface-functionalized nanoporous carbon for vehicular hydrogen storage. DOE EERE annual progress report, University of Missouri, 2009.

- [68] P. Pfeifer, F. Hawthorne, and C. Wexler. Networks of boron-doped carbon nanopores for low-pressure reversible hydrogen storage. In *2009 DOE Annual merit review*, Arlington, VA, May 2009. 2009 DOE Annual merit review. Presentation.
- [69] P. Pfeifer. Fractals in surface science: Scattering and thermodynamics of adsorbed films. In R. Editor Vanselow and Russel F. Editor Howe, editors, *Chemistry and Physics of Solid Surfaces VII*. Springer, New York, 1988.
- [70] E. Kaler. Small-angle scattering from colloidal dispersions. *Journal of Applied Crystallography*, 21(6):729–736, 1988.
- [71] T. Davis. *Statistical Mechanics of Phases, Interfaces, and Thin Films*. VCH Publishers, 1996.
- [72] J. S. Pedersen. Analysis of small-angle scattering data from colloids and polymer solutions: Modeling and least-squares fitting. *Advances in Colloid and Interface Science*, 70(1-3):171–210, 1997.
- [73] S. Hansen. Simultaneous estimation of the form factor and structure factor for globular particles in small-angle scattering. *Journal of Applied Crystallography*, 41:436–445, 2008.
- [74] J. Kohlbrecher and I. Bressler. Sasfit.
- [75] W. Gille, A. Mazzolo, and B. Roesslinger. Analysis of the initial slope of the small-angle scattering correlation function of a particle. *Particle & Particle Systems Characterization*, 22(4):254–260, 2005.
- [76] J. Romanos. Methane storage in monolithic and powdered activated carbons. March quarterly report.

- [77] J. Ilavsky, P. R. Jemian, A. J. Allen, F. Zhang, L. E. Levine, and G. G. Long. Ultra-small-angle x-ray scattering at the advanced photon source. *Journal of Applied Crystallography*, 42(3):469–479, 2009.
- [78] J. Ilavsky and P. R. Jemian. Irena: Tool suite for modeling and analysis of small-angle scattering. *Journal of Applied Crystallography*, 42(2):347–353, 2009.

VITA

Michael Kraus was born on April 11, 1978 in Phoenix, Arizona. He holds two bachelors degrees. He graduated *Summa Cum Laude* from Washington University in St. Louis with a bachelors degree in anthropology in 2001. He then attended the University of Missouri, St. Louis, where he earned a bachelors degree in physics with *Latin honors* in 2005.

From October 2005 through December 2006 he worked at MEMC Electronic Materials before attending the University of Missouri. He received his Ph.D. in physics from the University of Missouri in 2010 working under the advisement of Dr. Peter Pfeifer.